A STUDY OF THE CHEMICAL INTERACTIONS AT THE INTERFACE BETWEEN POLYMERIC POWDER/FIBRE AND WHITE CEMENT

by

Jennifer Lynn MacDonald

Submitted in partial fulfillment of the requirements
for the degree of Doctor of Philosophy

at

Dalhousie University
Halifax, Nova Scotia
October 2010

DALHOUSIE UNIVERSITY

DEPARTMENT OF CHEMISTRY

The undersigned hereby certify that they have read and recommend to the Faculty of Graduate Studies for acceptance a thesis entitled "A STUDY OF THE CHEMICAL INTERACTIONS AT THE INTERFACE BETWEEN POLYMERIC POWDER/FIBRE AND WHITE CEMENT" by Jennifer Lynn MacDonald in partial fulfillment of the requirements for the degree of Doctor of Philosophy.

Dated: October 14, 2010

External Examiner: _____

Research Supervisor: _____

Examining Committee: _____

_____

Departmental Representative: _____

DALHOUSIE UNIVERSITY

Date: October 14, 2010

AUTHOR: Jennifer Lynn MacDonald

TITLE: A STUDY OF THE CHEMICAL INTERACTIONS AT THE INTERFACE BETWEEN POLYMERIC POWDER/FIBRE AND WHITE CEMENT

DEPARTMENT OR SCHOOL: Department of Chemistry

DEGREE: PhD CONVOCATION: May YEAR: 2011

To my family

Table of Contents

List of Tables **ix**

List of Figures **x**

Abstract **xvi**

List of Abbreviations and Symbols Used **xvii**

Acknowledgements **xx**

Chapter 1. Introduction **1**

1.1 Preamble 1

1.2 Introduction 2

1.3 Cement Production 5

1.4 Cement Hydration 6

1.5 Concrete 10

1.5.1 Water to Cement Ratio 11

1.6 Reinforced Concrete 13

1.6.1 Why Does Concrete Need Reinforcement? 13

1.6.2 Steel Reinforcement 14

1.6.2.1 Bentur's Model of the Steel Fibre Concrete Interface 16

1.6.3 Synthetic Fibre Reinforcement 17

1.6.3.1 Review of Polymeric Fibres Used as Concrete Reinforcement 20

Chapter 2. Experimental Methods **25**

2.1 Nuclear Magnetic Resonance Spectroscopy 25

2.1.1 Single Pulse Excitation and Cross-Polarization NMR 27

2.1.2 Choice of Cement for NMR Study 29
2.1.3 NMR Active Nuclei in Cement 30
2.2 Infrared Spectroscopy 32
2.3 Ultraviolet-Visible Spectroscopy 33
2.4 Scanning Electron Microscopy/Energy Dispersive Spectroscopy . . . 33
2.4.1 Studying the Fibre/White Cement Interfacial Transition Zone via SEM/EDS 36
Chapter 3. Poly(ethylene-vinyl acetate) (EVA) Powder/White Cement NMR Study 40
3.1 Background 40
3.1.1 Sample Preparation 43
3.1.2 Experimental 44
3.2 Results and Discussion 45
3.2.1 NMR Studies 46
3.2.1.1 SPE ^{13}C NMR 47
3.2.1.2 ^{13}C CP/MAS NMR 49
3.2.1.3 SPE ^{43}Ca NMR 50
3.2.1.4 ^{29}Si SPE and CP/MAS NMR 53
3.2.2 Reaction Kinetics of EVA Hydrolysis in Cement 56
3.3 Conclusion 61
Chapter 4. Poly(ether imide)/White Cement NMR Study 62
4.1 Background 62
4.2 Sample Preparation 64
4.3 Experimental 64
4.4 Results and Discussion 65

4.5 Summary 72

Chapter 5. Poly(vinylidene fluoride)/White Cement Study 74

5.1 Background 74

5.2 Sample Preparation 76

5.3 Experimental 77

5.3.1 NMR Spectroscopy 77

5.3.2 Infrared Spectroscopy 78

5.3.3 Bromination Qualitative Test for the Presence of Alkene . . 78

5.3.4 Ultraviolet-Visible Spectroscopy 78

5.4 Results and Discussion 79

5.4.1 Dehydrofluorination of PVDF Mechanistic Pathways 79

5.4.2 SPE ^{13}C and ^{19}F NMR Spectroscopy 81

5.4.3 Infrared Spectroscopy 84

5.4.4 Bromination of Dehydrofluorinated PVDF 86

5.4.5 Ultraviolet-Visible Spectroscopy 87

5.5 Summary 90

Chapter 6. Short and Long Range Studies of the Polymeric Material/White Cement Interfacial Transition Zone 92

6.1 Background 92

6.2 Sample Preparation 96

6.2.1 Nuclear Magnetic Resonance Samples 96

6.2.2 SEM/EDS Samples 97

6.3 Experimental 99

6.3.1 NMR Spectroscopy 99

6.3.2 SEM/EDS 100

6.4 Results and Discussion 100

6.4.1 Interfacial Interactions Between Fluoropolymeric Powder and White Cement at Short Range 100

6.4.2 The Interfacial Transition Zone Surrounding Steel and Polymeric Fibres and White Cement at Long Range 107

6.4.2.1 Elemental Mapping 107

6.4.2.2 Point Analysis 112

6.4.2.3 Image Analysis 114

6.5 Summary 126

Chapter 7. Conclusion **128**

7.1 General Conclusions 128

7.2 Recommendations and Future Directions 130

References **133**

Appendix A. Fibre/White Cement Electron Images **142**

List of Tables

Table 1.1 Cement chemistry abbreviations 1

Table 1.2 Physical properties of fibres used for concrete reinforcement applications 22

Table 2.1 Comparison of calcium, silicon, aluminum, and iron oxides in regular and white cement 30

Table 2.2 Comparison of ^{1}H, ^{13}C, ^{19}F, ^{27}Al, ^{29}Si, and ^{43}Ca nuclear properties 32

Table 4.1 ^{13}C Spectral predictions for PEI and hydrolyzed PEI 68

Table 5.1 Vibrational assignment of PVDF powder 85

Table 6.1 SPE ^{13}C NMR chemical shifts for Nafion 104

Table 6.2 Cement hydration products 114

Table 6.3 t-test comparisons between PEI, PVA, Nylon, and PVDF SEM/EDS image analysis data 123

List of Figures

Figure 1.1 Representation of C_3S hydration in cement: pre-induction, induction, acceleration, and deceleration 8

Figure 1.2 Chemical structure of tobermorite 9

Figure 1.3 Chemical structure of jennite 10

Figure 1.4 Effect of water to cement ratio on hardened cement paste . . . 13

Figure 1.5 Effect of water to cement ratio on cement strength 14

Figure 1.6 Effect of steel reinforcement in concrete in areas experiencing tensile stress 16

Figure 1.7 Bentur's model of the steel fibre/concrete interface 17

Figure 1.8 Tensile stress-strain curve for fibre reinforced concrete 19

Figure 1.9 Toughness *vs.* interfacial bond strength in fibre reinforced concrete 21

Figure 2.1 Cross-polarization schematic diagram 28

Figure 2.2 Hartmann-Hahn matching and magnetization transfer in a cross-polarization NMR experiment 29

Figure 2.3 Schematic diagram of the electron column in a scanning electron microscope 35

Figure 2.4 SEM/EDS comparison of the steel fibre/white cement interface in an electron image and a Fe elemental map 36

Figure 2.5 Effect of accelerating voltage and average atomic number on the interaction volume in SEM/EDS experiment 38

Figure 2.6 Effect of spot size on interaction volume and resolution 38

Figure 3.1 Proposed mechanism and overall reaction for saponification of EVA in white cement during hydration 46

Figure 3.2 SPE ^{13}C NMR spectrum of EVA 48

Figure 3.3 SPE ^{13}C NMR spectra of EVA/white cement at various stages of hydration 48

Figure 3.4 SPE ^{13}C NMR spectra of hydrated white cement and EVA/white cement at 56 days hydration 49

Figure 3.5 ^{13}C CP/MAS NMR spectra of EVA/white cement at various hydration times 50

Figure 3.6 SPE ^{43}Ca NMR spectra of white cement, EVA/white cement, EVA/white cement 51

Figure 3.7 ^{29}Si SPE NMR spectrum of EVA/white cement after 1 week of hydration with D_2O 54

Figure 3.8 Q^n silicon centres for n=0, 1, 2, 3 55

Figure 3.9 ^{29}Si CP/MAS NMR spectra, at various contact times, of EVA/white cement after 1 week of hydration with D_2O 55

Figure 3.10 ^{29}Si CP/MAS NMR spectra of a white cement control and EVA/white cement after 1 week of hydration with D_2O 56

Figure 3.11 Potential hydrogen bonding between hydrolyzed EVA and CSH 57

Figure 3.12 Consumption of vinyl acetate and formation of $Ca(CH_3COO)_2$ over time 58

Figure 3.13 Pseudo-second order kinetics plot of EVA hydrolysis 58

Figure 3.14 Chemical reaction equation for vinyl acetate hydrolysis . . . 60

Figure 4.1 Poly(ether imide) chemical structure 62

Figure 4.2 PEI hydrolysis in NaOH as proposed by Jang *et al.* 66

Figure 4.3 PEI hydrolysis in NaOH as proposed by Kim *et al.* 67

Figure 4.4 PEI and hydrolyzed PEI segments 67

Figure 4.5 Predicted ^{13}C NMR stick spectra of PEI and hydrolyzed PEI products between 170-120 ppm 69

Figure 4.6 ^{13}C CP/MAS NMR spectra of PEI, hydrolyzed PEI, PEI/white cement (7 day hydration), and PEI/white cement (28 day hydration) 69

Figure 4.7 ^{13}C CP/MAS NMR PEI difference spectra 70

Figure 4.8 SPE ^{13}C NMR spectra of PEI, hydrolyzed PEI, PEI/white cement (7 day hydration), and PEI/white cement (28 day hydration) 72

Figure 4.9 SPE ^{13}C NMR PEI difference spectra 72

Figure 5.1 Chemical structure of poly(vinylidene fluoride) 74

Figure 5.2 Chemical structure of β-PVDF 75

Figure 5.3 Potential hydrogen bonding between β-PVDF and hydroxide in cementitious matrices 75

Figure 5.4 Bimolecular elimination (E2) mechanism 79

Figure 5.5 Nucleophilic substitution (S_N2) mechanism 80

Figure 5.6 Elimination by conjugate base (E1cB) mechanism 80

Figure 5.7 PVDF (brown particulate at the bottom of vial) and unreacted PVDF (white powder on the surface of NaOH solution) 81

Figure 5.8 PVDF backbone defects 82

Figure 5.9 SPE ^{13}C NMR spectra of difference spectrum (PVDF/white cement subtract PVDF), PVDF, and PVDF/white cement 83

Figure 5.10 SPE ^{19}F NMR spectra of difference spectrum (PVDF/white cement subtract PVDF), PVDF, and PVDF/white cement 83

Figure 5.11 IR spectra of dehydrofluorinated PVDF/Nujol, PVDF/Nujol, and Nujol from 4000-600 cm^{-1} 84

Figure 5.12 IR spectra of dehydrofluorinated PVDF/Nujol, PVDF/Nujol and Nujol from 1700-600 cm^{-1} 85

Figure 5.13 Schematic chemical equation for the bromination addition reaction to an alkene 86

Figure 5.14 Qualitative test for bromination of dehydrofluorinated PVDF 87

Figure 5.15 UV-Vis average spectra of PVDF and dehydrofluorinated PVDF 88

Figure 5.16 Effect of conjugation on energy band gap 89

Figure 5.17 UV-Vis average spectra of white cement and PVDF/white cement 90

Figure 6.1 Chemical structure of PFA and Teflon 94

Figure 6.2 Chemical structure of polymeric fibres 96

Figure 6.3 Epoxy impregnation apparatus 98

Figure 6.4 SEM/EDS fibre/white cement sample preparation 98

Figure 6.5 SPE ^{27}Al NMR spectra of white cement control, Teflon/white cement, and PFA/white cement 101

Figure 6.6 SPE ^{19}F NMR spectra of Teflon and Teflon/white cement . . 102

Figure 6.7 SPE ^{19}F NMR spectra of white cement control, PFA, and PFA/white cement 102

Figure 6.8 ^{13}C CP/MAS NMR spectra of white cement control and PFA/white cement 105

Figure 6.9 Chemical structure of Nafion 106

Figure 6.10 SPE ^{43}Ca NMR spectra of white cement control, Teflon/white cement, and PFA/white cement 106

Figure 6.11 SEM/EDS overlaid elemental maps of the steel/white cement interface 108

Figure 6.12 SEM/EDS overlaid elemental maps of the HDPE/PP/white cement interface 109

Figure 6.13 SEM/EDS overlaid elemental maps of the PVA/white cement interface 109

Figure 6.14 SEM/EDS overlaid elemental maps of the Nylon 6.6/white cement interface 110

Figure 6.15 SEM/EDS overlaid elemental maps of the PVDF/white cement interface 110

Figure 6.16 SEM/EDS overlaid elemental maps of the PEI/white cement interface 111

Figure 6.17 Example of a point map grid for elemental analysis of the interfacial transition zone in a steel fibre/white cement composite 113

Figure 6.18 Ca/Si ratio *vs.* distance from the fibre edge (each wedge number indicates a micron sized wedge) based upon point analysis data . . 114

Figure 6.19 Example of a fibre mask created and used for image analysis of SEM/EDS elemental maps 115

Figure 6.20 SEM/EDS elemental maps of the steel fibre/white cement interface 116

Figure 6.21 SEM/EDS elemental maps of the HDPE/PP fibre/white cement interface 117

Figure 6.22 SEM/EDS elemental maps of the PVA fibre/white cement interface 118

Figure 6.23 SEM/EDS elemental maps of the Nylon 6.6 fibre/white cement interface 119

Figure 6.24 SEM/EDS elemental maps of the PVDF fibre/white cement interface 120

Figure 6.25 SEM/EDS elemental maps of the PEI fibre/white cement interface 121

Figure 6.26 Example of micron sized slices used for SEM/EDS image analysis 122

Figure 6.27 Ca/Si ratio *vs.* distance from the fibre edge based upon image analysis results 122

Figure 6.28 Potential bonding between PVA and cementitious matrices 125

Figure A.1 Secondary electron image of the steel fibre/white cement interfacial transition zone 142

Figure A.2 Secondary electron image of the HDPE/PP fibre/white cement interfacial transition zone 143

Figure A.3 Secondary electron image of the PVA fibre/white cement interfacial transition zone 143

Figure A.4 Secondary electron image of the PVDF fibre/white cement interfacial transition zone 144

Figure A.5 Secondary electron image of the PEI fibre/white cement interfacial transition zone 144

Figure A.6 Secondary electron image of the Nylon 6.6 fibre/white cement interfacial transition zone 145

Abstract

Concrete, due to its low cost, durability and fire resistance, is one of the world's most widely used construction materials. Concrete is typically reinforced with steel bars and welded wire mesh. Since the cost of steel is increasing and steel corrosion is a significant contributor to structural failure, it is advantageous to find an alternative replacement reinforcement material which can not only replace the steel, but also resist corrosion.

Over the past few decades, polymeric fibres have been used as concrete reinforcement. The chemical bond between the polymeric fibre and the cementitious matrix is an important factor in the fibre's performance as a concrete reinforcement. Despite the great importance of the chemical bonding at the polymeric fibre/concrete interface, the chemical bonding at the interface is not well understood.

To investigate the chemical interactions between polymeric materials and concrete, model systems of polymeric powder/white cement and polymeric fibre/white cement were chosen, where white cement was chosen for its suitability for nuclear magnetic resonance (NMR) experiments. The chemical interactions between poly(ethylene-vinyl acetate) (EVA), poly(ether imide) (PEI), and poly(vinylidene fluoride) (PVDF) polymeric powders were studied via ^{13}C NMR spectroscopy. It was found that EVA admixture undergoes hydrolysis in a cementitious matrix and follows a pseudo-second order kinetics model up to 32 days of cement hydration. PEI was also found to undergo hydrolysis at the imide functional group in a cementitious matrix. PVDF powder undergoes dehydrofluorination in the cementitious environment, producing a brown coloured polymer which is a result of conjugation of the polymer backbone.

The interfacial transition zone between fluoropolymeric powder/white cement and steel and polymeric fibres (high density polyethylene/polypropylene, poly(vinyl alcohol), PEI, PVDF, and Nylon 6.6) was studied at short range using ^{19}F, ^{27}Al, and ^{43}Ca NMR spectroscopy and at long range using the scanning electron microscopy/energy dispersive spectroscopy method. It was concluded that the chemistry of polymeric fibres themselves can alter the surrounding interfacial transition zone such that the calcium silicate hydrate favours a tobermorite or jennite-like structure, which could contribute to a strong or weak interface.

List of Abbreviations and Symbols Used

ACD	Advanced Chemistry Development
ACK	Aveston-Cooper-Kelly
ASTM	American Society of Testing and Materials
C	calcium oxide
CH	calcium hydroxide
CSH	calcium silicate hydrate
$C\bar{S}H_2$	gypsum
C_3A	tricalcium aluminate
C_4AF	tetracalcium aluminoferrite
$C_6A\bar{S}_3H_{32}$	ettringite
C_2S	dicalcium silicate
C_3S	tricalcium silicate
Ca/Si	calcium to silicon ratio
CP	cross-polarization
E1cB	elimination by conjugate base
E2	bimolecular elimination
EDS	energy dispersive spectroscopy
EVA	poly(ethylene-vinyl acetate)

FT	Fourier transform
HDPE	high density polyethylene
HOMO	highest occupied molecular orbial
IR	infrared
ITZ	interfacial transition zone
LDPE	low density polyethylene
LUMO	lowest unoccupied molecular orbital
MAS	magic angle spinning
NMR	nuclear magnetic resonance
PEI	poly(ether imide)
PFA	poly(tetrafluoroethylene-co-perfluoropropyl vinyl ether)
PP	polypropylene
PVA	poly(vinyl alcohol)
PVDF	poly(vinylidene fluoride)
SEM	scanning electron microscopy
S_N2	nucleophilic substitution 2
SPE	single pulse excitation
TPPM	two pulse phase modulation
UV-Vis	ultraviolet-visible
w/c	water to cement ratio

E	Young's modulus
E_c	Young's modulus of composite
E_f	Young's modulus of fibre
ϵ	strain
ϵ_{cu}	ultimate strain on composite
ϵ_{mc}	strain at end of multiple cracking zone
ϵ_{mu}	ultimate strain on matrix
k	rate constant
k_p	pseudo-rate constant
$R_{Ca(CH_3COO)_2}$	ratio of integrated NMR intensities for the carbonyl and methyl group peaks in calcium acetate
R_{EVA}	ratio of integrated NMR intensities for the carbonyl and methyl group peaks in EVA
σ	stress
σ_{cu}	ultimate stress on composite
σ_{fu}	ultimate stress on fibre
σ_{mu}	ultimate stress on matrix
τ	interfacial bond strength
τ_c	critical bond strength
V_f	fractional fibre content
[C=O]	concentration of carbonyl
$[Ca(OH)_2]$	concentration of calcium hydroxide

Acknowledgements

I would like to thank Dr. Josef Zwanziger for his supervision and support. I would also like to thank my supervisory committee: Dr. Mary Anne White, Dr. Heather Andreas, and Dr. Dean Forgeron. I would like to thank the Zwanziger group for their friendship and support; especially Hannah Le, who made several samples of dehydrofluorinated PVDF powder and acquired the UV-Visible spectroscopic data presented in this dissertation, and Amy Trottier, for the numerous fruitful discussions throughout our work together on the fibre reinforced concrete project.

I am grateful to Dr. Ulrike Werner-Zwanziger, Dr. Banghao Chen, James Longstaffe and the Nuclear Magnetic Resonance Research Resource (NMR3) for assistance with the solid state NMR spectrometers and many helpful discussions. I am grateful to Dr. Victor Terskikh and Dr. Eric Ye for their assistance with the ^{43}Ca data aquisition on the 900 MHz NMR spectrometer. Access to the 900 MHz NMR spectrometer was provided by the National Ultrahigh-Field NMR Facility for Solids (Ottawa, Canada), a national research facility funded by the Canada Foundation for Innovation, the Ontario Innovation Trust, Recherche Québec, the National Research Council Canada, and Bruker BioSpin and managed by the University of Ottawa (www.nmr900.ca). The Natural Sciences and Engineering Research Council of Canada (NSERC) is acknowledged for a Major Resources Support grant.

I would like to thank Kelly Resmer and Felix Meier-Stephenson and their respective supervisors, Dr. Robert White and Dr. Donald Weaver, for access to the freeze driers and their assistance carrying out lyophylization procedures in this work. I would like to thank Mike Boutlier and Rick Conrad for their assistance with building the vacuum impregnation set-up, Andy George for access and assistance with the diamond saw and polisher, Ping Li for sputter coating my SEM samples, and Patricia Scallion for access and assistance with the SEM.

I would like to thank the Natural Science and Engineering Council (NSERC) for CGS-M and PGS-D awards and the Atlantic Innovation Fund, NSERC and Dalhousie University for funding.

I am forever grateful to my husband, Norm, parents, Colleen and Gerard, and brother, Derek, for their endless supply of love and support.

Chapter 1

Introduction

1.1 Preamble

For the reader's convenience, this dissertation will refer to cement components with their appropriate cement chemistry symbol throughout the text. Chemical reactions will be reported using chemical formulae rather than cement chemistry symbols. Table 1.1 summarizes the conversion between nomenclatures.

Table 1.1: Cement chemistry abbreviations

Abbreviation	Component Name	Chemical Formula
C	calcium oxide	CaO
CH	calcium hydroxide	$Ca(OH)_2$
$C\bar{S}H_2$	gypsum	$CaSO_4 \cdot 2\,H_2O$
CSH	calcium silicate hydrate	$(CaO)_x \cdot SiO_2 \cdot yH_2O$*
C_3A	tricalcium aluminate	$3\,CaO \cdot Al_2O_3$
C_4AF	tetracalcium aluminoferrite	$4\,CaO \cdot Al_2O_3 \cdot Fe_2O_3$
C_2S	dicalcium silicate	$2\,CaO \cdot SiO_2$
C_3S	tricalcium silicate	$3\,CaO \cdot SiO_2$
$C_6A\bar{S}_3H_{32}$	ettringite	$C_3A \cdot 3\,CaSO_4 \cdot 32\,H_2O$

*x<1.5

This chapter serves as an introduction to cement chemistry, concrete, reinforced concrete, and polymeric fibres used in concrete reinforcement applications. Chapter 2 outlines the experimental methods, Nuclear Magnetic Resonance (NMR) spectroscopy, Scanning Electron Microscopy/Energy Dispersive Spectroscopy (SEM/EDS),

Infrared (IR) spectroscopy, and Ultraviolet-Visible (UV-Vis) spectroscopy, used in this work. Chapter 3 discusses the hydrolysis kinetics of a chemical admixture, poly(ethylene-vinyl acetate) (EVA), in a hydrating white cement environment over 84 days via ^{13}C NMR spectroscopy. Chapter 4 examines poly(ether imide) (PEI) as a possible concrete reinforcement material with ^{13}C NMR spectroscopy. Chapter 5 addresses poly(vinylidene fluoride)'s (PVDF) stability in cementitious matrices using ^{13}C and ^{19}F NMR, IR, and UV-Vis spectroscopies. Chapter 6 discusses the interfacial transition zone surrounding steel and polymeric materials (powder and fibre) at short (angstrom scale) and long (micron scale) range from the interface. Chapter 7 presents the overall conclusions, recommendations, and future directions for this work.

1.2 Introduction

The purpose of this dissertation is to explore the chemical interactions between polymeric powder or fibre and white cement. It is hypothesized that the chemical interactions between polymeric fibres and concrete create additional bonding. The goal of this thesis is to experimentally test this hypothesis. Using nuclear magnetic resonance (NMR) spectroscopic and scanning electron microscopic (SEM) methods, the chemical interactions between polymeric powder and white cement (model system for NMR experiments) and polymeric fibres/white cement (model system for SEM experiments) were investigated. NMR was used to study the chemical stability of poly(ethylene-vinyl acetate) (EVA), poly(vinylidene fluoride) (PVDF)(infrared (IR), and ultraviolet-visible (UV) spectroscopies were also used in the PVDF study),

and poly(ether imide) (PEI) in cementitious matrices. It was found that EVA and PEI polymers undergo hydrolysis and PVDF undergoes dehydrofluorination in the cementitious environment which could be detrimental to a fibre's ability to toughen concrete if it is composed of these materials. It is speculated that fibre composition induces structural changes in the interfacial transition zone surrounding the fibre, thus ultimately having an effect on the bond created between polymeric fibres and a concrete matrix.

Concrete, due to its low cost, durability and fire resistance, is one of the world's most widely used construction materials. The world consumes approximately 10 billion tonnes of engineering materials (ceramics, metals, natural, and polymers) each year [1]. The consumption of concrete exceeds the consumption of all other engineering materials combined. For comparison purposes, ceramics (dominated by concrete), natural (*e.g.*, wood), metals (dominated by steel), and polymers (*e.g.*, PE and PP) make up 84%, 9%, 6%, and 1% of engineering materials consumed each year, respectively [1].

Concrete structures are typically reinforced using steel rebar and welded wire mesh. The major drawbacks when using rebar to reinforce concrete structures are cost and corrosion. With high steel prices and the world's aging concrete structures, which cost billions of dollars to repair each year, alternative concrete reinforcement methods need to be investigated. Since corrosion is a significant contributor to structural failure, it would be advantageous to find an alternative reinforcement material to not only replace steel reinforcement but also be corrosion resistant.

Over the past few decades, asbestos, steel, natural, and synthetic (polymeric) fibres have been used as reinforcement in concrete. Due to asbestos related health concerns [2] and rising steel prices, the fibre industry is turning to synthetic fibres as a reinforcement material. One important characteristic of a fibre, which is necessary for good performance in a concrete matrix, is the bond between fibre and concrete. There are two types of bonding that can occur at the polymeric fibre/concrete interface: mechanical and chemical. Mechanical bonding at the interface has been studied extensively in the literature [3–12]; however, chemical bonding at the interface is not well understood. The industry currently lacks understanding of the chemical interactions between synthetic fibres and concrete; as a result, the development of new high performance fibre for concrete reinforcement has lost momentum.

Chemical bonding at the polymeric fibre/concrete interface is an important factor in a fibre's performance in concrete reinforcement applications. Knowing which polymer chemistries best interact with the concrete will guide the choice of appropriate polymers and give some direction toward the chemical alteration of the fibres if required. To investigate the interfacial interactions between polymer fibres and concrete, on the small scale (angstroms from the interface) solid state NMR spectroscopy was employed to probe local interactions of the nuclei present at the polymeric powder and white cement interface. On the larger scale, SEM/EDS was used to examine the interfacial transition zone surrounding steel and polymeric fibres up to 200 μm (2×10^6 angstroms) from the fibre surface. The chemical bond of potential polymers

with concrete can be studied, prior to fibre production, to optimize the polymer selection process which could lead to new fibre blends and surface treatments to enhance the bond between the fibre and concrete.

The long term stability of polymeric material in a cementitious environment is important to consider when choosing a fibre for concrete reinforcement applications. The harsh basic environment in cementitious matrices can lead to chemical degradation of fibres by processes such as hydrolysis, which can damage fibre surfaces, cause reduction in mechanical properties of the fibre, and in extreme cases cause premature fibre failure. In this work, the chemical stability of an EVA admixture and both polymeric materials (PVDF and PEI) chosen by Trottier [13] as potential polymeric materials for reinforced concrete applications were studied via NMR, IR, and UV-Vis spectroscopic methods.

1.3 Cement Production

Cement is produced from four essential oxides of calcium (CaO), silicon (SiO_2), aluminum (Al_2O_3), and iron (Fe_2O_3). Limestone is used as the calcium source and clay as a source of silicon, aluminum, and iron. The raw materials are blended in the following proportions of approximately 63% calcium oxide, 20% silica, 6% alumina, 3% iron (III) oxide, and small portions of other materials [14]. The blended raw materials are transported from the quarry to the factory where they are pulverized by a roller on a rotating table. After being crushed, the material passes through a series of vertical chambers which pre-heat the material before entrance to the kiln. The kiln

is a large, sloped, rotating furnace which completes 1-3 revolutions per minute. Since the kiln is sloped, the material is gradually heated as it moves toward the flame heat source located at the end of the kiln. As the material is heated, water and carbon dioxide are expelled and consequently reactions are produced among the remaining solids as they are agitated due to the kiln rotation [14]. The CaO reacts with the silica and alumina to form calcium silicates and calcium aluminates. At a temperature of approximately 1250°C, tricalcium silicate (C_3S), the major component of cement, begins to form. At 1500°C, C_3S represents 40-70% of the final cement powder product. At the end of the kiln, the material is partially molten and is typically called clinker. The clinker is then cooled on a grate using forced air. After cooling, the clinker is ground in a ball mill to reduce the particulate size to a fine powder with an average size of 15 μm [15]. At the grinding stage, gypsum ($C\bar{S}H_2$) is added which, during the hydration process, controls flash setting (rapid reaction of C_3A that causes the loss of cement paste workability) of the cement.

1.4 Cement Hydration

Cement hydration occurs in a series of complex chemical reactions which are still not fully understood [14, 16, 17]. To simplify this complex process, cement hydration can be described in four stages: pre-induction; induction; acceleration; and deceleration. When water is added to cement, a brief period of heightened hydration occurs and is called the pre-induction stage. During this stage, alkali earth oxides quickly dissolve in water which results in the formation of calcium hydroxide ($Ca(OH)_2$) and

calcium silicate hydrate (CSH) gel. Taylor [14] describes the formation of $Ca(OH)_2$ and CSH gel by the following chemical reaction (Equation 1.1):

$$2\,(3\,CaO{\cdot}SiO_2)(s) + 6\,H_2O(l) \longrightarrow 3\,CaO{\cdot}2\,SiO_2{\cdot}3\,H_2O(s) + 3\,Ca(OH)_2(aq). \quad (1.1)$$

It is also proposed that tricalcium aluminate (C_3A) and tetracalcium aluminoferrite (C_4AF) undergo hydration by the following reactions (Equations 1.2 and 1.3):

$$3\,CaO{\cdot}Al_2O_3(s) + 6\,H_2O(l) \longrightarrow 3\,CaO{\cdot}Al_2O_3{\cdot}6\,H_2O(s) \quad (1.2)$$

and

$$4\,CaO{\cdot}Al_2O_3{\cdot}Fe_2O_3(s) + 2\,Ca(OH)_2(aq) + 10\,H_2O(l) \longrightarrow$$
$$3\,CaO{\cdot}Al_2O_3{\cdot}6\,H_2O(s) + 3\,CaO{\cdot}Fe_2O_3{\cdot}6\,H_2O(s). \quad (1.3)$$

Gypsum is added during cement production to prevent flash setting. The reaction of gypsum with C_3A, shown below (Equation 1.4), is responsible for slowing the setting time of cement by the formation of calcium trisulfoaluminate hydrate,

$$3\,CaO{\cdot}Al_2O_3(s) + 3\,CaSO_4(s) + 32\,H_2O(l) \longrightarrow$$
$$3\,CaO{\cdot}Al_2O_3{\cdot}3\,CaSO_4{\cdot}32\,H_2O(s). \quad (1.4)$$

Following the pre-induction stage, the induction stage begins with a significant reduction in the rate of hydration. One hypothesis that has been suggested to account for the hydration rate reduction is that the CSH gel layer covers the C_3S which would prevent the aqueous C_3S from undergoing hydration [14]. The induction period typically lasts several hours. After the induction stage, the rate of hydration increases again. During the acceleration stage, the hydration of C_2S begins to proceed very slowly while the hydration of C_3S becomes more rapid. At this point in the hydration process there is a large concentration of solid hydration products present which results in the remainder of the cement hydration process being diffusion controlled. This final stage of hydration, referred to as deceleration, continues for many years. The overall cement hydration process is represented graphically in Figure 1.1.

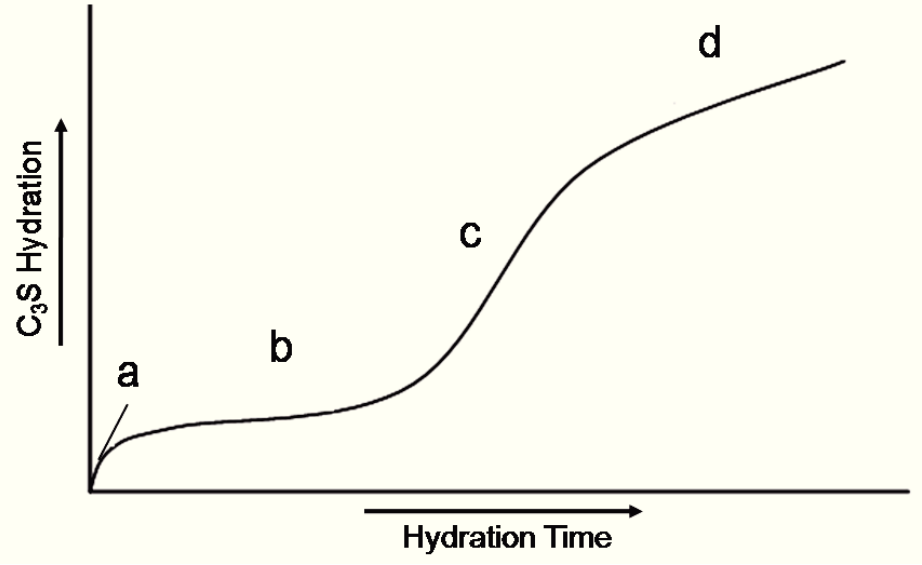

Figure 1.1: Representation of C_3S hydration in cement: (a) pre-induction, (b) induction, (c) acceleration, and (d) deceleration. Styled after [16, 17].

During hydration, amorphous CSH forms as a result of C_3S and C_2S hydration. It has been proposed that the CSH formed during hydration resembles the structure of tobermorite and jennite minerals [14, 16]. The chemical structures of 1.4 nm tobermorite and jennite are shown in Figures 1.2 and 1.3, respectively. Tobermorite, $[Ca_4(Si_3O_9H)_2]Ca \cdot 8\,H_2O$, consists of a layered structure that includes two silicate chain layers, a CaO_2 sublayer, and a $Ca \cdot 8\,H_2O$ interspace layer. Tobermorite exists in two forms, 1.4 nm and 1.1 nm tobermorite. 1.1 nm tobermorite, $[Ca_4(Si_3O_9H)_2]Ca \cdot 4\,H_2O$, can be formed from 1.4 nm tobermorite via the loss of interspace water by heating at 55°C [14]. Jennite, $[Ca_8(Si_3O_9H)_2(OH)_8]Ca \cdot 6\,H_2O$, has a similar layered structure to tobermorite, although, there are differences in the sub and interspace layers. The jennite sublayer is composed of CaO−OH and the interspace layer contains less water than 1.4 nm tobermorite. As was described previously for tobermorite, upon heating to 70-90°C, jennite also loses interspace water to form meta-jennite.

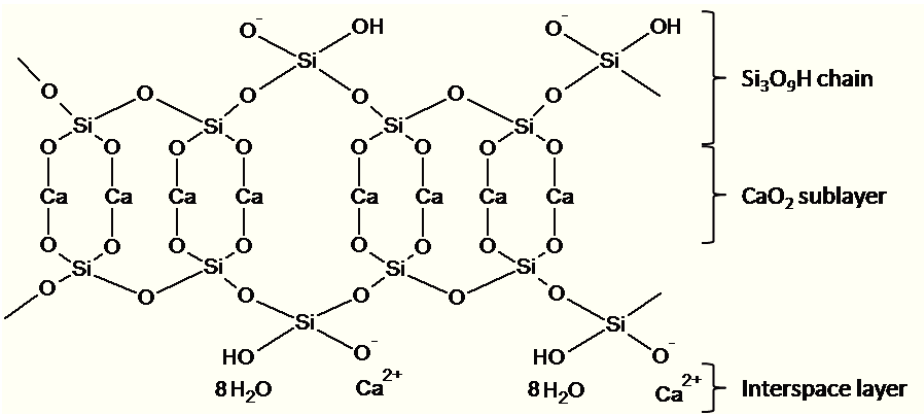

Figure 1.2: Chemical structure of tobermorite. Styled after Hewlett [16]

CSH is the major strength component of the cementitious matrix, acting to bridge

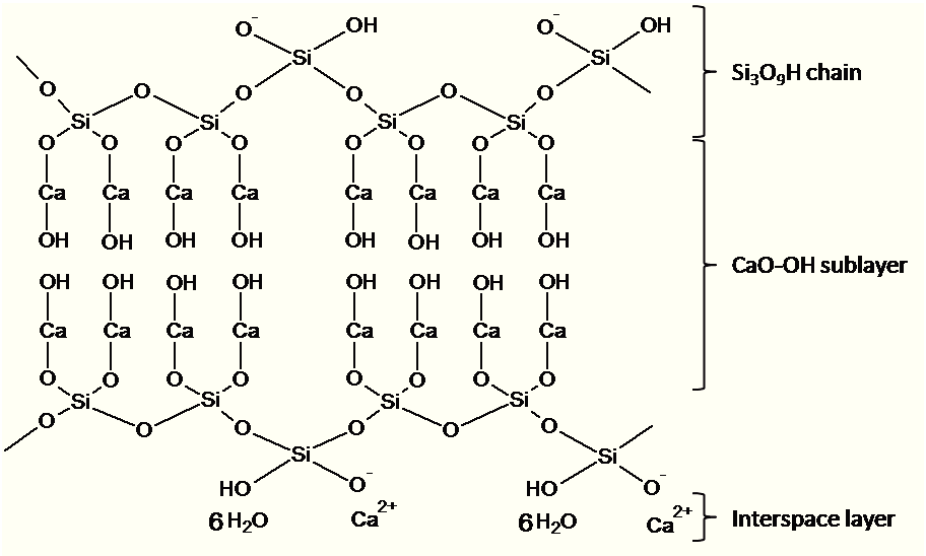

Figure 1.3: Chemical structure of jennite. Styled after Hewlett [16]

pores and bind together aggregate. To avoid structural damage to the CSH formed during hydration of the cement samples discussed in this dissertation, all drying steps in the sample preparation were carried out below 50°C.

1.5 Concrete

Cement is a powdered material which sets and hardens in the presence of water to form a hardened cement paste. As a result of these properties, cement is commonly used as a binder between materials. For instance, bricks are cemented together with mortar, which is composed of cement paste and fine aggregate, typically natural or manufactured sand having a particulate size less than 10 mm [18]. Concrete is composed of Portland cement, water, aggregate, and in some cases chemical admixture. Concrete contains course aggregate as well as fine aggregate. Course aggregate (*e.g.*, crushed gravel or stone) is typically between 10 to 38 mm in diameter [18].

Due to cost considerations, only the amount of cement required to bind the aggregate together is added to the concrete mixture. Therefore, aggregate is the major component (60-75% by volume) of the concrete mixture. Prior to using aggregate, it must be sufficiently cleaned to remove any organic or mineral materials which can degrade the concrete product. Aggregate shape is also an important consideration for the properties of the freshly mixed concrete as well as its hardened properties. For instance, aggregate which is highly textured and elongated in shape will require more water to achieve flow than rounded less textured aggregate. Admixtures can be used in concrete to achieve desired effects such as retarding and corrosion inhibition [15]. In warm environments, for example, concrete tends to harden more rapidly which makes placing the concrete difficult. Using a retarding admixture can slow down the setting which allows for longer periods of workability before the initial setting occurs. The use of corrosion inhibiting admixtures is desirable when steel is used to reinforce the concrete structure. These admixtures can be used to defend against corrosion of steel in environments which have high chloride levels (*e.g.*, marine environments).

1.5.1 Water to Cement Ratio

The water to cement ratio (mass of water/mass of cement) is vital to the strength of hardened concrete. When mixing concrete, water is typically added to cement at a volume that exceeds the amount needed for hydration reactions to occur. Adding extra water improves concrete workability thus allowing for sufficient flow of the material which is essential for reducing the quantity of pores in the hardened paste; however,

strength is often sacrificed. Consider the schematic cement pastes in Figure 1.4. Figure 1.4a depicts a cement paste mixed with a low water to cement (w/c) ratio, for example, less than 0.3, where the blue areas represent water and white represent cement particles. Upon hydration, a cement paste with small pores, shown in black in Figure 1.4b, approximately 2 to 3 μm in size, densely packed CSH hydration products (shown in grey) and some unhydrated cement grains, as a result of low quantities of water available for hydration, is formed. Figure 1.4c demonstrates a cement paste having been mixed with a high w/c ratio (greater than 0.6). Following hydration (Figure 1.4d), the hardened cement paste is characterized by large interconnected pores (approximately 10 μm in size, pictured in black), few small unhydrated cement grains (shown in white), and CSH hydration products (shown in grey).

Increasing the w/c ratio can make mixing, placing, and compacting fresh concrete more convenient, as the wet concrete is more fluid and workable. This benefit is largely outweighed by the negative effects an increased w/c ratio causes in the composite. Despite the fact that increasing the w/c ratio will decrease the proportion of unhydrated cement grains in the composite, it is coupled with an increase in porosity that makes the composite more permeable which can be detrimental to steel reinforcement that is protected from the elements by the surrounding concrete. Also, as a result of increased porosity, the compressive strength of the composite decreases with increasing w/c ratio since CSH cannot bridge the larger pores, therefore restricting the formation of concrete strengthening CSH bonds. A general curve, shown in Figure 1.5, expresses the graphical relationship between concrete strength and w/c

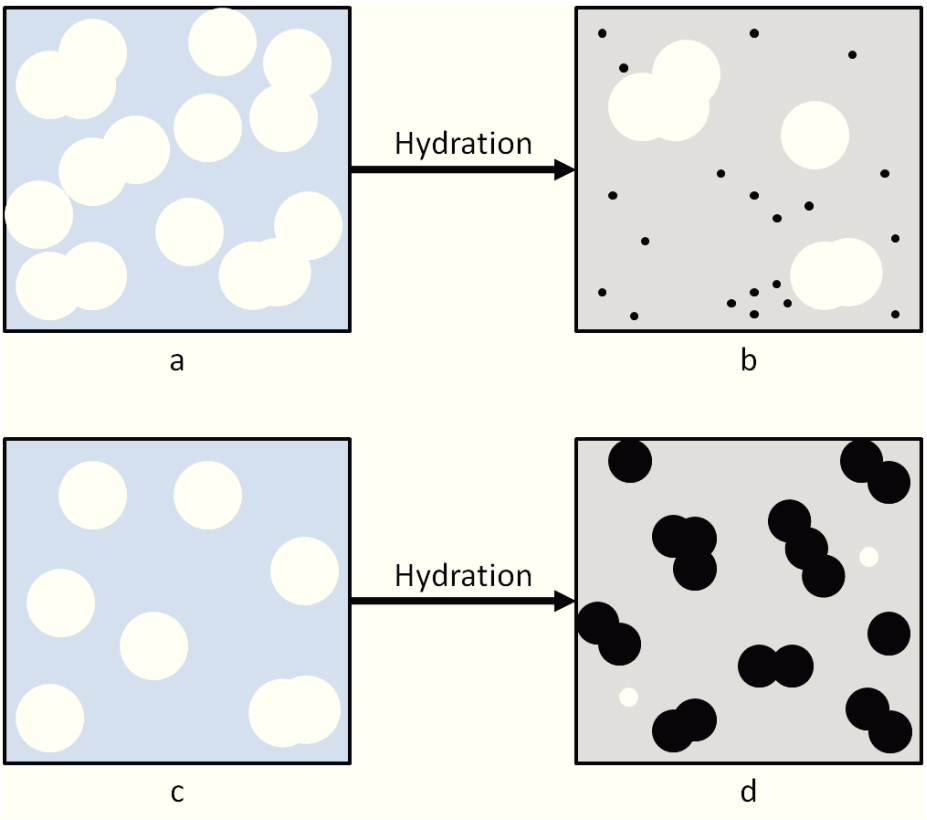

Figure 1.4: Effect of water to cement ratio on hardened cement paste. (a) fresh cement paste with low water to cement ratio,(b) hardened cement with low water cement ratio, (c) fresh cement paste with high water to cement ratio, and (d) hardened cement with high water to cement ratio. The colours blue, white, grey, and black indicate water, unhydrated cement grains, hydrated cement paste, and pores, respectively.

ratio.

1.6 Reinforced Concrete

1.6.1 Why Does Concrete Need Reinforcement?

The American Society of Testing and Materials (ASTM) defines the strength of a material as the maximum force (*e.g.*, load, stress or strain) that it can withstand without deformation or structural failure [19]. Concrete, in its hardened state, has

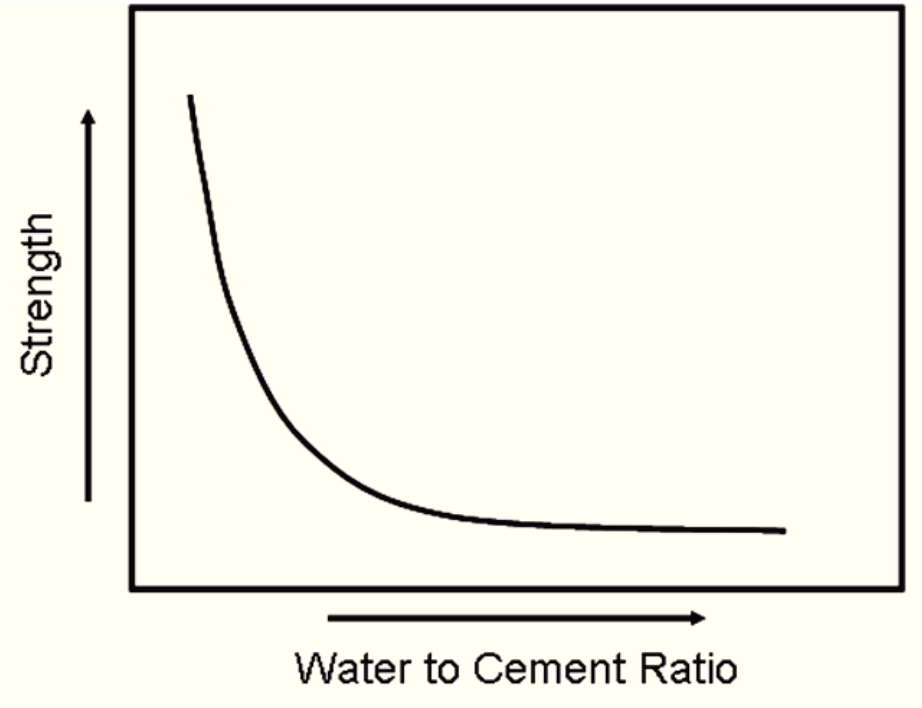

Figure 1.5: Effect of water to cement ratio on cement strength. Styled after Hewlett [16].

a high compressive strength (35 MPa) [20, 21]; however, it is also brittle, prone to cracking and has a tensile strength of approximately 10% of its compressive strength. Tensile strength is defined as the maximum load a material can withstand before it fractures divided by the initial cross-sectional area of the material [22]. When designing concrete structures, it is assumed that the concrete can withstand compressive stress but not tensile stress. Therefore, concrete structures that will be placed under tensile stress must be reinforced to avoid cracking and ultimately structural failure.

1.6.2 Steel Reinforcement

Concrete has low tensile strength; therefore, it is typically reinforced in areas with excessive tensile stress. This is of particular importance in concrete elements

such as beams (*e.g.*, in a roof) or a concrete slab in a bridge. When concrete is suspended, as pictured in Figure 1.6, the horizontal beam or slab experiences both compressive and tensile strength under its own weight. The compressive stress is experienced in the upper portion of the concrete while the under side of the concrete element is stretching apart in tension. Since concrete's tensile strength is poor in comparison to its compressive strength, if it is not reinforced in the region experiencing tensile stress, the structure will crack under its own weight (as seen in Figure 1.6a) leading to premature failure of the structure. By placing steel rebar in the concrete during casting, the hardened reinforced composite can withstand both compressive and tensile stresses, as the steel rebar (which has a tensile strength of approximately 275-500 MPa) can absorb the tensile stress and prolong the life of the structure.

To enhance the bond between the steel and concrete, the bars are typically deformed by having raised patterns rolled onto their surface. An advantage of using steel as a concrete reinforcement is that steel and concrete have similar coefficients of thermal expansion, thus they react in a similar manner to temperature fluctuations [23]. The fire resistant quality of concrete protects the steel reinforcement in the event of a fire. Although using steel as a concrete reinforcement has many advantages, there are also some drawbacks. One of the main issues with using steel as a concrete reinforcement is that it is susceptible to corrosion due to the presence of salts in marine areas and, in cold climates, de-icing salts. The high cost of steel and steel fibres has lead to the study and production of synthetic fibres to be used as a replacement for steel fibres and rebar as concrete reinforcement. It has been shown

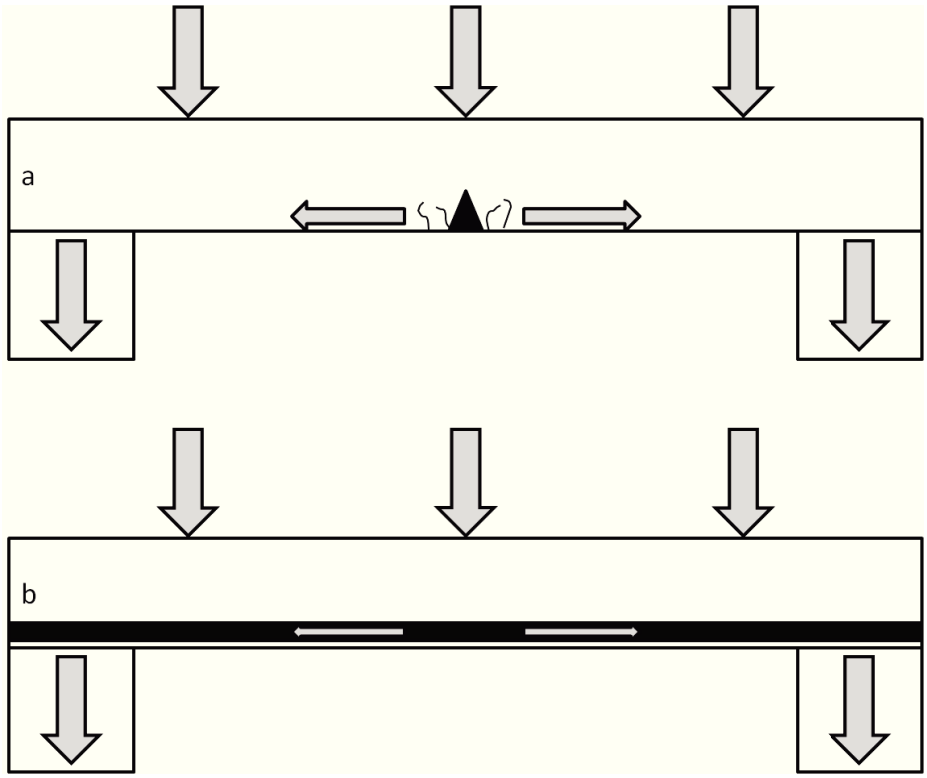

Figure 1.6: Effect of steel reinforcement in concrete in areas experiencing tensile stress.

that polymeric fibre reinforcement has been successful in replacing some low level reinforcement (secondary reinforcement), such as in bridge decks [24, 25]. Further research is required to better understand the bond between concrete and polymeric fibres. The long term goal in industry is to develop an ultra high performance, cost effective polymeric fibre which is capable of replacing steel reinforcement.

1.6.2.1 Bentur's Model of the Steel Fibre Concrete Interface

Bentur and co-workers [26] used scanning electron microscopy to study the steel fibre concrete interface. They described an interfacial transition zone between the steel fibre and bulk concrete which is porous and rich in $Ca(OH)_2$. Figure 1.7 shows

a schematic representation of the steel fibre concrete interface. It was estimated by Bentur *et al.* [26] that the transition zone is 50 to 100 μm in thickness and is composed of CSH, ettringite ($C_6A\bar{S}_3H_{32}$) and $Ca(OH)_2$. The interfacial transition zone is characterized by a 1 to 2 μm thick duplex film that is in direct contact with the fibre surface, followed by a 10 to 30 μm thick layer which is occupied by massive $Ca(OH)_2$ deposits. The $Ca(OH)_2$ layer is backed by a porous layer which becomes denser as it approaches the bulk matrix.

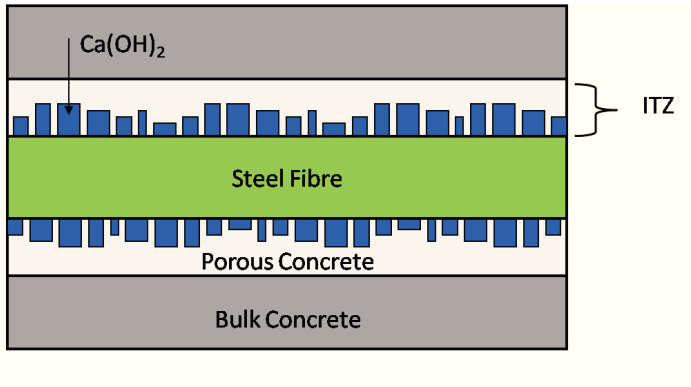

Figure 1.7: Bentur's model of the steel fibre/concrete interface, where ITZ is the interfacial transition zone. Styled after Bentur *et. al.* [26].

1.6.3 Synthetic Fibre Reinforcement

The intrinsic properties of the fibres themselves have an effect on their ability to reinforce concrete. Some important properties to be considered when choosing a fibre for concrete reinforcement are tensile strength, modulus of elasticity, and the bond with the concrete matrix.

The fibre content is usually less than 1% (by volume) in a concrete matrix, thus only a small fraction of the fibre is in contact with the cementitious matrix. The

modulus of elasticity, or Young's modulus (E), is a measure of a material's stiffness (see Equation 1.5), where σ is the stress and ϵ is the strain on the material.

$$E = \frac{\sigma}{\epsilon} \tag{1.5}$$

Fibres possessing a high modulus are ideal for reinforced concrete applications (polymeric fibres: approximately 10-20 GPa) as the fibres will carry the entire load when bridging a crack in the concrete matrix.

The mechanical behaviour of a fibre reinforced concrete composite can be described as three stages in a tensile stress-strain curve (shown in Figure 1.8), as described by the ACK model [26, 27]. These stages include: (a) the elastic stage; (b) the multiple cracking stage; and (c) the post-multiple cracking stage. In the elastic stage, both fibre and concrete matrix are within their elastic range with a Young's modulus, E_c. When the strain on the fibre reinforced composite exceeds that of the concrete matrix, the first crack occurs at stress, σ_{mu}, and strain, ϵ_{mu}, beginning the multiple cracking stage. During the multiple cracking stage, fibres act to alleviate stress in the concrete matrix by accepting load on fibres bridging the cracks, thus controlling crack formation. Over time, further cracking occurs and the composite is multiply cracked with bridging fibre reinforcement. At the end of the multiple cracking stage (ϵ_{mc}), the post-multiple cracking stage begins, fibres are stretched and pulled out of the concrete matrix. In an ideal case, the slope of the stress-strain curve in the post-multiple cracking region would be $E_f V_f$, where E_f is the Young's modulus

of the fibre and V_f is the fractional fibre content. When the load bearing capacity of the composite (ϵ_{cu}) and ultimate tensile stress of the fibre (σ_{fu}) are reached, failure occurs. The black curve in Figure 1.8 represents an ideal case of fibre reinforced concrete in which toughness (area under the stress-strain curve) of the composite is increased. In contrast, in plain concrete, as shown in the orange curve in Figure 1.8, the composite fails shortly after the first crack occurs at maximum stress and strain. The blue curve in Figure 1.8 depicts a stress-strain curve for a typical fibre reinforced composite containing fibres of low load bearing capacity.

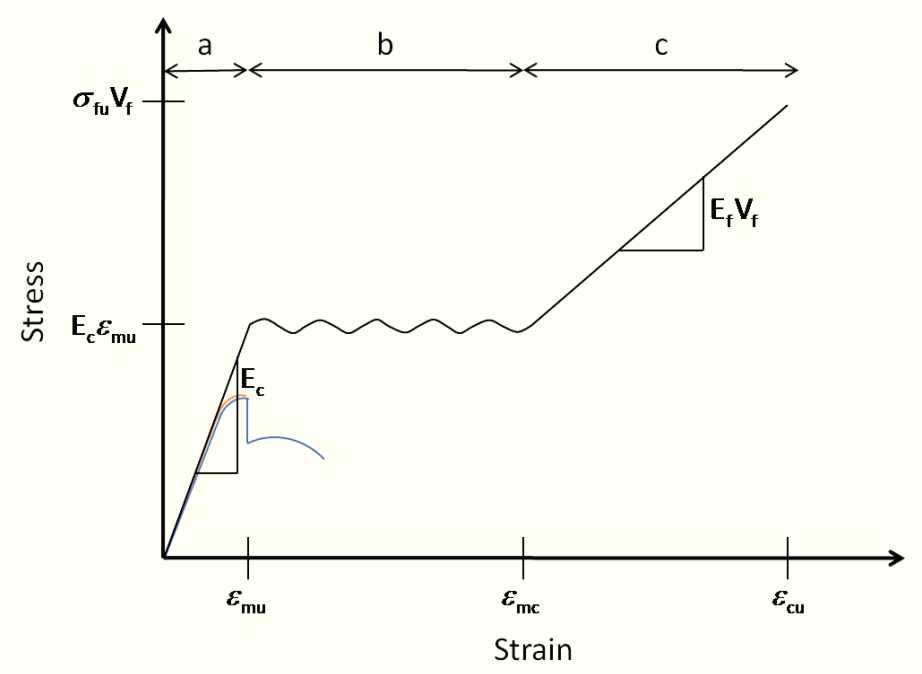

Figure 1.8: Tensile stress-strain curve for fibre reinforced concrete. The letters (a), (b), and (c) indicate the elastic, multiple cracking, and post-multiple cracking stages, respectively (based on the ACK model [27] and styled after Bentur *et al.* [26]). The black, orange, and blue curves represent an ideal fibre reinforced composite, plain concrete, and a fibre reinforced composite with low load bearing capacity.

Toughness, unlike strength which is a measure of the stress required to break a

material, is defined as the energy required to break a material. In a stress-strain curve, the area under the curve indicates the toughness of the material. The bond between fibres and concrete is of utmost importance when determining a fibre's ability to toughen concrete. The relationship between toughness and the interfacial bond strength is shown in Figure 1.9. If the bond strength is less than the critical bond strength, τ_c, fibres pull-out of the matrix before they can contribute to the concrete composite toughness. An example of a fibre that exhibits weak bond with concrete is nylon [28, 29]. If the bond strength is greater than τ_c, the fibre tends to break before pulling out of the concrete, thus the toughness of the composite is limited by the strength of the fibre itself. An example of a fibre that exhibits a strong bond with concrete is poly(vinyl alcohol) (PVA) [5,30]. In the ideal case, a fibre with high tensile strength and a bond strength near but less than τ_c will result in a composite toughened by fibre which absorbs energy and slowly pulls out of the cementitious matrix.

1.6.3.1 Review of Polymeric Fibres Used as Concrete Reinforcement

In recent years, many polymeric fibres have emerged as suitable concrete reinforcement. A suitable reinforcement must have high tensile strength and high resistance to the harsh alkaline environment of concrete. The following section is a short review of current polymeric fibres used for concrete reinforcement. Table 1.2 gives the physical properties of synthetic fibres used in concrete reinforcement as well as steel and glass for comparison purposes. Synthetic fibres that have been used as a concrete

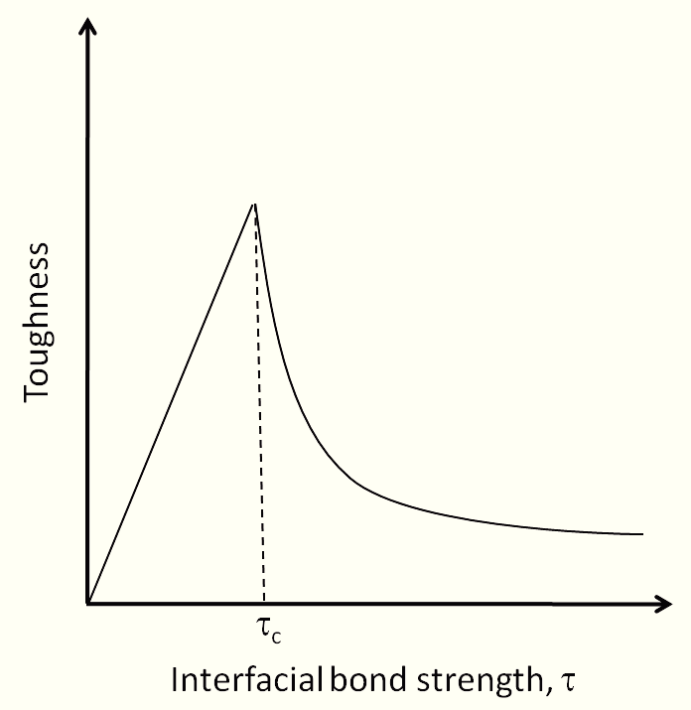

Figure 1.9: Toughness *vs.* interfacial bond strength in fibre reinforced concrete. Styled after Bentur and Mindess [26].

reinforcement over the past few decades include carbon, polyamide, polyester, acrylic, poly(vinyl alcohol), and polyolefin. Carbon fibres have high tensile strength (2.6 GPa) and elastic modulus (14-20 GPa) [31]. Carbon fibres are also highly resistant to the concrete alkaline environment and have a moderate bond with the concrete matrix. Although these properties are ideal for concrete reinforcement, the fibres are not used commercially because of their high cost.

Another alternative used is polyamide fibre. A common example of this fibre class is nylon. Polyamide fibres have a high tensile strength, resistance to alkaline environments, and, unlike carbon fibres, they are reasonably priced. The drawback to polyamide fibres is that they have low bonding with the concrete matrix [28, 29].

Table 1.2: Physical properties of fibres used for concrete reinforcement applications

Fibre	Elastic Modulus /GPa	Tensile Strength /GPa	Reference
acrylic	14-20	0.4-1.0	[20]
carbon	14-19.5	0.4-1.0	[31]
glass	80	2-4	[31]
Kevlar	133	2.8	[31]
nylon	4	0.9	[20]
polyester	41.8	0.3	[32]
polyethylene	5	0.2-0.3	[32]
polypropylene	5	0.5	[31]
poly(vinyl alcohol)	20-25	1.2-1.5	[20]
steel	200	1-3	[31]

Polyester fibres are hydrophobic in nature, thus the bonding with the concrete matrix is assumed to be purely mechanical; however, the bonding is low. The cost of the material is reasonable and its tensile strength and modulus of elasticity are relatively good. Despite these qualities, polyester fibres are susceptible to degradation in alkaline environments, via hydrolysis of ester linkages, making them unsuitable for concrete reinforcement [33].

Acrylic fibres typically have an elastic modulus between 14-20 GPa and tensile strength of 0.4-1.0 GPa. Acrylic fibres exhibit good bond with concrete; however, they are subject to hydrolysis of the nitrile groups in the basic cementitious environment.

Poly(vinyl alcohol) fibres, due to the presence of hydroxyl functional groups in their chemical structure, are hydrophilic which contributes to a strong bond between the fibre and concrete matrix. This strong bond can result in fracture of PVA fibres prior to pulling out of the concrete matrix, thus the fibre can no longer contribute to the composite toughness. PVA fibres, which have high eleastic modulus (20-25 GPa), were initially developed as a replacement for asbestos fibres [34,35] which were

phased out for use in fibre reinforced concrete applications due to the health risks they pose [2].

Polyolefin fibres, such as polyethylene and polypropylene, are hydrophobic and exhibit low bonding with the concrete matrix, but are highly resistant to the alkali cementitious environment. Polyethylene filaments are commonly made with low density polyethylene (LDPE) which is easier to produce and lower in cost in comparison to high density polyethylene (HDPE). Polypropylene fibres have a higher tensile strength (approximately 500 MPa) than polyethylene (approximately 200-300 MPa). Both polypropylene and polyethylene have low cost which makes them desirable materials for concrete reinforcement if the bonding issue can be addressed.

Trottier *et al.* [24, 36] developed a polyolefin fibre that is a blend of polypropylene and polyethylene. As mentioned previously, polyolefin fibres typically exhibit poor bonding in cementitious matrices; however, the current fibre addresses this concern [24, 37]. Due to the immiscibility of polypropylene and polyethylene, when the fibres are agitated through the concrete mixing process, they undergo progressive fibrillation. During mixing, the fibre maintains its monofilament character until the fibre is uniformly distributed throughout the cement, which avoids the undesirable balling effect. The fibrillation increases the fibre's surface area by approximately 20%, which increases the mechanical bond between the fibre and concrete. The current commercial fibre has strength of 650 MPa and Young's modulus of 9.5 GPa (the target for the next generation polymeric fibre is 15-20 GPa). The current fibre is shown to effectively improve crack resistance, crack control, thermal expansion, contraction

resistance and flexural toughness [24].

Chapter 2

Experimental Methods

This chapter serves as a brief introduction to nuclear magnetic resonance, infrared, and ultraviolet-visible spectroscopies and the scanning electron microscopy/energy dispersive spectroscopic technique, in the context used in this work.

2.1 Nuclear Magnetic Resonance Spectroscopy

Nuclear magnetic resonance (NMR) spectroscopy studies the interaction of nuclei in a sample with electromagnetic energy (in the radio-frequency range), while the sample is in the presence of an external magnetic field. The magnetic field splits the energy levels of the nuclear magnetic dipoles while local magnetic interactions shift them slighty. The result is a spectral fingerprint of the local bonding environment. In the liquid state, where molecules tumble rapidly, NMR spectra are typically well resolved and consist of sharp resonances. The high resolution is the result of orientational averaging as the liquid molecules tumble rapidly. In the solid state, however, samples are typically in a powdered form in which the crystallite orientations are static. Due to orientation dependent effects, solid state NMR spectra are generally broad in comparison to liquid state spectra and if spatial effects are not suppressed

it is sometimes impossible to extract useful structural data from the spectra.

An important source of both information and linebroadening in solid state spectra is chemical shift. The electrons near a nucleus are affected by the presence of the external magnetic field and circulate to produce a secondary field, which has the potential to alter the resonance frequency of the nucleus. The interaction of the secondary field and the nuclei results in chemical shielding and the shift in the resonance frequency caused by the field is called the chemical shift.

Dipole-dipole coupling is a direct through space interaction between one nuclear spin with the magnetic field generated by another nuclear spin. In the liquid state this effect is averaged away due to tumbling. In the solid state, on the other hand, nuclear spins are fixed in place and the dipolar interaction has a broadening effect on NMR spectra.

A quadrupolar nucleus (*e.g.*, ^{27}Al or ^{43}Ca) has an ellipsoid type shape and a nuclear spin greater than 1/2. Due to the non-spherical distribution of nuclear charge, quadrupolar nuclei interact with the electric field gradients in a molecule. This interaction also broadens the resultant NMR spectrum.

To achieve high resolution solid state NMR spectra it is necessary to remove the orientation dependent effects. In solid state NMR, this is routinely achieved by spinning the sample at the magic angle (54.74^{o}) to effectively reduce the spatial dependence of the chemical shielding anisotropy and dipolar coupling, which greatly enhances the quality of the NMR spectra. For half integer spin quadrupolar nuclei, of the type considered here, the first-order quadrupolar interaction vanishes for the

central transition.

2.1.1 Single Pulse Excitation and Cross-Polarization NMR

Single pulse excitation (SPE) NMR is a single resonance experiment in which the signal of the nucleus of interest is observed directly; for instance, in an SPE ^{13}C NMR experiment, a pulse is applied to all ^{13}C nuclei in the sample and the resultant spectrum consists of resonances corresponding to all ^{13}C species in the sample. SPE NMR experiments can be very time consuming for nuclei that have low natural abundance and/or long relaxation times. On the other hand, SPE is quantative in that all nuclei contribute to the signal, proportional to their population. Cross-polarization (CP) is a double resonance NMR technique that is typically used to observe dilute nuclei. Dilute nuclei, for example,^{13}C and ^{43}Ca, are low in natural abundance and often also have low gyromagnetic ratio and long relaxation times, all of which make observing these nuclei through SPE techniques difficult. The CP NMR technique exploits the dipole-dipole interactions between a high natural abundance and gyromagnetic ratio nucleus, which has a comparatively shorter relaxation time, and the dilute nucleus.

For instance, consider a CP NMR experiment between an abundant nucleus, ^{1}H, and dilute nucleus, ^{13}C (see Figure 2.1). A pulse is applied on ^{1}H and when both ^{1}H and ^{13}C nuclei precess at the same frequency satisfy the Hartmann-Hahn matching condition [38] (see Figure 2.2a) during a contact period (spin locking) [38], the magnetization can be transferred from ^{1}H (excited nucleus) to the ^{13}C (observed nucleus),

if the nuclei are coupled via dipole-dipole interactions. Figure 2.2b shows a schematic diagram of the build-up of magnetization as a function contact time. The drawback to CP is that it emphasizes nuclear pairs that are in close proximity and gives little signal for nuclei far from the abundant species. CP is therefore not quantitative.

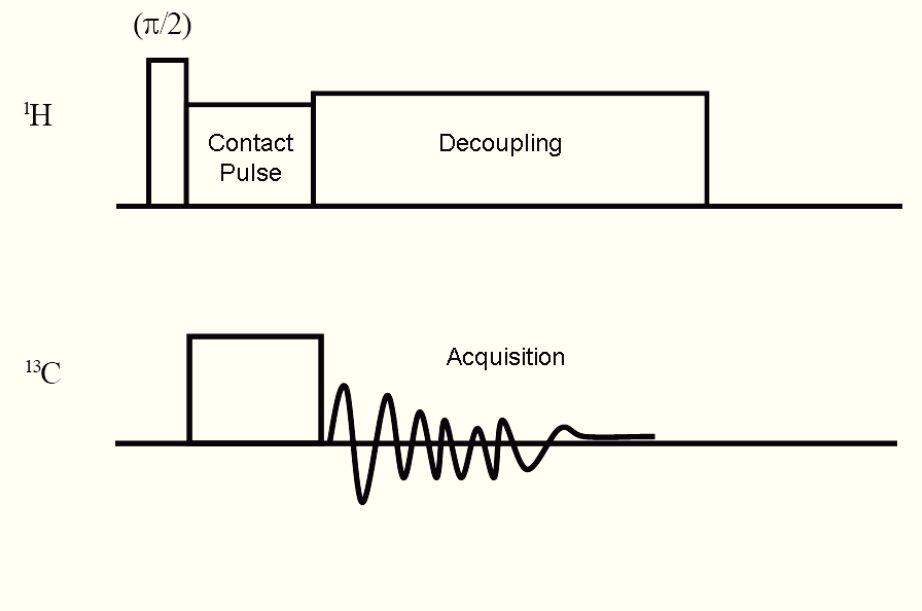

Figure 2.1: Cross-polarization schematic diagram. Styled after Duer [39].

Although the most common use of the CP NMR techniques is to observe dilute nuclei, it can also be used to obtain information about nuclei in close proximity to the excited nucleus. As discussed above, dipole-dipole coupling is a through-space interaction, therefore, nuclei which are in close proximity to the excited nucleus couple strongly, and a more intense CP signal is observed as a result of magnatization transfer than nuclei that are distant from the excited nucleus. It is speculated that by using the CP NMR technique the chemistry at the polymeric powder/white cement interface can be probed on the small scale (angstroms from the polymer surface), through the

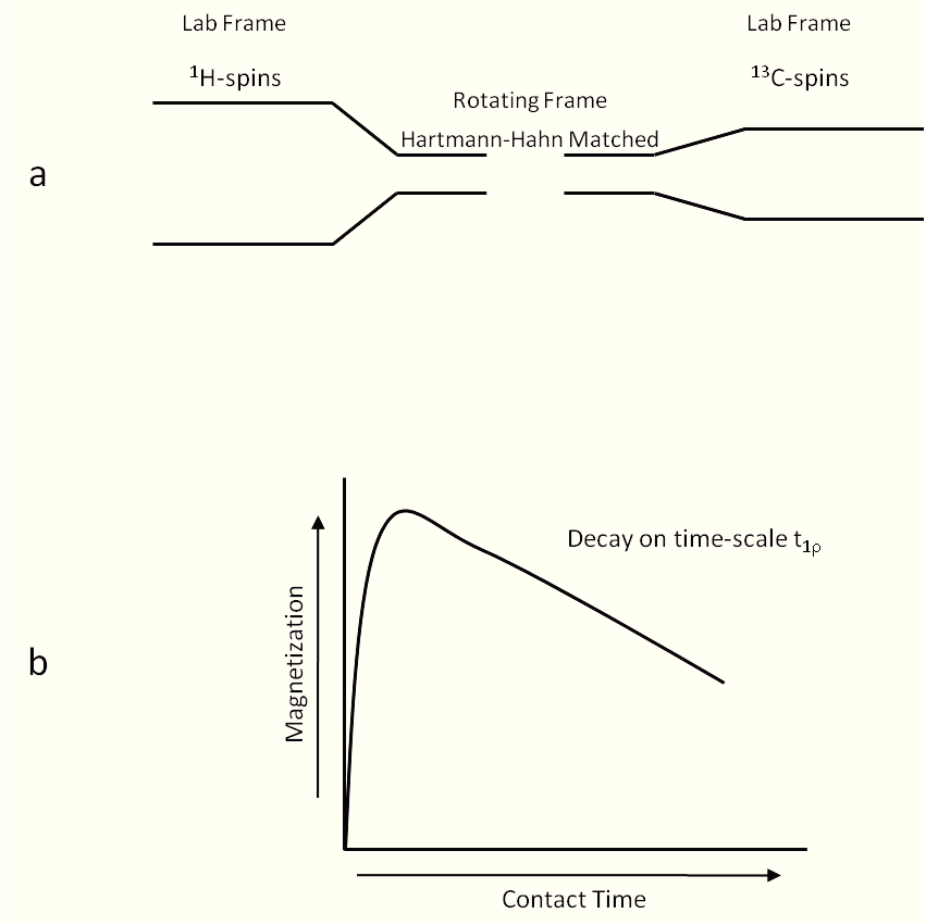

Figure 2.2: Hartmann-Hahn matching (a) and magnetization transfer in a cross-polarization NMR experiment (b). Styled after MacKenzie and Smith [40].

transfer of magnetization between different polymeric and cementitious nuclei.

Finally, both SPE and CP excitation methods can be combined with magic angle spinning to suppress chemical shift and quadrupolar broadening in order to yield maximal spectral resolution.

2.1.2 Choice of Cement for NMR Study

In the preliminary stages of this work, NMR samples were prepared using regular and white Portland cement. The major difference between regular and white cement

is highlighted in Table 2.1. White cement contains approximately 0.3% Fe_2O_3 while regular cement contains 2.0% Fe_2O_3, which imparts the grey colour of regular cement. Iron (Fe^{3+}), being paramagnetic, introduces unpaired electrons into the system which can be problematic for NMR studies. The unpaired electrons can couple with nuclei in the sample to significantly broaden NMR spectra. For this reason and as a result of preliminary testing, white cement was chosen as the cementitious matrix for this work as it is speculated that white cement behaves the same chemically as regular cement.

Table 2.1: Comparison of calcium, silicon, aluminum, and iron oxides in regular and white cement

Compound	Regular Cement (%)	White Cement (%)
CaO	63.1	65.5
SiO_2	21.1	22.5
Al_2O_3	5.3	4.42
Fe_2O_3	2.0	0.3

2.1.3 NMR Active Nuclei in Cement

In this work, a variety of nuclei present in cementitious materials and polymers were studied namely: ^{1}H, ^{13}C, ^{19}F, ^{27}Al, ^{29}Si, and ^{43}Ca.

Protons are abundant in cementitious matrices and present in many of the polymers studied in this work. Although ^{1}H is a spherical nucleus and is essentially 100% natually abundant, its strong homonuclear dipole coupling causes broad signals and prevents the determination of structural information. Since protons are of high natural abundance and are also abundant in the cementitious samples, protons were

excited and exploited via CP NMR experiments to enhance the observation of ^{13}C nuclei. ^{13}C is a common nucleus of study in NMR; however, it is plagued by its low natural abundance and is therefore often observed with the aide of CP NMR experiments. ^{19}F, which is present in the fluoropolymers used in this work (discussed in Chapters 5 and 6), is an easy nucleus to study with a 100% natural abundance and spherical shape. ^{27}Al nuclei, present in cementitious matrices, are 100% naturally abundant; however, these nuclei are difficult to study due to their large quadrupolar interactions which serve to broaden the NMR resonances. ^{29}Si nuclei have low natural abundance and long relaxation time which couple to create long data aquistion times. The ^{29}Si nucleus was studied in this work only for the EVA/white cement system (discussed in Chapter 3). Studying ^{43}Ca with NMR spectroscopy presents special challenges. Table 2.2 compares the nuclear properties of ^{43}Ca to the other nuclei studied in this work (^{1}H, ^{13}C, ^{19}F, ^{27}Al, ^{29}Si). ^{43}Ca has a natural abundance of 0.14% which is substantially less than that of ^{1}H (99.99%) and ^{13}C (1.07%). Not only does ^{43}Ca have low natural abundance, but it is also a quadrupolar nucleus and as such ^{43}Ca NMR spectra suffer from quadrupolar broadening. ^{43}Ca has a low Larmor frequency thus it is difficult to tune probes to achieve this frequency. With this in mind, as the magnetic field strength is increased, the frequency is higher and thus more easily tuned. All ^{43}Ca experiments presented in this dissertation were carried out at a magnetic field strength of 21.1 T.

Table 2.2: Comparison of ^{1}H, ^{13}C, ^{19}F, ^{27}Al, ^{29}Si, and ^{43}Ca nuclear properties [39,40]

Nucleus	Spin	Natural Abundance /%	Larmor Frequency /MHz 9.4 T	16.4 T	21.1 T	Quadrupole Moment / mb
^{1}H	1/2	99.99	400.1	700.1	900.1	
^{13}C	1/2	1.07	100.6	176.0	226.3	
^{19}F	1/2	100	376.5	658.8	846.9	
^{27}Al	5/2	100	104.3	182.4	234.5	146.6
^{29}Si	1/2	4.70	79.5	139.1	178.8	
^{43}Ca	7/2	0.14	26.9	47.1	60.6	-49.0

2.2 Infrared Spectroscopy

In the mid-infrared region of the electromagnetic spectrum, molecular vibrations (*e.g.*, stretches and bends) occur in the wavelength range of 0.00025 to 0.0025 cm. For simplicity, the mid-IR region can be defined in terms of wavenumber (cm^{-1}) from 4000-400 cm^{-1}. By exciting molecular motions in a molecule and analyzing the IR light which has been transmitted through the sample, the functional groups present within the sample can be distinguished and can therefore be a useful tool to identify structural characteristics of unknown samples. In this work, a Nujol mull was created by grinding polymeric powder with a mortar and pestle with Nujol mineral oil. One drop of the sample mixture was placed at the centre of NaCl salt disc and another NaCl disc was used to sandwich the sample mull and create a thin layer suitable for transmission analysis. Using this method, spectra were acquired from 4000-600 cm^{-1} of Nujol, PVDF/Nujol, and dehydrofluorinated PVDF/Nujol (as shown and discussed in Chapter 5). Experimental conditions used in this work are described in further detail in Chapter 5, Section 5.3.2.

2.3 Ultraviolet-Visible Spectroscopy

The ultraviolet-visible (UV-Vis) spectroscopic technique examines electronic transitions within a material. The ultraviolet region of the electromagnetic spectrum lies between 40-390 nm while the visible region is between 390-760 nm. UV-Vis radiation can excite a valence electron in a molecule from the highest occupied molecular orbital (HOMO) to the lowest unoccupied molecular orbital (LUMO). These energy level transitions become particularly effective in conjugated systems (alternating single and double bonds), where increased conjugation and delocalized electrons cause the wavelength absorbance maximum to shift to longer wavelength. Samples which exhibit colour absorb their complimentary colour in the visible region of the electromagnetic spectrum. The UV-Vis technique was employed (experimental conditions described in Chapter 5, Section 5.3.4) in this work to characterize a product of the chemical reaction between PVDF powder and aqueous NaOH.

2.4 Scanning Electron Microscopy/Energy Dispersive Spectroscopy

The scanning electron microscope (SEM) uses a focused beam of electrons to produce high resolution images of a sample surface. The electron beam interacts with the atoms in the sample causing inner shell electrons to be ejected, which are called secondary electrons. A higher energy outer shell electron emits an X-ray, as it relaxes to the core level, which is characteristic of the energy difference between the two shells

and thus of a particular element. The secondary electrons produced from the interaction of the electron beam with the sample, are collected by the electron detector and imaged with a cathode ray tube. A SEM can typically examine sample surfaces at magnifications between $30\times$ and $500,000\times$ with a resolution on the nanometre scale. Figure 2.3 shows a schematic diagram of a SEM electron column that is composed of an electron gun, electromagnetic lenses, electron deflection system (scan coils) and detectors (electron and X-ray). A common electron gun for SEM is the tungsten-hair pin electron gun. The electron gun consists of a cathodic tungsten-hair pin wire filament that generates electrons, which are accelerated through the anode aperture. The voltage difference between the cathode and anode is called the accelerating voltage. The accelerating voltage, typically between 0.1-30 kV, determines the energy and wavelength of the electrons that travel down the electron column. Once the electrons exit the anode aperture, they are focused to achieve a small spot size (less than 10 nm) by the electromagnetic lenses which are controlled by varying their current. The focused beam of electrons then enters the deflection system in which the scanning coils deflect the beam such that it moves across the sample in a controlled raster pattern. Resulting electrons and X-rays, from the beam-specimen interactions, can be detected to create an electron image or an elemental map of the sample surface, respectively.

The SEM imaging technique is commonly coupled with an energy dispersive spectroscopy (EDS) system creating an SEM/EDS technique in which elementally characteristic X-rays emitted by a sample can be collected, sorted by energy, and analyzed

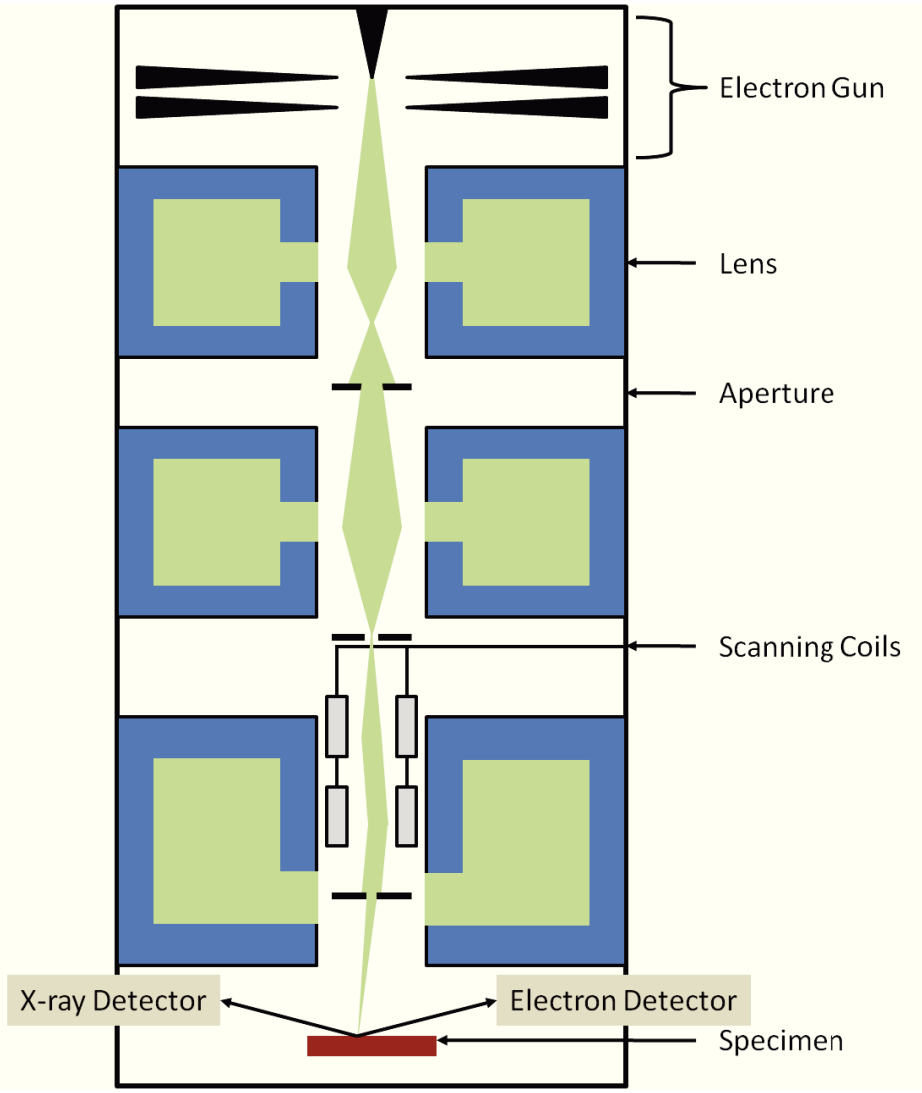

Figure 2.3: Schematic diagram of the electron column in a scanning electron microscope. Styled after Goldstein *et al.* [41].

to produce an elemental map as a function of position of a sample area. Using the SEM/EDS technique, searching a selected surface area for the presence of all elements in the periodic table only takes minutes. Mapping produces a grey scale map in which the pixel value corresponds to the number of X-rays which enter the detector within particular energy range, which gives an idea of the elemental distribution in the sample area. Figure 2.4 shows an example of an electron image and its corresponding elemental map. EDS can analyze X-rays in the 0.7-20 kV range; however, it cannot analyze light elements (atomic numbers less than 5). The spatial resolution in a SEM/EDS map is typically between 1-5 μm [42, 43]. he experimental conditions used in this work are described in further detail in Chapter 6, Section 6.3.2.

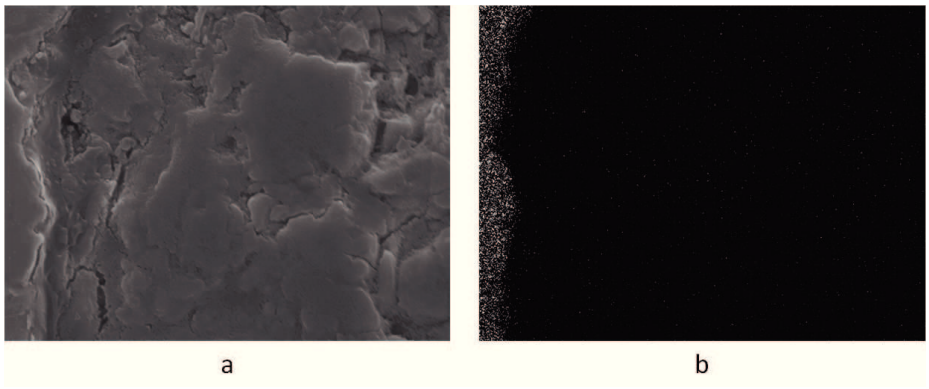

Figure 2.4: SEM/EDS comparison of the steel fibre/white cement interface in an (a) electron image and (b) a Fe elemental map.

2.4.1 Studying the Fibre/White Cement Interfacial Transition Zone via SEM/EDS

To enhance the spatial resolution in SEM/EDS experiments, it is important to consider the interaction volume between the electron beam and the specimen as well

as the spot size of the focused electron beam.

Figure 2.5 shows the relationship between the accelerating voltage, as well as the average atomic number of the sample, with the interaction volume between the electron beam and the specimen. Increasing the accelerating voltage, in theory, reduces the wavelength of the electron beam which allows for a smaller spot size to be achieved; however, higher voltages also increase the interaction volume. Biological and polymeric samples are typically examined with low accelerating voltages between 5-15 kV. The majority of samples in this work are polymeric fibre/cement composites, thus an accelerating voltage appropriate for polymeric materials was chosen within this range (12 kV). The interaction volume is also affected by the composition of the sample. Samples with low average atomic number allow for a larger interaction volume while samples composed of material of high average atomic number produce comparatively smaller interaction volumes. Considering a cementitious matrix with main elemental components of Ca, Al, Si, O, and Fe, the average atomic number would be 16. Using a low accelerating voltage (12 kV) and having samples with an estimated average atomic number of 16, the interaction volume between the specimen and electron beam will be between cases a and b in Figure 2.5.

Figure 2.6 demonstrates the effect of spot size on resolution. If a small condenser lens is chosen, a large spot size is produced reducing resolution. By choosing a larger condenser lens to focus the electron beam, a small spot size is achieved resulting in comparatively better resolution. In this work a condenser lens setting of 5 was chosen to ensure a small spot size was achieved.

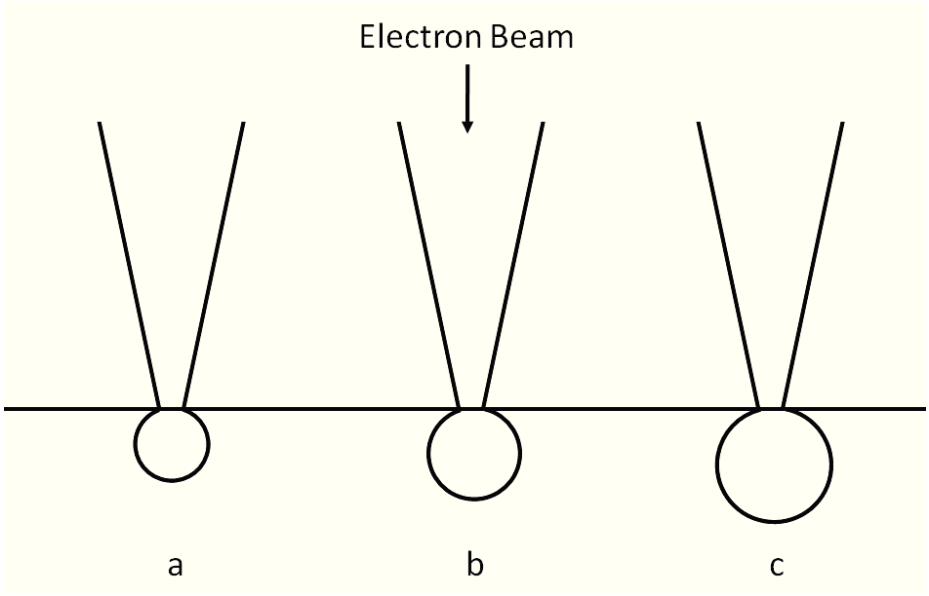

Figure 2.5: Effect of accelerating voltage and average atomic number on the interaction volume in an SEM/EDS experiment. (a) low accelerating voltage, high atomic number, (b) medium accelerating voltage, atomic number, and (c) high accelerating voltage, low atomic number.

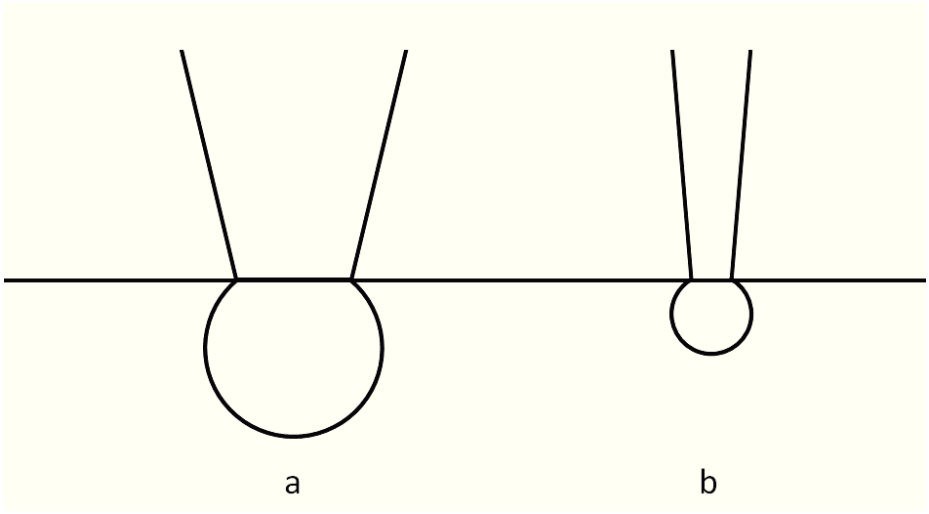

Figure 2.6: Effect of spot size on interaction volume and resolution. (a) small condenser lens creates a large spot size, decreasing resolution and (b) large condenser lens creates small spot size, increasing resolution.

Considering Bentur's model of the steel fibre/concrete interface (introduced in Chapter 1), to successfully study the composition of the interfacial transition zone surrounding the steel and polymeric fibres using the SEM/EDS method, the samples must be viewed under high magnification, such that the fibre edge and approximately 20-250 μm of the surrounding cementitious matrix can be viewed simultaneously, and a micron sized resolution can be achieved to resolve possible layers of $Ca(OH)_2$ as suggested by Bentur and co-workers [26]. Using the SEM/EDS technique, and satisfying the above mentioned conditions, the interfacial transition zone surrounding steel, HDPE/PP, PVA, PVDF, PEI, and Nylon 6.6 fibres was studied by elemental mapping. The results of this study are discussed in Chapter 6.

Chapter 3

Poly(ethylene-vinyl acetate) (EVA) Powder/White Cement NMR Study

3.1 Background

The binding component in concrete is a cementitious matrix, composed of oxides of calcium, silicon, aluminum, and iron, that undergoes a series of complex chemical reactions upon the addition of water to form a hardened stone-like material [14, 16]. The versatile nature of cementitious mortars and concrete composites can be, in part, attributed to the use of admixtures. Admixture is defined as a material that is added to cement immediately before or during the mixing stage (other than water, aggregate or hydraulic cement) [15]. There are numerous classifications of admixtures; for example, accelerating, retarding, and air-entraining, which act to modify the properties of the cement and ultimately the final concrete composite.

Poly(ethylene-vinyl acetate) (EVA) is a specialty admixture that, due to its cost and high required quantities (10% by weight of cement), is most frequently used in latex-modified mortars rather than concrete [16]. Latex-modified mortars are typically used in adhesive, repair, flooring and paving applications [44]. Despite the wide

use of EVA admixture to improve mortar properties such as impermeability, fracture toughness and bond strength, the nature of the interactions between the cement matrix and EVA are not well understood and therefore have been subject of recent interest [45–48].

Silva *et al.* [45] used infrared spectroscopic and thermogravimetric analysis to study EVA hydrolysis in cementitious matrices. This study reported that EVA hydrolysis was not complete but formed terpolymer and calcium acetate products. From the thermogravimetric study, it was concluded that EVA greatly reduces the $Ca(OH)_2$ formation in the cement hydration process. This study put forth evidence for chemical interactions between the OH groups of the EVA hydrolysis product and Ca^{2+} in cementitious matrices. Rottstegge and co-workers [46] used ^{13}C cross-polarization (CP)/magic angle spinning (MAS) solid state NMR spectroscopy to study the hydrolysis of EVA latex in mortar. The differences (spectral broadening of the CHO and CH_2 resonances) in the ^{13}C CP/MAS NMR spectra of the control sample (EVA/mortar unhydrated) and the EVA in hydrated mortar were attributed to partial EVA hydrolysis. In this study, however, no ^{13}C CP/MAS signal attributable to the formation of $Ca(CH_3COO)_2$ was observed. Betioli *et al.* [47] used differential thermogravimetric methods to study the chemical interaction between EVA and Portland cement in the early stages of hydration (15 minutes to 24 hours). They observed bands which were attributed to the decomposition of $Ca(CH_3COO)_2$ and ultimately concluded that EVA reduces the formation of $Ca(OH)_2$ as a result of EVA hydrolysis and $Ca(CH_3COO)_2$ formation. Mansur *et al.* [48] studied the hydrolysis of EVA in a cementitious matrix

using FT-IR spectroscopy and presented an "extension of hydrolysis" parameter that was determined from the ratio of areas under the carboxylate to the C=O or ether peak. It was concluded that hydrolysis of EVA admixture in mortar is of utmost importance to the formation of adhesion between mortar and ceramic tile (hydrogen bonding between OH from terpolymer hydrolysis product and silanol groups on the surface of the ceramic tile).

The objective of the present study was to monitor the hydrolysis of EVA admixture in a hydrating white cement matrix. EVA re-dispersible latex was mixed into white cement paste and hydrated for pre-determined times over a 3 month period. Using single pulse excitation (SPE) ^{13}C NMR spectroscopy, resonances indicative of EVA carbonyl (168 ppm) and the calcium acetate hydrolysis product carbonyl (181 ppm) were monitored and a kinetic model was determined. SPE ^{43}Ca NMR was used to determine if changes in cementitious calcium sites, specifically $Ca(OH)_2$, occur as a result of the presence and hydrolysis of EVA. SPE and CP ^{29}Si NMR experiments were used to study any structural changes or chemical interactions involving silicon, which occur as a result of the addition of EVA latex to white cement paste. These studies give insight into the stability of EVA admixture as well as possible structural changes in the hardened cementitious matrix with respect to EVA hydrolysis over time.

3.1.1 Sample Preparation

Cement pastes were prepared using white Portland cement (Federal White Cement), distilled water, and EVA water re-dispersible latex (DLP 2000, Dow Chemical Company). To introduce a significant amount of interface at which the hydrolysis reactions can take place, the EVA latex (1 μm particulate size) was added to white cement paste at 20% cement weight. A water to cement ratio of 0.40 was chosen to ensure optimum hydration and a densely packed hardened composite [14].

EVA latex was dry-mixed into cement followed by the addition of water. The cement paste was mixed with a light duty mixer (Arrow 6000) until a smooth consistency was achieved (approximately 2 minutes). Specimens were cast in silicone moulds and sealed in a plastic container for 1 day at which time they were removed from the moulds and sealed in a plastic container for the remainder of their hydration period. At pre-determined hydration times, samples were frozen in liquid nitrogen and lyophylized to remove all free water present, thus effectively stopping the hydration process [47]. In this manner, samples with the following hydration times were prepared: 0.25, 0.50, 1, 2, 3, 4, 5, 6, and 12 hours and 1, 2, 4, 7, 12, 15, 22, 28, 32, 48, 56, and 84 days. All samples were stored in a N_2 atmosphere until NMR analysis could be conducted.

During preliminary stages of this work, white cement control and EVA/white cement samples were prepared with D_2O instead of H_2O to reduce the ^1H content in the cementitious matrix to facilitate the isolation of the EVA/white cement interface

by creating a heteronuclear pair for study in which one nucleus is associated with the polymer and the other the cement. White cement paste with a D_2O to cement ratio of 0.5 was used to cast white cement control and EVA/white cement (containing 10% EVA by cement weight) specimens. Samples were hydrated in sealed plastic containers for one week and were then ground to a powder for NMR analysis.

3.1.2 Experimental

All ^{13}C experiments were conducted on a 400 MHz Bruker Avance NMR spectrometer, operating at a magnetic field of 9.4 T (Larmor frequencies of 400.240 and 100.655 MHz for ^{1}H and ^{13}C, respectively) using a 4 mm probe. Samples were spun up to 8 kHz to characterize spinning sidebands and isotropic frequencies. Spectra were referenced to the carbonyl resonance of glycine at 176.06 ppm as a secondary standard. SPE ^{13}C NMR spectra were acquired after a 5 μs 90 $^\circ$ pulse with 5120 scans using a 5 s recycle delay with proton decoupling. No attempt was made to determine ^{13}C relaxation times. Data were background corrected by subtracting the signal from an empty rotor. Data were processed with linebroadening of 100 Hz. ^{13}C CP/MAS NMR spectra were acquired with a 4 μs 90 $^\circ$ pulse on ^{1}H, 2048 scans with a recycle delay of 3 s, a contact time of 2.6 ms with TPPM proton decoupling. Data were processed with linebroadening of 100 Hz.

SPE ^{43}Ca NMR spectra were obtained with a 900 MHz Bruker Avance II NMR spectrometer, operating at a magnetic field of 21.1 T (Larmor frequency of 60.576 MHz)

using a 7 mm single channel probe after a 1 μs 40 $^\circ$ pulse. Each spectrum was acquired with 81,920 scans with a recycle delay of 2 s at a spinning frequency of 5 kHz. Spectra were referenced to 2.0 M $CaCl_2$ at -14 ppm consistent with Bryce *et al.* [49]. Data were processed with linebroadening of 200 Hz.

All ^{29}Si experiments were conducted on a 700 MHz Bruker Avance NMR spectrometer, operating at a magnetic field strength of 16.4 T (Larmor frequecies of 139.114 and 700.289 MHz for ^{29}Si and ^{1}H, respectively) using a 4 mm probe. Samples were spun at 10 kHz and the chemical shift scale was referenced to kaolin at -91.34 ppm. SPE ^{29}Si NMR spectra were acquired after a 7 μs 90 $^\circ$ pulse with a recycle delay of 35 s and a total of 6144 averaged scans. ^{29}Si CP/MAS NMR spectra were acquired following a 4 μs 90 $^\circ$ pulse on ^{1}H, 2048 scans with a recycle delay of 10 s, and a contact time of 5 ms. Data were processed with 50 and 100 Hz linebroadening for SPE and CP/MAS NMR experimental data, respectively.

3.2 Results and Discussion

Consistent with the literature [50], the following mechanism and overall reaction for the hydrolysis of EVA in a cementitious matrix (Figure 3.1) is proposed.

EVA hydrolysis proceeds via a nucleophilic acyl substitution pathway that is described by second order kinetics [51]. As shown in Figure 3.1a, the OH^- nucleophile attacks the ester functional group promoting acyl-oxygen cleavage that results in the formation of an alcohol and a carboxylic acid. More specifically (see Figure 3.1b), in an alkaline environment, such as that of cement paste (pH 13), the vinyl acetate

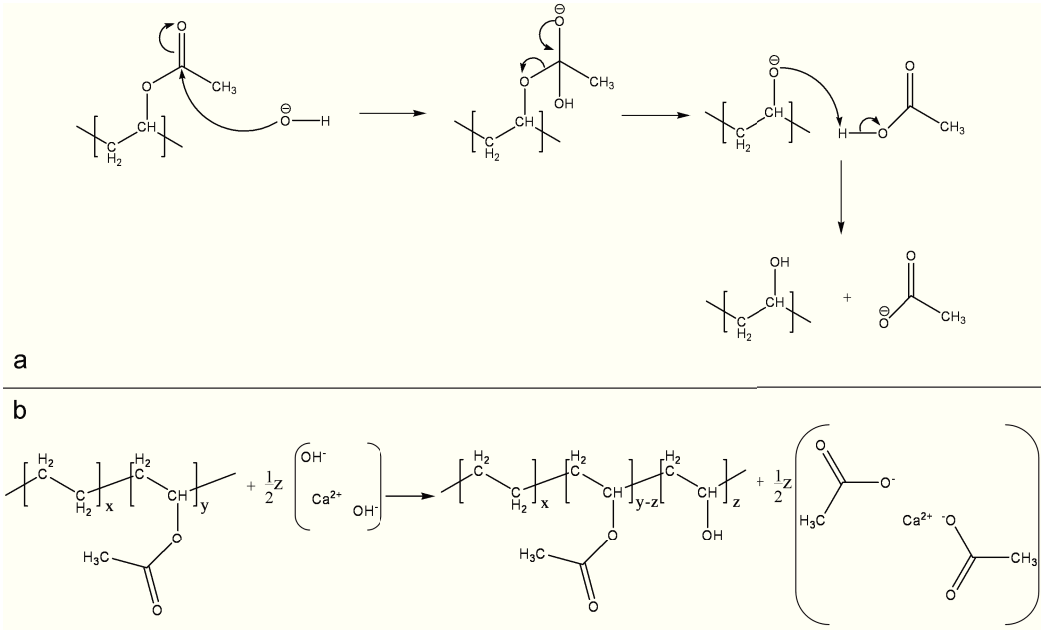

Figure 3.1: Proposed mechanism (a) and overall reaction (b) for saponification of EVA in white cement during hydration.

unit of EVA undergoes partial hydrolysis producing a terpolymer, poly(ethylene-vinyl acetate-vinyl alcohol), and a calcium acetate salt, $Ca(CH_3COO)_2$ [45–48]. The consumption of Ca^{2+} through $Ca(CH_3COO)_2$ formation decreases the formation of $Ca(OH)_2$ [45]. Betioli *et al.* [47], using thermogravimetric methods, observed the decomposition of the $Ca(CH_3COO)_2$ species in the early stages of hydration (within 24 hours). Using ^{13}C CP/MAS solid state NMR methods, Rottstegge *et al.* [46] attributed line broadening in CH_2 and CHO resonances to partial EVA hydrolysis; however, no $Ca(CH_3COO)_2$ resonance was observed.

3.2.1 NMR Studies

Cements contain many NMR active nuclei. To study the chemical interactions between EVA and white cement, ^{13}C and ^{43}Ca NMR spectroscopies were applied.

While ^{13}C and ^{29}Si are comparatively easy nuclei to study, the ^{43}Ca nucleus presents a challenge due to its low natural abundance (0.135 %), quadrupolar magnetic spin (I=7/2), and low Larmor frequency (26.929 MHz at 9.4 T). For these reasons, the occurrence of literature in this area has been moderate [40,52–60] until very high field NMR spectrometers (Larmor frequency of 60.579 MHz at 21.1 T) became available making this nucleus more attractive for enriched [61] and natural abundance [49,62–67] studies.

3.2.1.1 SPE ^{13}C NMR

The SPE ^{13}C NMR spectrum of EVA (Figure 3.2) agrees with the literature [46] and contains characteristic resonances at 21 ppm (CH_3), 34 ppm (CH_2), 68 ppm (CHO), and 170 ppm (C=O). If EVA undergoes hydrolysis and $Ca(CH_3COO)_2$ is formed, new resonances between 175-190 ppm, specifically 181 ppm ($Ca(CH_3COO)_2 \cdot \frac{1}{2}H_2O$) and 186 ppm ($Ca(CH_3COO)_2 \cdot H_2O$) would be observed [68, 69]. SPE ^{13}C NMR spectroscopy was used to monitor the saponification of EVA and the formation of $Ca(CH_3COO)_2$ over a period of 3 months. Figure 3.3 shows the SPE ^{13}C NMR spectra of EVA/white cement pastes at 1, 2, 4, 7, 12, 15, 22, 28, 32, 48, 56, and 84 days of hydration. At a hydration time of 1 day (and all those tested prior to 1 day), there is no apparent resonance from $Ca(CH_3COO)_2$; however, between hydration times of 1 and 84 days the $Ca(CH_3COO)_2$ resonance (181 ppm) becomes evident and increases over time. There is no significant contribution to the ^{13}C spectra from cementitious carbonyl species (see Figure 3.4a), between 190-160 ppm, therefore, the resonance at

181 ppm (see Figure 3.4b) was confidently assignmend as the $Ca(CH_3COO)_2$ carbonyl resonance. Similar to the results of Rottstegge *et al.* [46], spectral broadening of CHO and CH_2 resonances is observed which further reflects the effect of EVA hydrolysis.

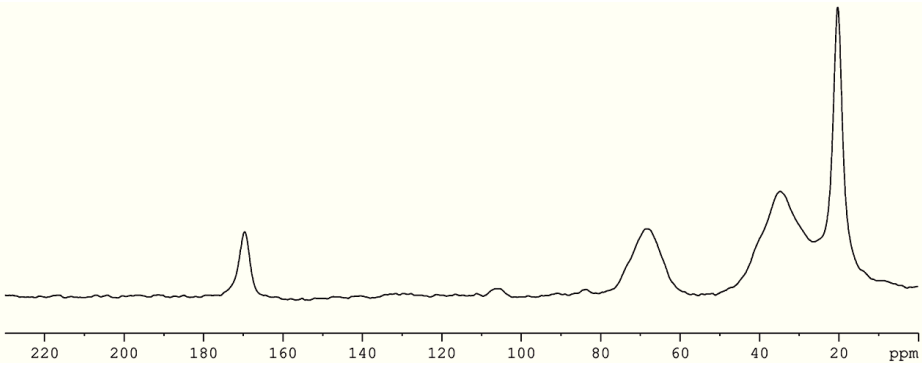

Figure 3.2: SPE ^{13}C NMR spectrum of EVA.

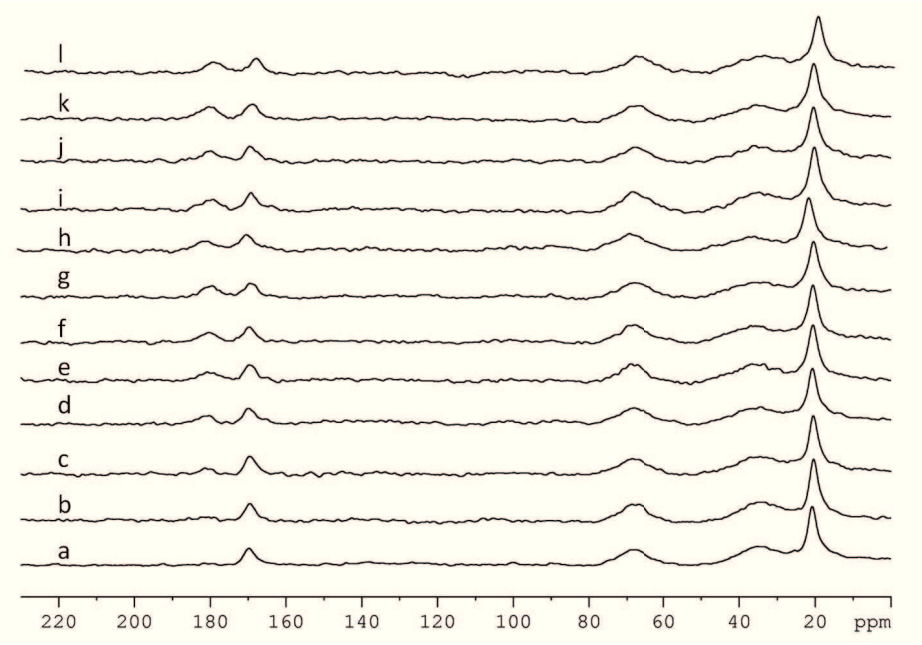

Figure 3.3: SPE ^{13}C NMR spectra of EVA/white cement at various stages of hydration. (a) 1 day, (b) 2 days, (c) 4 days, (d) 7 days, (e) 12 days, (f) 15 days, (g) 22 days, (h) 28 days, (i) 32 days, (j) 48 days, (k) 56 day, (l) 84 days.

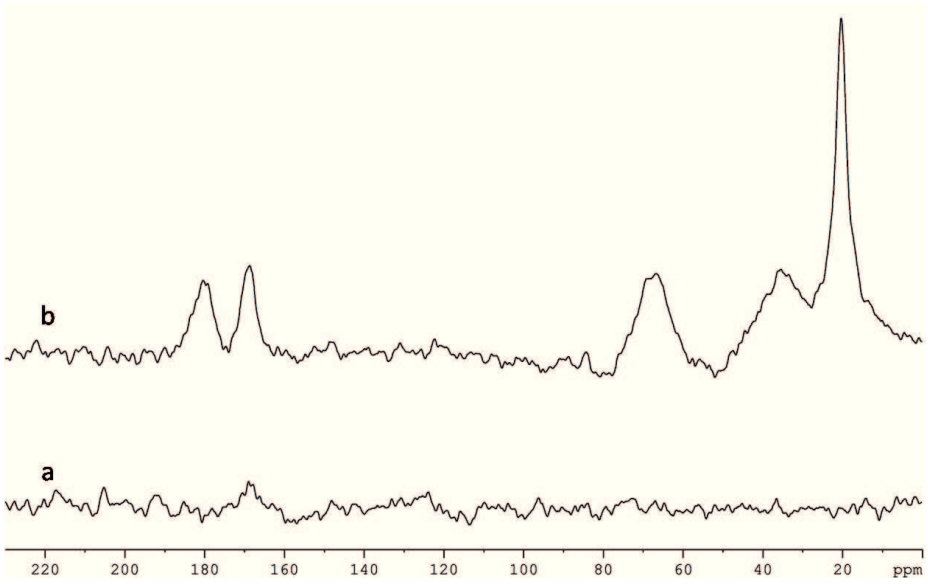

Figure 3.4: SPE ^{13}C NMR spectra of (a) hydrated white cement and (b) EVA/white cement at 56 days hydration.

3.2.1.2 ^{13}C CP/MAS NMR

For comparison with the Rottstegge study [46], ^{13}C CP/MAS spectra were collected at various hydration times.

Figure 3.5 shows the ^{13}C CP/MAS spectra of EVA/white cement systems at 2, 4, 22, 28, 56, and 84 days of hydration. These spectra clearly show the resonance at 181 ppm that is attributed to the $Ca(CH_3COO)_2$ EVA hydrolysis product. Also, in the CP spectra spectral broadening of the CHO and CH_2, similar to that observed in the Rottstegge study, was observed. For the purposes of this experiment, kinetic data were extracted from the SPE ^{13}C NMR spectra only, as the integrated intensities of the resonances in the ^{13}C CP/MAS spectra are dependent on the magnetization that can be transferred from nearby protons in the cement and in EVA.

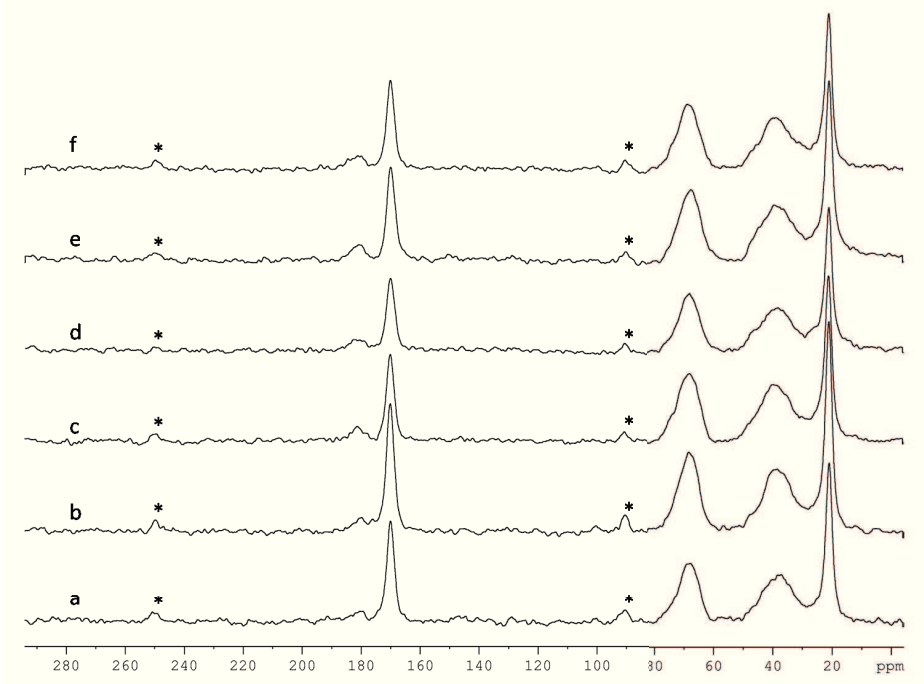

Figure 3.5: ^{13}C CP/MAS NMR spectra of (a) 2, (b) 4, (c) 22, (d) 28, (e) 56, and (f) 84 days hydration (* spinning side bands).

3.2.1.3 SPE ^{43}Ca NMR

The formation of $Ca(CH_3COO)_2$ during the hydrolysis of EVA creates a new calcium environment in the cementitious system and it was desired to detect it with ^{43}Ca NMR spectroscopy. The SPE ^{43}Ca NMR spectra of white cement (7 day hydration), EVA/white cement (1 day hydration), and EVA/white cement (28 day hydration) are shown in Figure 3.6. Given the low signal-to-noise ratio the three spectra are essentially identical. They all show a broad resonance between 55 and -10 ppm. Whether there is additional signal in the EVA-cement samples between 100 ppm and 55 ppm is questionable.

The major component of hydrated cement paste is CSH. Taylor *et al.* [14, 70, 71]

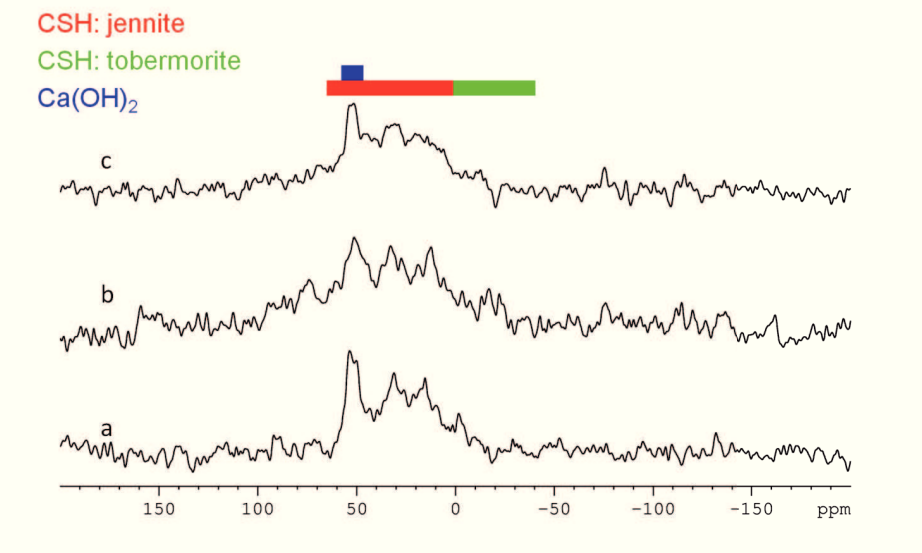

Figure 3.6: SPE ^{43}Ca NMR spectra of (a) white cement (7 day hydration), (b) EVA/white cement (1 day hydration), and (c) EVA/white cement (28 day hydration). The $Ca(OH)_2$ region is pictured in blue (peak maximum of 53 ppm), jennite is pictured in red (broad resonance between 0 and 62 ppm) and tobermorite is pictured in green (resonance at -10 ppm).

postulated that the structure of CSH is like that of tobermorite or jennite (structures introduced in Chapter 1). Both exhibit a layered structure in which a sublayer composed of CaO_2 and CaO−OH linkages, for tobermorite and jennite respectively, is sandwiched between Si_3O_9H chains. The interspace between the silicate chains is composed of $Ca_2 \cdot 8\,H_2O$ (for tobermorite) and $Ca_2 \cdot 6\,H_2O$ (for jennite) [16]. Bowers *et al.* [64] studied the calcium environments in crystalline tobermorite, jennite, and $Ca(OH)_2$ using ^{43}Ca NMR at the same magnetic field strength as this study. They found that the ^{43}Ca NMR spectra for tobermorite give resonances between 0 and −40 ppm with maxima at -10 ppm and for jennite between 5 and −60 ppm with maxima at 24 ppm. In their results, the resonances of tobermorite and jennite do not overlap. They also investigated $Ca(OH)_2$ resonances between 30 to 70 ppm with a

peak maximum at 60 ppm which only partially overlaps with the jennite resonances. The ^{43}Ca NMR spectra of EVA/white cement composites, presented in this work, are essentially a summation of the spectral features of tobermorite, jennite, and $Ca(OH)_2$. Consistent with Bowers *et al.* [64], resonances were assigned as a broad jennite resonance between 0 ppm and 62 ppm with an apparent peak maximum at 31 ppm, the tobermorite resonance at -10 ppm, and the $Ca(OH)_2$ peak maximum at 53 ppm. Bryce *et al.* [49] shows $CaCO_3$ experimental resonances for calcite between 3 to 6 ppm and for vaterite between 0 and -30 ppm centered at 10 ppm (at 21.1 T magnetic field strength). These resonances would overlap in the tobermorite region of the spectrum. Since there are no significant intensity changes in this region, it was concluded that $CaCO_3$ is not significantly contributing to the ^{43}Ca NMR spectra which is consistent with the ^{13}C study. Apparently, based on the ^{43}Ca NMR spectra, the presence of the EVA admixture does not greatly affect the CSH structure or $Ca(OH)_2$ sites in the hydrated cement paste.

Wong *et al.* [65] studied crystalline $Ca(CH_3COO)_2 \cdot H_2O$ using ^{43}Ca NMR at 14.1 T magnetic field strength and observed resonances at -15.9 and 7.8 ppm corresponding to calcium coordinated to eight and seven oxygen atoms, respectively. Due to their narrow lines, they conclude only minor quadrupole contributions. Therefore, lines in similar shift ranges could be expected. There were no new significant signal intensities in the EVA/white cement samples found in this frequency range. Based on cement and latex composition, it was estimated that less than 3 % of calcium in the samples would be in the form of $Ca(CH_3COO)_2$ following cement hydration and EVA

hydrolysis. With such small amounts of $Ca(CH_3COO)_2$ being formed, coupled with the likelihood of the $Ca(CH_3COO)_2$ forming in the cementitious matrix being amorphous in nature and therefore less well defined, it is not surprising that resonances attributable to $Ca(CH_3COO)_2$ in the ^{43}Ca spectra are not observable.

3.2.1.4 ^{29}Si SPE and CP/MAS NMR

As discussed previously, EVA is commonly used in latex-modified mortars to improve bonding between tile and mortar. Mansur *et al.* [48, 50] studied the chemical interactions between silanol modified tile and EVA-modified mortar. It was concluded that the hydroxyl functional groups in hydrolyzed EVA act as a bonding agent between the $Ca \cdot xH_2O$ (where x is 6 for jennite-like CSH and 8 for tobermorite-like CSH) interlayer in CSH and the silanol modified surface of the tile.

To explore the bonding potential between EVA and the hydroxyl groups on the CSH silicate chains, ^{29}Si NMR spectroscopy was employed. Figure 3.7 shows the ^{29}Si SPE NMR spectrum of EVA/white cement after 1 week of hydration with D_2O. Following the assignment by Rottstegge *et al.* [72], ^{29}Si resonances are assigned as Q^0 (−72.7 ppm), Q^1 (−80.3 ppm), Q^2 (−85.7 ppm), and Q^3 (−92.7 ppm), where Q^n indicates the number of SiO_4^{4-} units surrounding a central silicon atom. Figure 3.8 shows the Q^n silicon environments for n=0, 1, 2, and 3. The intense Q^0 resonance in the SPE spectrum indicates that cement hydrolysis is not fully complete for the EVA/white cement system in D_2O after a period of one week. To examine the interactions between polymeric protons and the silicon sites in the EVA/white cement

specimens, the CP/MAS NMR technique was employed. Figure 3.9 shows the ^{29}Si CP/MAS NMR spectra of EVA/white cement specimens using various contact times (0.5, 1.0, 2.0, and 5.0 ms). From these spectra, it was determined that the best signal to noise is achieved with a contact time of 5.0 ms to allow for sufficient magnetization transfer between ^{1}H and ^{29}Si to isolate the interface between the polymeric powder and cement. Using a contact time of 5.0 ms, ^{29}Si CP/MAS NMR spectra of a white cement control and EVA/white cement were acquired following 1 week of D_2O hydration (shown in Figure 3.10).

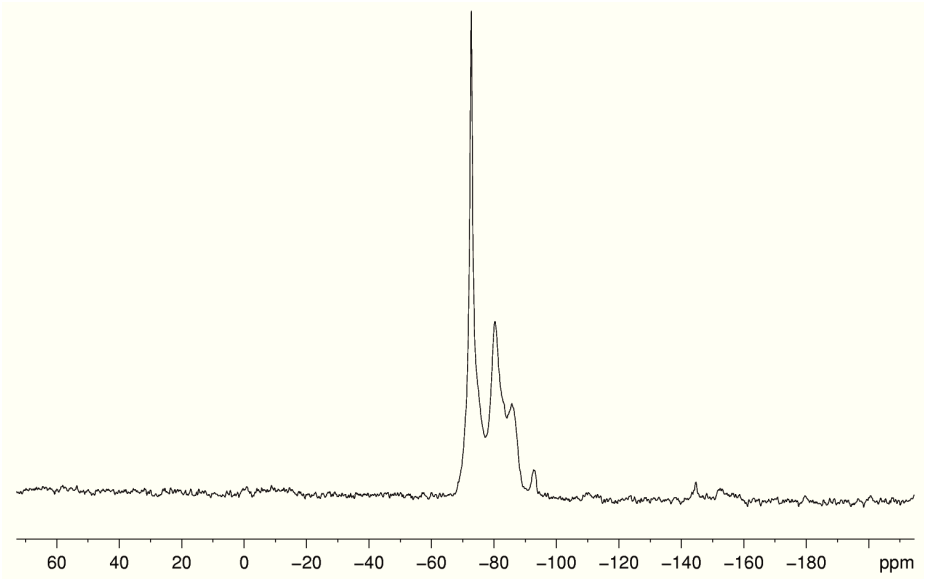

Figure 3.7: ^{29}Si SPE NMR spectrum of EVA/white cement after 1 week of hydration with D_2O.

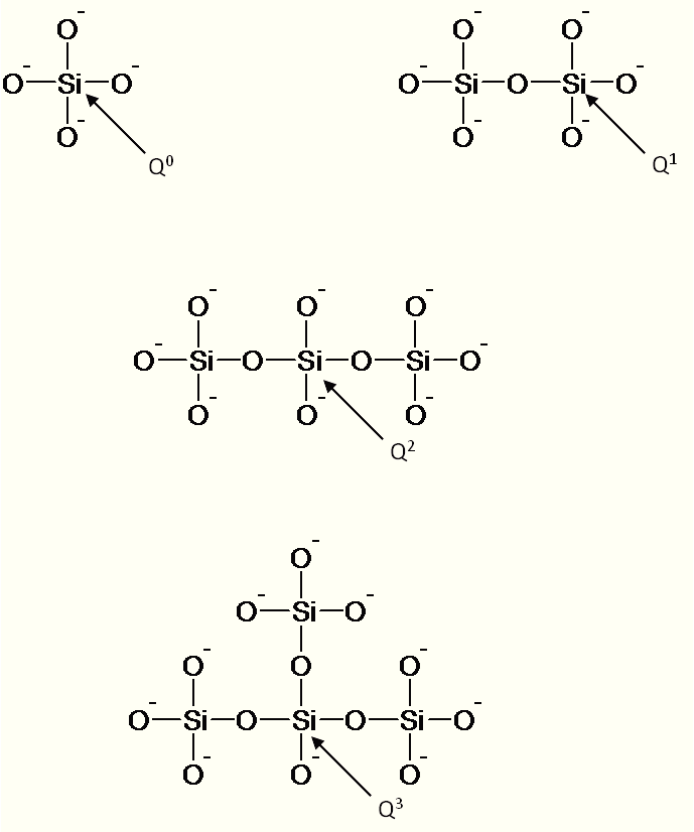

Figure 3.8: Q^n silicon centres for n=0, 1, 2, 3.

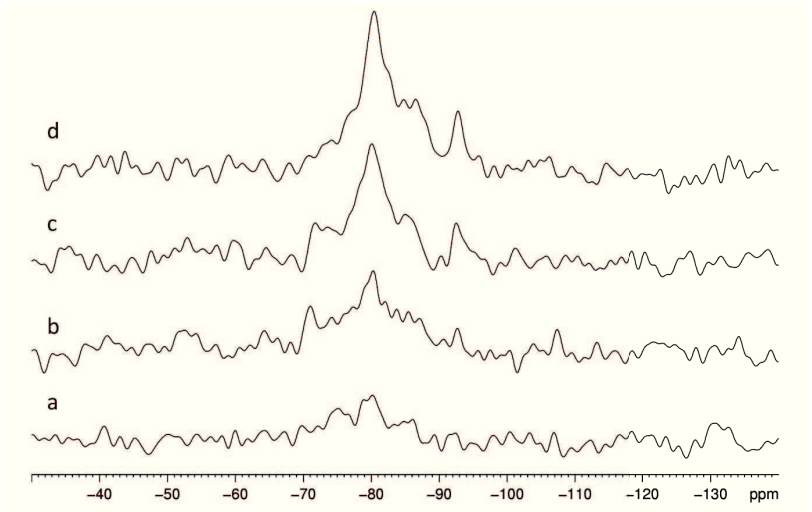

Figure 3.9: ^{29}Si CP/MAS NMR spectra, at various contact times, of EVA/white cement after 1 week of hydration with D_2O. Letters a, b, c, and d indicate contact times of 0.5, 1.0, 2.0, and 5.0 ms, respectively.

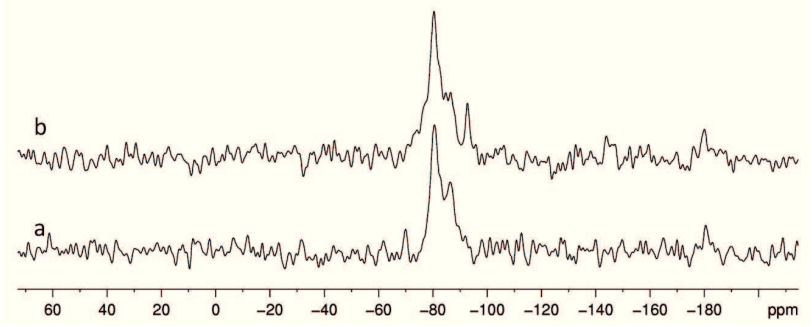

Figure 3.10: ^{29}Si CP/MAS NMR spectra of (a) white cement control and (b) EVA/white cement after 1 week of hydration with D_2O.

In both spectra, resonances of silicon centres, Q^1 and Q^2, can be assigned at approximately −80 ppm and −86 ppm, respectively. In the spectrum for EVA modified cement (Figure 3.10b), a Q^3 resonance was assigned at −92.7 ppm. This Q^3 resonance in the ^{29}Si CP/MAS NMR spectrum indicates that there are more protons surrounding the Q^3 silicon sites in EVA modified white cement in comparison to those sites in the white cement control. These data suggest that there could be hydrogen bonding potential between the silicon sites in the CSH and hydrolyzed EVA. Figure 3.11 depicts a potential hydrogen bonding environment between CSH and hydrolyzed EVA which could contribute to increased chemical bonding.

3.2.2 Reaction Kinetics of EVA Hydrolysis in Cement

Using the CH_3 resonance as an internal standard, the ratios of the integrated intensities for the carbonyl and methyl group peaks for $Ca(CH_3COO)_2$ ($R_{Ca(CH_3COO)_2}$) and EVA carbonyl (R_{EVA}) were plotted against hydration time (Figure 3.12). A 10%

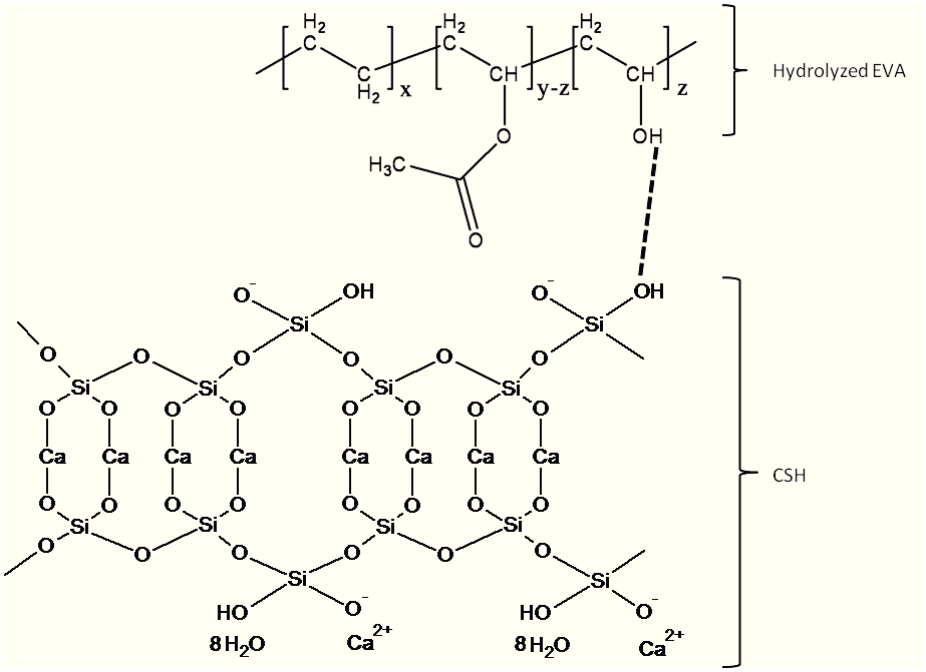

Figure 3.11: Potential hydrogen bonding between hydrolyzed EVA and CSH (tobermorite-like CSH depicted).

error from acquisition and spectral processing was taken into account and propagated into the $R_{\mathrm{Ca(CH_3COO)_2}}$ and R_{EVA} and kinetics calculations (error bars shown in Figure 3.12). These values are not the absolute ratios, due to unknown relaxation times; it is assumed that the relaxation times, mostly dominated by methyl group rotation, do not change significantly over the times evaluated here (1-84 days). In Figures 3.12 (specifically R_{EVA} data set) and 3.13, outliers were removed at 2 and 4 days of hydration with 99% confidence.

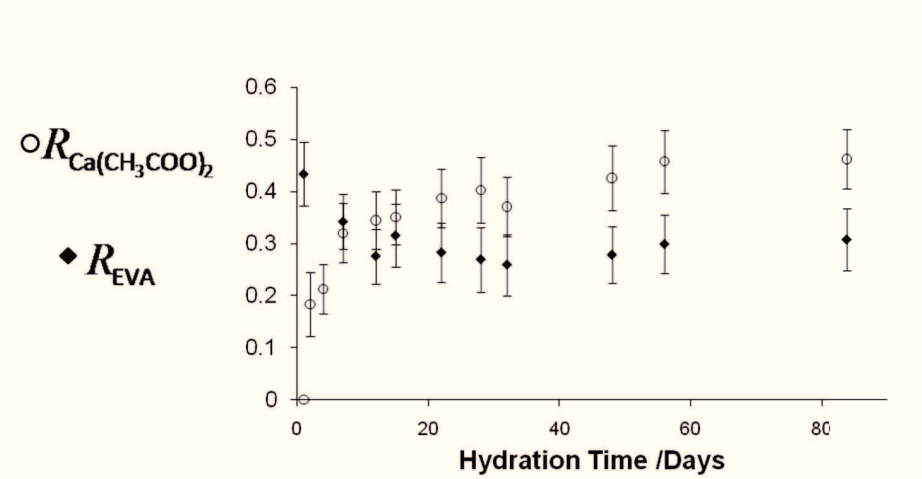

Figure 3.12: Consumption of vinyl acetate and formation of $Ca(CH_3COO)_2$ over time.

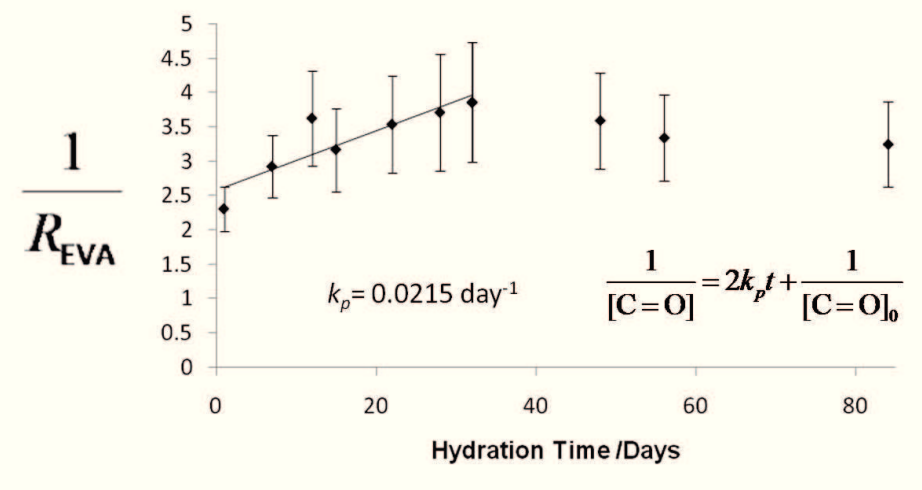

Figure 3.13: Pseudo-second order kinetics plot of EVA hydrolysis.

Sakurada [73] describes the hydrolysis of poly(vinyl acetate) as an autocatalytic reaction in which hydroxyl pendant groups formed during hydrolysis catalyze the reaction of neighbouring acetate groups. The hydrolysis of EVA, in solution, is shown to proceed via a second order kinetics reaction [74,75]. To explain the kinetics of EVA hydrolysis in cement one must first consider the cement hydration process. During

hydration, tricalcium silicate ($(CaO)_3 \cdot SiO_2$ or C_3S) reacts with water to produce CSH gel ($(CaO)_x \cdot SiO_2 \cdot yH_2O$) and $Ca(OH)_2$ by the following reaction (Equation 3.1: not necessarily in this stoichiometry) [16]

$$(CaO)_3{\cdot}SiO_2 + 2\,H_2O \longrightarrow (CaO)_2{\cdot}SiO_2{\cdot}H_2O + Ca(OH)_2. \tag{3.1}$$

C_3S hydration occurs in four stages: (a) pre-induction; (b) induction; (c) acceleration; and (d) deceleration (see Chapter 1, Figure 1.1). The pre-induction stage lasts from minutes to hours and is characterized by a short lived hydrolysis of C_3S as alkali earth oxides rapidly dissolve in water. Between 6-12 hours, the hydration of C_3S slows and essentially becomes dormant (induction). Following this period, at approximately 1 day of hydration, the reaction accelerates and C_3S hydrates rapidly. Eventually, as the cement hardens the hydration reactions become diffusion controlled and continue for years [16, 76].

For the hydrolysis of EVA to begin, C_3S hydration must provide $Ca(OH)_2$. Evidence of EVA hydration was observed in the SPE ^{13}C NMR spectra as early as 2 days of hydration which coincides with the beginning of the C_3S acceleration period. EVA hydrolysis continues and produces increasing amounts of $Ca(CH_3COO)_2$ until 32 days of hydration. Focusing on the reaction between the vinyl acetate unit and $Ca(OH)_2$ (see Figure 3.14), the rate law can be written as (Equation 3.2):

$$\frac{d[\text{C=O}]}{dt} = -2k[\text{C=O}]^2[Ca(OH)_2] \tag{3.2}$$

where k is the rate constant. Assuming that the $Ca(OH)_2$ is in excess, the rate constant, k, and $[Ca(OH)_2]$ can be combined to from a pseudo rate constant, k_p, and thus a simplified pseudo second order rate law (Equation 3.3).

$$\frac{d[\text{C=O}]}{dt} = -2k_p[\text{C=O}]^2 \tag{3.3}$$

It follows that the hydrolysis of EVA follows a pseudo-second order kinetics model and as such the R_{EVA} data will also follow this model (Equation 3.4 and Figure 3.13)

$$\frac{1}{R_{\text{EVA}}} = \frac{1}{R_{\text{EVA}_0}} + 2k_p t. \tag{3.4}$$

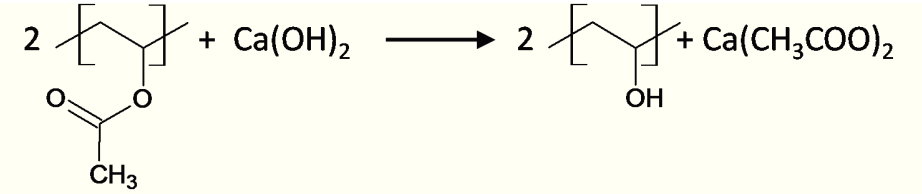

Figure 3.14: Chemical reaction equation for vinyl acetate hydrolysis.

The data fit the pseudo-second order kinetics model up to 32 days of hydration with an R^2= 0.7759 and k_p= 0.0215 day^{-1}. Beyond 32 days, the ratio of carbonyl to methyl groups remains roughly constant within NMR precision. It is speculated that, as in this time frame the cement hydration reactions are well within their deceleration period and are diffusion controlled, the EVA hydrolysis kinetics also adopts a diffusion controlled kinetics model or in any case slower and more complex kinetics than the initial pseudo-second order behaviour.

3.3 Conclusion

SPE ^{13}C and ^{43}Ca NMR spectroscopy was used to successfully monitor the hydrolysis of EVA in white cement over a 3 month period and ^{29}Si NMR was used to study the effect of EVA latex on cementitious silicon sites in EVA/white cement specimens (hydrated with D_2O for 1 week). SPE ^{13}C and CP/MAS NMR spectra clearly showed the resonance associated with the expected $Ca(CH_3COO)_2$ EVA hydrolysis product. From the SPE ^{13}C NMR spectra, the reaction kinetics of EVA hydrolysis were modelled and found to be pseudo-second order between 1-32 days of hydration with a pseudo-rate constant, k_p, of 0.0215 day^{-1}. Following 32 days of hydration, it was found that EVA hydrolysis deviates from the pseudo-second order kinetics model and it is speculated that it adopts a diffusion model. SPE ^{43}Ca NMR spectra did not show a resonance corresponding to $Ca(CH_3COO)_2$ as anticipated; however, the results indicate that the presence of the EVA admixture does not greatly affect the structure of the calcium sites in the cementitious matrix. The ^{29}Si NMR spectra indicate that there are more protons near the Q^3 silicon sites, as demonstrated with the CP NMR technique, when EVA additive is present in the cementitious matrix which suggests a potential hydrogen bonding environment between the silanol groups in CSH and the hydroxyl group of hydrolyzed EVA. This result is consistent with work in the literature [48, 50], which states that EVA bonds via hydrogen bonding with silanol modified tiles. Therefore, EVA, in its hydrolyzed form, can act as a binding agent between cementitious matrices and silanol modified tile at the interface.

Chapter 4

Poly(ether imide)/White Cement NMR Study

4.1 Background

Poly(ether imide) (PEI) is a high performance thermoplastic which is sold under the trade name Ultem®. As a result of its high melting temperature (350-400 °C), Young's modulus (3.59 GPa), and tensile strength (110 MPa) [77], PEI resin was chosen as a candidate for fibre production for concrete reinforcement applications [13]. PEI has been shown to be suitable for fibre production [78] and, until 2009, this material had not been pursued as a possible concrete reinforcement [13]. The chemical structure of PEI is shown in Figure 4.1.

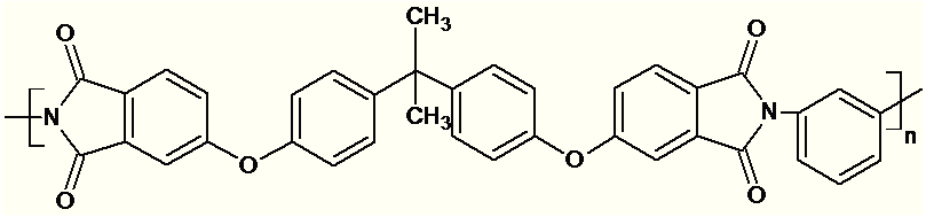

Figure 4.1: Poly(ether imide) chemical structure.

The aromatic rings present in PEI's structure provide rigidity to the backbone while the ether linkages impart some flexibility in the chain. The bond between polymeric fibres and concrete is of utmost importance to a fibre's ability to toughen a

concrete composite. The ether and imide functionalities give PEI a hydrophilic character and it is postulated that it will bond better with concrete via hydrogen bonding mechanisms than commercial HDPE/PP fibres. PEI is known to be highly resistant to acidic environments, hydrolysis, and is categorized as a limited service material in alkaline environments [79]; therefore, it is possible that the imide group could undergo hydrolysis in the basic cementitious environment which could potentially damage the fibre surface. To test PEI's stability in concrete, Trottier [13] used optical microscopy to study fibre and tensile coupon surfaces after exposure to basic conditions. PEI fibres were cast in cement and hydrated for 3 weeks, while tensile coupons were immersed in aqueous NaOH solution (pH 11) for 7 days prior to analysis. No visible signs of degradation were observed on fibre or tensile coupon surfaces. Trottier [13] observed a mass increase in tensile coupons of 0.43 $\pm$ 0.05% and attributed this increase to water absorption.

To explore further PEI's suitability as a concrete reinforcement material, SPE and CP/MAS ^{13}C NMR spectroscopy were used to investigate possible structural changes in samples of PEI, hydrolyzed PEI, and PEI/white cement (hydrated for 7 and 28 days). It is speculated that imide hydrolysis, if minimal, could contribute to a stronger chemical bond between the PEI surface and white cement through increased hydrogen bonding opportunities from the carboxylic acid and amine functional groups which would enable this material to contribute to the toughening of a concrete composite.

4.2 Sample Preparation

Ultem® 1000 PEI resin (SABIC Plastics) was cryogenically milled to a particulate size of 700 μm using a Spex SamplePrep 6770 Freezer Mill. White cement with 20% PEI by cement weight, with a $w/c = 0.4$ (to ensure complete hydration), was cast in silicone moulds and hydrated for periods of 1 week and 28 days in a sealed plastic container. At the pre-determined hydration times, the samples were freeze dried to remove all free water to halt further hydration processes. Samples were stored and ground for NMR analysis in a N_2 atmosphere.

A sample of hydrolyzed PEI was prepared by reacting 0.5 g of PEI resin (700 μm particulate size) with 30 mL of 0.5 M NaOH solution at 60 °C for 1.5 hours, consistent with Kim *et al.* [80]. NaOH solution was prepared using deionized water. The hydrolyzed PEI product was recovered by filtration, washed with deionized water, and dried over dessicant for 2 days prior to analysis.

4.3 Experimental

^{13}C experiments were conducted on a 700 MHz Bruker Avance NMR spectrometer operating at a magnetic field of 16.4 T using a 4 mm double resonance probe at a spinning speed of 13 kHz. SPE ^{13}C NMR spectra were acquired following a 4.6 μs 90 ° pulse and a recycle delay of 5 s. For polymeric samples, 1024 scans were acquired while 5120 scans were acquired for polymer/cement samples. ^{13}C CP/MAS NMR spectra were acquired using a 4 μs 90 ° pulse on ^{1}H, a 3 s recycle delay, and a 2 ms

contact time. For polymeric samples, 1200 scans were acquired while 4800 scans were acquired for polymer/cement samples. All spectra were referenced to glycine at 176.06 ppm and processed with 100 Hz linebroadening. Data were background corrected by subtracting the spectrum for an empty rotor and a cement control for polymeric samples and polymer/cement samples, respectively.

4.4 Results and Discussion

Jang *et al.* [81] describe the hydrolysis of PEI in NaOH, which is characterized by a ring opening of the imide group to form amide and carboxyl functionalities (see Figure 4.2). This reaction results in the formation of a dipolymer with a PEI unit and a partially hydrolyzed PEI unit which retains one imide group. Kim *et al.* [80] describe a similar reaction, as shown in Figure 4.3, that is characterized by the hydrolysis of both imide groups. The hydrolysis of PEI, which creates amide and carboxyl functional groups, could potentially allow for further hydrogen bonding opportunities with the cementitious matrix which could translate into a fibre with increased bond to concrete. To determine if this reaction, which could lead to increased chemical bonding between PEI and cement, is occurring in cementitious matrices containing PEI, ^{13}C SPE and CP/MAS NMR spectroscopy were used to study raw PEI, hydrolyzed PEI, and PEI in white cement (hydration times of 7 and 28 days). ^{13}C chemical shifts for PEI and both possible PEI hydrolysis products were predicted using the ACD/13CNMR Predictor program (Advanced Chemistry Development, Inc.) [82].

Predictions were carried out on two repeat units of the polymer which were terminated using methyl groups. For simplicity, Figure 4.4 shows the labeled segment of PEI and hydroylzed PEI which correspond to the chemical shift predictions given in Table 4.1.

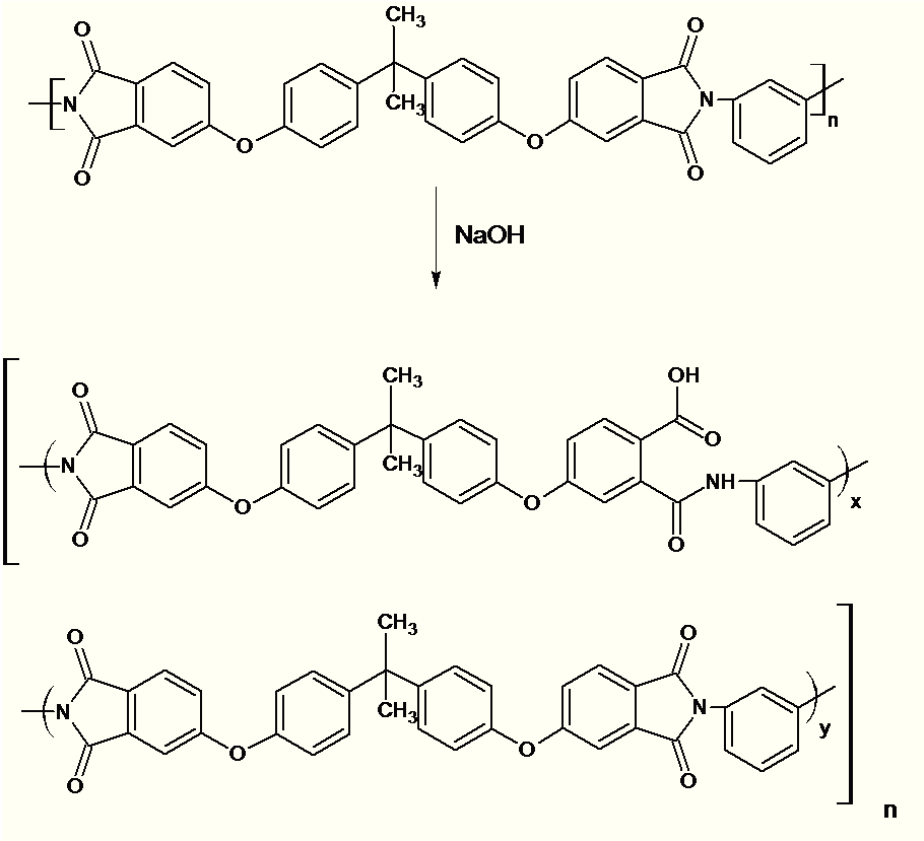

Figure 4.2: PEI hydrolysis in NaOH as proposed by Jang *et al.* [81].

From the predicted ^{13}C chemical shifts, it is evident that the NMR spectra of both PEI hydrolysis products, proposed by Jang *et al.* [81] and Kim *et al.* [80], shown in Figures 4.2 and 4.3, will be quite similar. For this reason, it can be assumed that either one or two imide ring openings would not be distinguishable; however, the comparison of the PEI and hydrolyzed PEI ^{13}C chemical shift predictions suggests that an increase

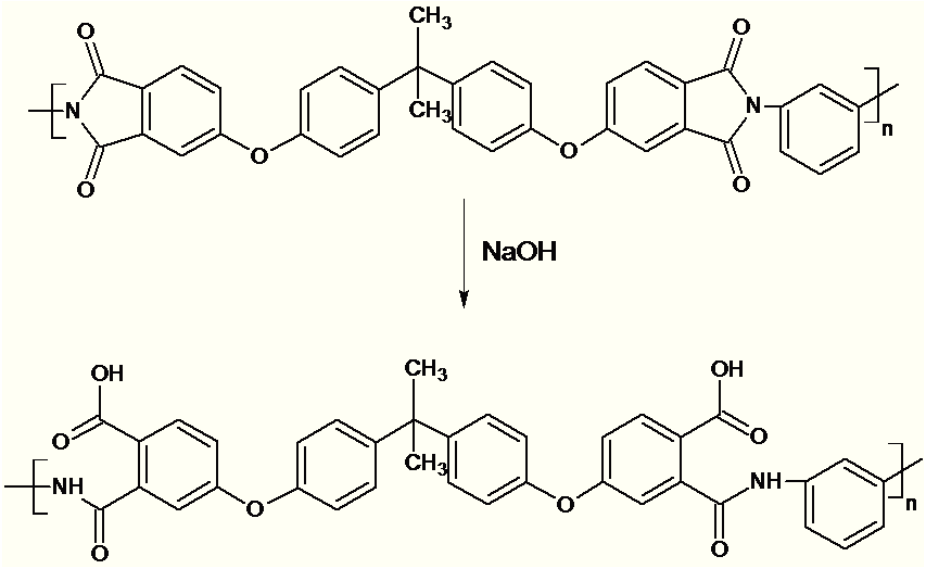

Figure 4.3: PEI hydrolysis in NaOH as proposed by Kim *et al.* [80].

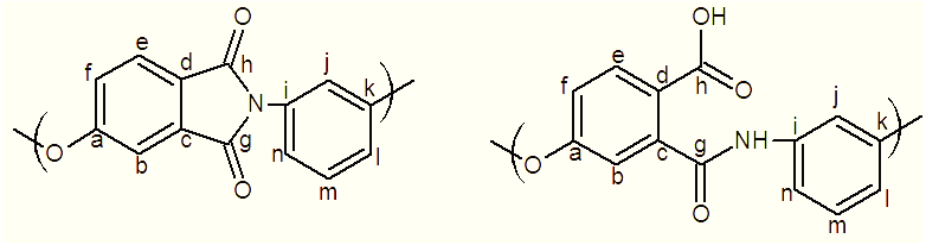

Figure 4.4: PEI and hydrolyzed PEI segments.

in intensity and/or spectral broadening may be observable between 170 and 120 ppm indicating hydrolysis of imide. Using the predicted ^{13}C chemical shifts, stick spectra were prepared for the region of interest between 170 and 120 ppm (see Figure 4.5). The predicted stick spectra clearly illustrate the potential for spectral broadening and possible integrated intensity increase in the spectral region between 170-120 ppm as a result of imide hydrolysis. ^{13}C CP/MAS NMR spectra of PEI, hydrolyzed PEI, PEI/white cement (7 and 28 day hydration) are shown in Figure 4.6. Resonances are assigned as the imide carbonyl (165 ppm), O−Ar (152 ppm), N−Ar (133 ppm), Ar

Table 4.1: ^{13}C Spectral predictions for PEI and hydrolyzed PEI

Atom Labe[1]l	PEI	Hydrolyzed PEI[2]	Hydrolyzed PEI[3]
a	161.2	160.2	160.2
b	114.7	112.6	112.0
c	128.1	136.3	134.6
d	120.9	124.6	124.6
e	126.7	134.1	134.2
f	124.7	121.2	121.3
g	165.1	156.3	156.3
h	165.6	167.1	167.2
i	133.7	136.2	135.7
j	111.1	107.3	108.6
k	133.7	135.9	135.7
l	120.9	116.7	116.8
m	128.7	127.7	129.4
n	120.7	118.5	116.8

[1] Atom labels shown in Figure 4.4
[2] Jang *et al.* Product
[3] Kim *et al.* Product

(125 ppm), C (42 ppm), and CH_3 (31 ppm) and are consistent with the predicted values, where Ar indicates an aromatic ring. Difference spectra were calculated by subtracting the spectrum of PEI from the hydrolyzed PEI and PEI/white cement spectra. The difference spectra, shown in Figure 4.7, are characterized by two broad resonances between 168-162 and 136-130 ppm. These resonances are consistent with those predicted by ACD software and are indicative of the ring opening reaction of the imide groups in the presence of base.

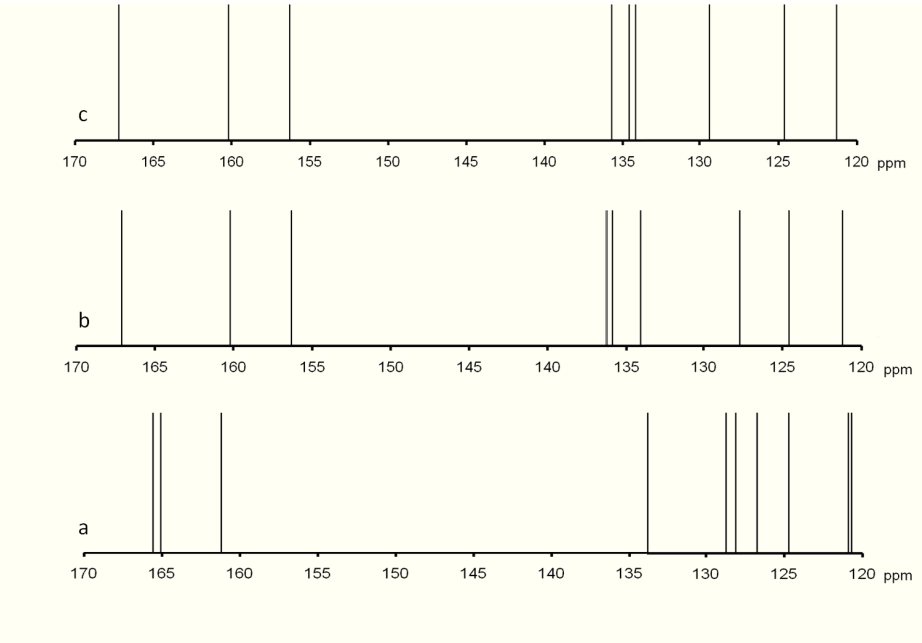

Figure 4.5: Predicted ^{13}C NMR stick spectra of PEI and hydrolyzed PEI products between 170-120 ppm. The letters a, b, and c represent PEI, hydrolyzed PEI as proposed by Jang *et al.* [81], and hydrolyzed PEI as proposed by Kim *et al.* [80], respectively. Detailed chemical shift values for the spectra are reported in Table 4.1.

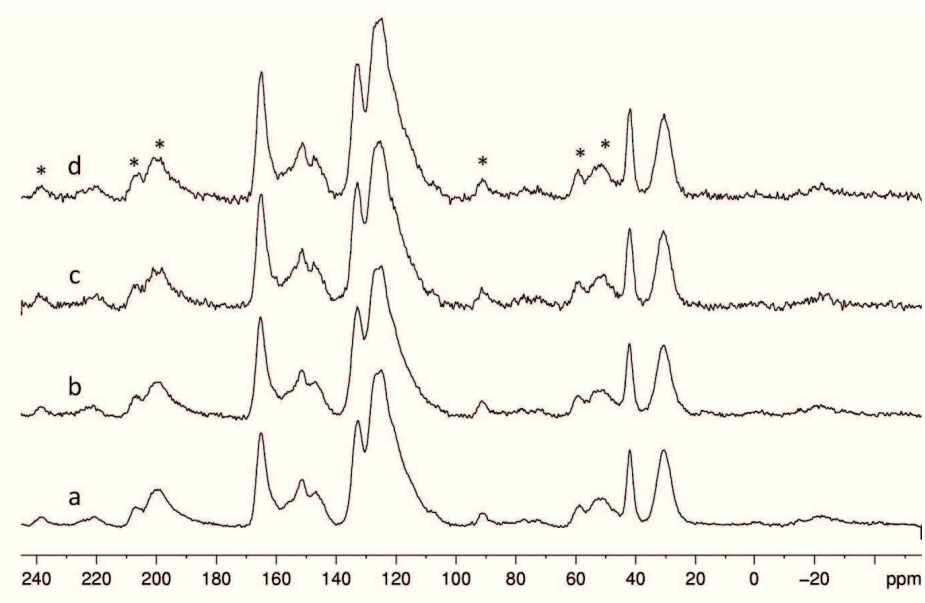

Figure 4.6: ^{13}C CP/MAS NMR spectra of (a) PEI, (b) hydrolyzed PEI, (c) PEI/white cement (7 day hydration), and (d) PEI/white cement (28 day hydration).

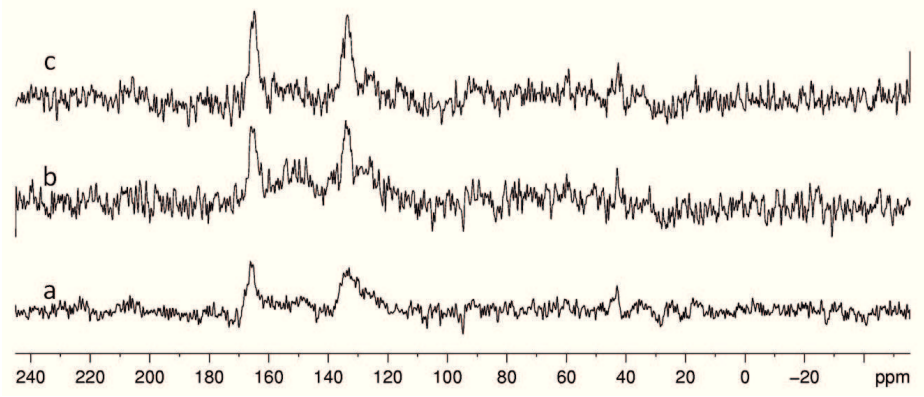

Figure 4.7: ^{13}C CP/MAS NMR PEI difference spectra. PEI spectrum was subtracted from (a) hydrolyzed PEI, (b) PEI/white cement (7 day hydration), and (c) PEI/white cement (28 day hydration).

In the CP NMR experiments, the observed spectrum is dependent upon the through space dipole-dipole coupling between the excited nucleus and the observed nucleus; for instance, ^{1}H and ^{13}C, respectively. Therefore, ^{13}C signals will be more intense for sites which are in close proximity to protons and absent for those ^{13}C sites which are too far from protons to couple and accept magnetization transfer. In contrast, with a SPE NMR experiment, all ^{13}C nuclear spins present in the samples will be observed in the NMR spectrum and have no direct intensity dependence on surrounding nuclei like in a CP experiment. Therefore, when quantification is of interest, SPE NMR experiments are employed.

SPE ^{13}C NMR spectra, shown in Figure 4.8, were acquired and difference spectra (Figure 4.9) were calculated as previously described (*vide supra*) for the ^{13}C CP/MAS study. The SPE ^{13}C NMR difference spectra are characterized by similar resonances as observed in the ^{13}C CP/MAS spectra; however, with this experiment it is concluded that between 7 and 28 days of hydration PEI is hydrolyzed, forming

increasing amounts of polymer containing carbonyl and amide functional groups. To estimate the relative extent of PEI hydrolysis in both the NaOH solution and cementitious matrices, the ratio of integrated intensities of the suspected region of intensity increase (approximately 170-120 ppm, as a result of imide hydrolysis) was calculated using the CH_3 peak as an internal standard, as this site remains unchanged throughout the hydrolysis reaction. At one week of hydration in the cementitious matrix, the increase in integrated intensity between 170-120 ppm is less than 1% and at 28 days of hydration, approximately 4%. These increases in integrated intensity suggest that the imide hydrolysis in PEI is minimal in the cementitious matrix, which is consistent with Trottier's work [13]. In the synthesized hydrolyzed PEI (made by reacting PEI with aqueous 0.5 M NaOH solution) showed a more substantial intensity increase, approximately 20%, in this region. It is speculated that the reaction proceeded more readily in the NaOH solution as compared to the hindered hardened cement paste environment.

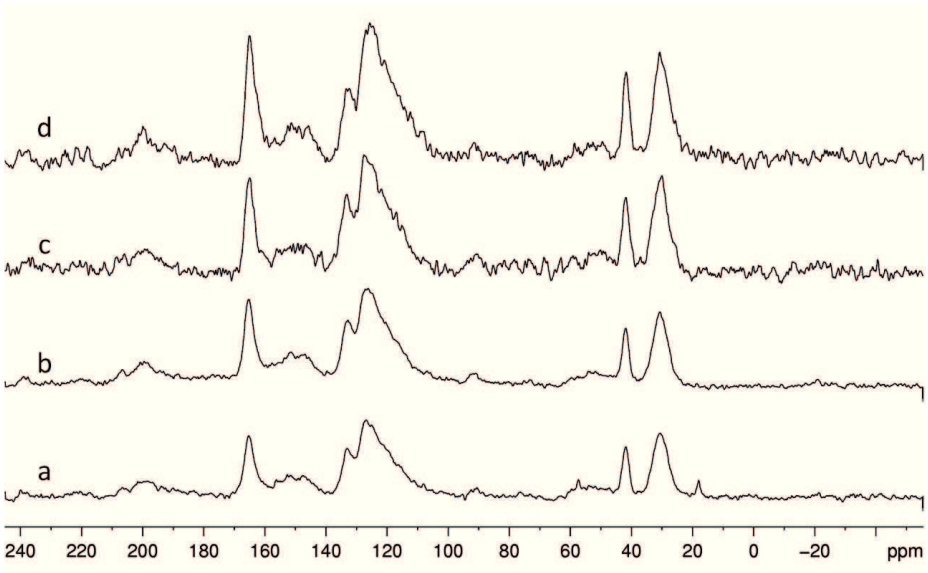

Figure 4.8: SPE ^{13}C NMR spectra of (a) PEI, (b) hydrolyzed PEI, (c) PEI/white cement (7 day hydration), and (d) PEI/white cement (28 day hydration).

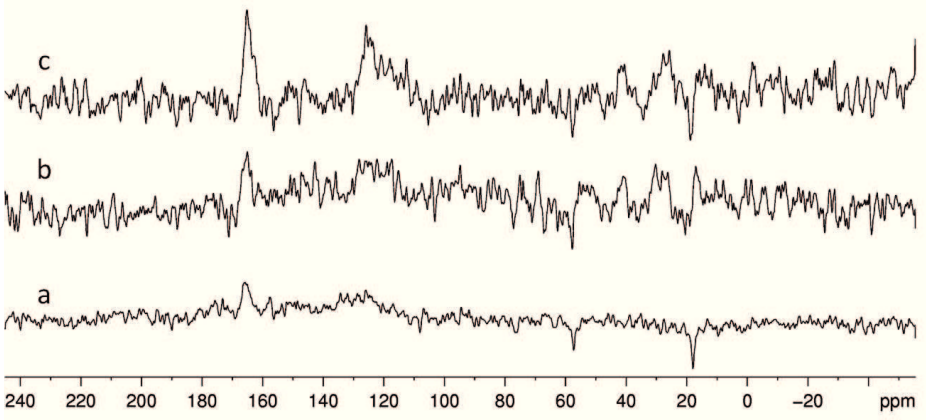

Figure 4.9: SPE ^{13}C NMR PEI difference spectra. PEI spectrum was subtracted from of (a) hydrolyzed PEI, (b) PEI/white cement (7 day hydration), and (c) PEI/white cement (28 day hydration).

4.5 Summary

This study has shown that PEI is susceptible to hydrolysis, albeit minimally, in a cementitious environment, which is consistent with the findings of Trottier [13].

The ring opening of the imide functional group to form amide and carboxyl groups will induce some flexibility in the polymer backbone and it is speculated that the carboxylic acid functional groups formed through hydrolysis could provide additional hydrogen bonding between the PEI fibre and concrete thus increasing the fibres' potential to toughen a concrete composite in fibre-reinforced concrete applications. Due to temperature limitations of the experimental extrusion line, which is used for fibre production, PEI fibres could not be extruded. As a result, mechanical testing on PEI/concrete composites was not conducted to estimate PEI's suitability as a fibre candidate for fibre reinforced concrete applications.

Chapter 5

Poly(vinylidene fluoride)/White Cement Study

5.1 Background

Poly(vinylidene fluoride), PVDF, is a semi-crystalline fluoropolymer which is commercially available as powder, pellets, and films. As a result of its high chemical resistance and ease of melt processing, PVDF was chosen by Trottier [13] as a candidate for fibre reinforced concrete applications. The chemical structure of PVDF is shown in Figure 5.1.

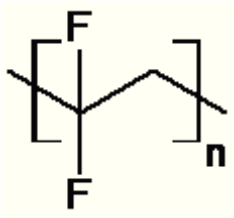

Figure 5.1: Chemical structure of poly(vinylidene fluoride).

PVDF has four polymorphs, α, β, γ, and δ [83]. Of direct interest to this work are the α and β phases, formed from crystallization of the melt and solid state drawing [13, 84–86], respectively. The β polymorph chemical structure is shown in Figure 5.2. β-PVDF is characterized by the alignment of all fluorines on one side of the carbon chain and all of the protons on the opposite side causing a poled structure. The polarized

β-PVDF structure, which is achieved when fibres are drawn, is thought to potentially increase the chemical bonding between the PVDF fibre and the concrete matrix via hydrogen bonding. Figure 5.3 demonstrates the hydrogen bonding potential between the partially positive region of β-PVDF and the hydroxide groups in white cement.

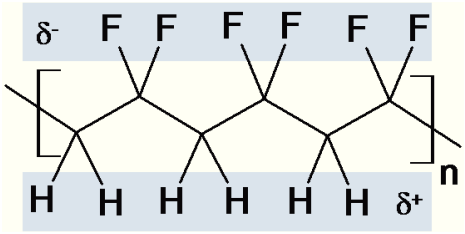

Figure 5.2: Chemical structure of β-PVDF.

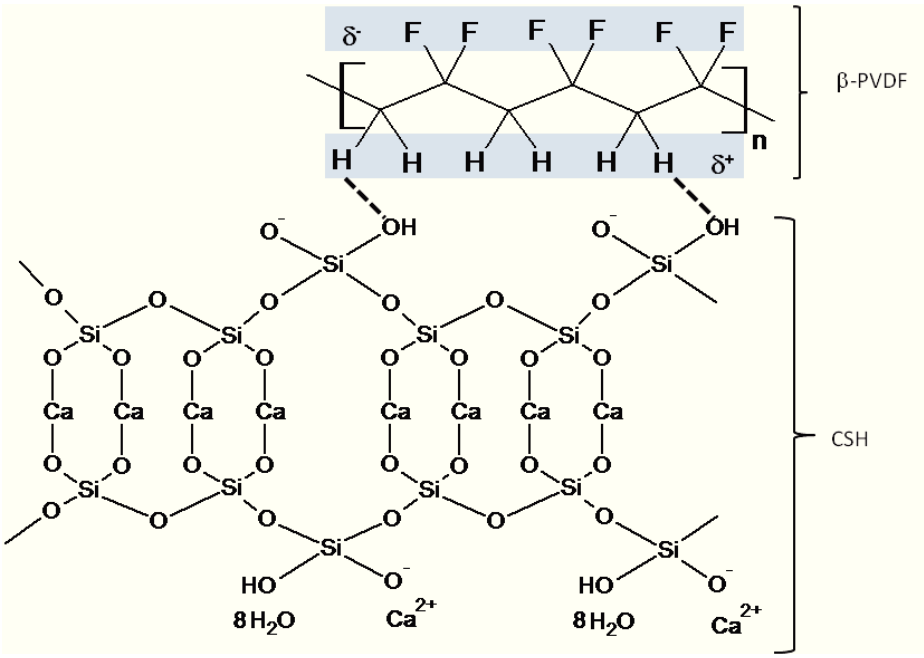

Figure 5.3: Potential hydrogen bonding between β-PVDF and hydroxide in cementitious matrices.

When choosing polymeric material with which to draw fibres for use in concrete reinforcement applications, it is important to consider the polymer's chemical resistance

to a basic environment. Despite being classified as a material with broad chemical resistance, there are some examples in the literature which report that under basic conditions PVDF powder and film can undergo degradation via dehydrofluorination [87,88]. It has also been reported that PVDF which has been dehydrofluorinated (discussed in further detail in Section 5.4.1), causing a brown to black colour change from its initial white colour, can result in a reduction in mechanical properties [89,90].

The objective of this work was to study the chemical stability of PVDF powder in white cement to gain insight into stability issues which may arise in PVDF fibre reinforced concrete composites.

5.2 Sample Preparation

PVDF powder was purchased from Sigma-Aldrich and was sieved to separate a particulate size of 150 μm using ASTM E-11 sieves (ELE International) and a RO-TAP testing sieve shaker. White cement paste ($w/c = 0.40$, introduced in Chapter 1), containing 20% PVDF by cement weight, was cast in silicone moulds and sealed in a plastic container for 7 and 28 day hydration periods. When the appropriate hydration times were achieved, samples were frozen in liquid nitrogen and freeze dried to remove all free water to cease hydration. Samples were stored and ground for NMR analysis in a N_2 atmosphere.

PVDF powder (approximately 0.7 g) was reacted with 50 mL of 0.5 M NaOH at 80 °C for 5 hours with continuous stirring. The brown particulate, presumed to be dehydrofluoronated PVDF, was recovered by filtration and was dried in a desiccator

prior to analysis.

5.3 Experimental

5.3.1 NMR Spectroscopy

All ^{13}C single pulse and CP/MAS NMR experiments were conducted on a 700 MHz Bruker Avance NMR spectrometer operating at a magnetic field of 16.4 T at a spinning frequency of 10 kHz using a 4 mm probe. ^{13}C single pulse spectra were acquired after a 4.6 μs 90 $^\circ$ pulse and a recycle delay of 5 s. An average of 128 and 5120 scans were acquired for PVDF and PVDF/white cement samples, respectively. ^{13}C CP/MAS spectra were acquired following a 4 μs 90 $^\circ$ pulse on ^{1}H, a contact time of 2 ms, and a 5 s recycle delay. Each spectrum resulted from an average of 4800-5120 scans. Spectra were background corrected by subtracting either the spectrum of an empty rotor (for PVDF samples) or the appropriate cement control spectrum (for PVDF/white cement samples). Data were processed with linebroadening of 100-200 Hz.

^{19}F single pulse experiments were conducted on a 700 MHz Bruker Avance NMR spectrometer operating at a magnetic field of 16.4 T at a spinning frequency of 29 kHz using a 2.5 mm probe. ^{19}F spectra were acquired following a 2.65 μs 90 $^\circ$ pulse, a recycle delay of 6 s and 64-128 scans were averaged. Spectra were background corrected by subtracting the spectrum of an empty rotor.

5.3.2 Infrared Spectroscopy

Infrared spectra of PVDF and dehydrofluorinated PVDF were recorded using the Nujol mull technique (NaCl windows) with a Perkin Elmer Spectrum 100 FT-IR Spectrometer. Spectra were acquired in the mid-IR region from 4000-600 cm^{-1} with 8 cm^{-1} resolution and an average of 32 scans.

5.3.3 Bromination Qualitative Test for the Presence of Alkene

A control sample was created in a test tube containing approximately 0.5 mL of dichloromethane (CH_2Cl_2) and 3 drops of 5% Br_2 in CH_2Cl_2 solution. Using the same set up, approximately 0.02 g of dehydrofluorinated PVDF was added to the 0.5 mL of CH_2Cl_2 prior to the addition of bromine. Samples were mixed thoroughly and were monitored for a period of 4 hours.

5.3.4 Ultraviolet-Visible Spectroscopy

Ultraviolet-Visible (UV-Vis) spectra were acquired on a Cary 5000 UV-Vis-NIR spectrophotometer in the wavelength range of 200-800 nm. Powdered samples of PVDF, dehydrofluorinated PVDF, white cement and PVDF/white cement were ground with a mortar and pestle and sandwiched between quartz discs for analysis.

5.4 Results and Discussion

5.4.1 Dehydrofluorination of PVDF Mechanistic Pathways

The C−F bond is the strongest of all carbon halogen single bonds. This makes fluorine a poor leaving group in eliminations and substitutions of alkyl halides. There are three possible mechanisms [51,91] which could be followed in a basic environment for the dehydrofluorination of PVDF: the common bimolecular elimination, E2; its competing substitution reaction, S_N2; and the rare elimination by conjugate base, E1cB. Each of these mechanistic pathways will be discussed in further detail, with respect to PVDF in basic solution, starting with the E2 mechanism.

The E2 mechanism is a one step reaction where the hydroxide begins to remove the acidic proton while, at the same time, the fluorine begins to leave, finally forming a vinyl alkyl unit, water and a fluoride anion (Figure 5.4).

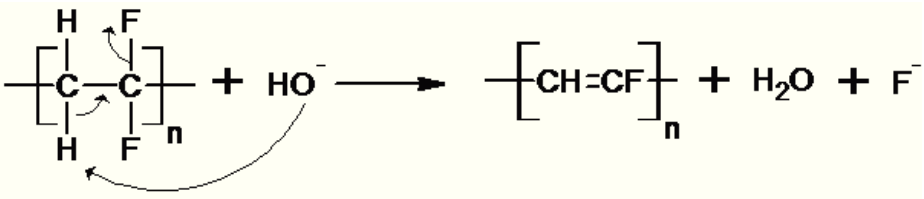

Figure 5.4: Bimolecular elimination (E2) mechanism.

Competing with this reaction is the S_N2 substitution (see Figure 5.5) that is characterized by the hydroxide nucleophile attacking the fluorine substituted carbon centre and displacing the fluorine to form a fluoroalcohol polymeric unit.

Another possible mechanistic route, although rare, for the reaction of PVDF and base is the E1cB mechanism (see Figure 5.6). This reaction is characterized by a two

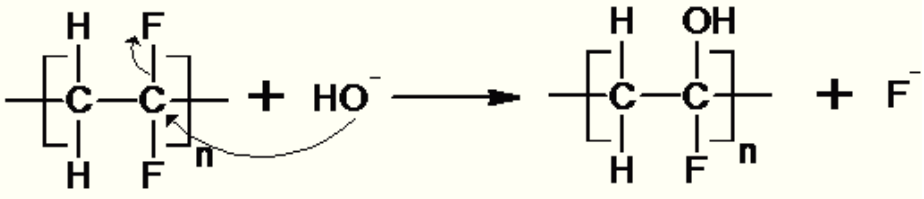

Figure 5.5: Nucleophilic substitution (S_N2) mechanism.

step process in which hydroxide removes an acidic proton to form a carbanion in a fast reversible step. In the slow step, the carbanion electron pair forms a double bond expelling a fluorine atom.

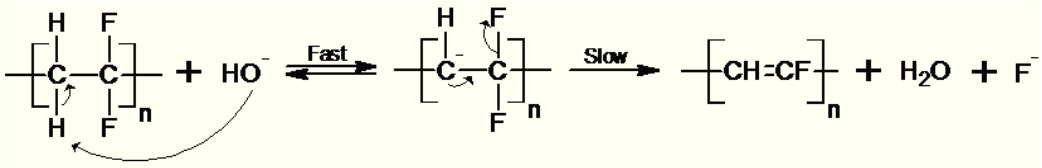

Figure 5.6: Elimination by conjugate base (E1cB) mechanism.

Following hydration, a light brown colour was observed in the PVDF/white cement samples, while the hydrated cement control remained white, indicating a chemical reaction had taken place between PVDF and white cement.

To characterize the brown product observed in the PVDF/white cement samples, PVDF powder was reacted with 0.5 M NaOH at 80 °C for 5 hours. PVDF is hydrophobic and therefore sat on the surface of the NaOH solution. The brown reaction product settled to the bottom of the reaction vessel (see Figure 5.7) and therefore it was easily isolated by filtration. Kise *et al.* [87, 88] observed that the colour of PVDF changes from white, to light brown, to black when reacted with NaOH/ethanol solution.

Although PVDF is highly resistant to many chemical environments, it has been

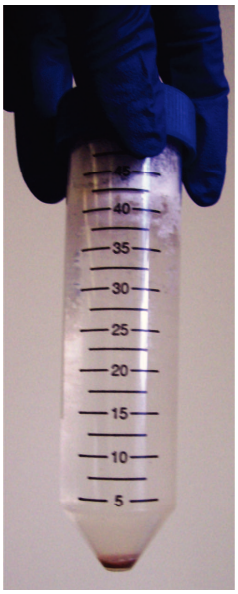

Figure 5.7: PVDF (brown particulate at the bottom of vial) and unreacted PVDF (white powder on the surface of NaOH solution).

shown that PVDF is degraded in caustic solutions [87,88,90]. In a basic environment, PVDF undergoes dehydrofluorination which results in conjugation of the backbone. Approximately 0.1 wt% of PVDF is affected by dehydrofluorination which is sufficient to cause a colour change from white to black [90].

5.4.2 SPE ^{13}C and ^{19}F NMR Spectroscopy

Holstein *et al.* [92] used ^{13}C CP/MAS NMR to study PVDF powder and reported chemical shifts of 43.2 ppm for CH_2 and 119.9 ppm for CF_2. Weak resonances in the region of 25 ppm were attributed to head-to-head or tail-to-tail defects (see Figure 5.8). It is estimated that defects in the structure of PVDF were between 3.5-6% of the backbone.

Pallathadka *et al.* [93] report chemical shift values for PVDF as 43 and 120 ppm

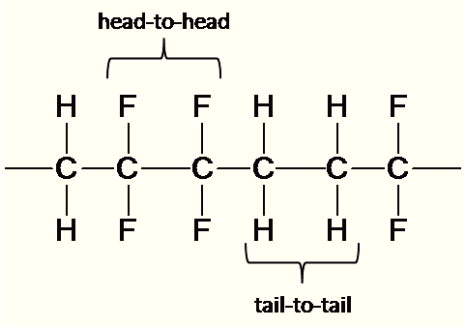

Figure 5.8: PVDF backbone defects.

for CH_2 and CF_2, respectively. In this work, consistent with the literature [92,93], ^{13}C chemical shifts for CH_2 and CF_2 are observed at 43.5 and 119.7 ppm, respectively (see Figure 5.9). The ^{13}C NMR spectrum of PVDF/white cement, shown in Figure 5.9c, is essentially the same as that of PVDF (the difference spectrum is shown in Figure 5.9a). As calculated by ACD/13CNMR Predictor [82], resonances from **C**H=CF and CH=**C**F would appear at approximately 103 ppm and between 170-178 ppm, respectively. Although dehydrofluorinated PVDF is brown in colour, only 0.1% of the backbone need be conjugated to produce the colour [87,88,90], thus ^{13}C NMR signals from the conjugated PVDF backbone would be weak or as in this work, unobservable.

Holstein *et al.* [92] carried out ^{19}F NMR experiments to characterize the fluorine sites of PVDF. They observed resonances at −91.2 ppm (amorphous domains), −81.8 and −96.1 ppm (crystalline domains), and −113.1 and −115.0 ppm (head-to-head and tail-to-tail defects). In this work, ^{19}F NMR resonances were observed at −92.1 ppm (amorphous domains), −82.7 and −96.8 ppm (crystalline domains), and −114.2 and −115.5 ppm (head-to-head and tail-to-tail defects), shown in Figure 5.10, consistent

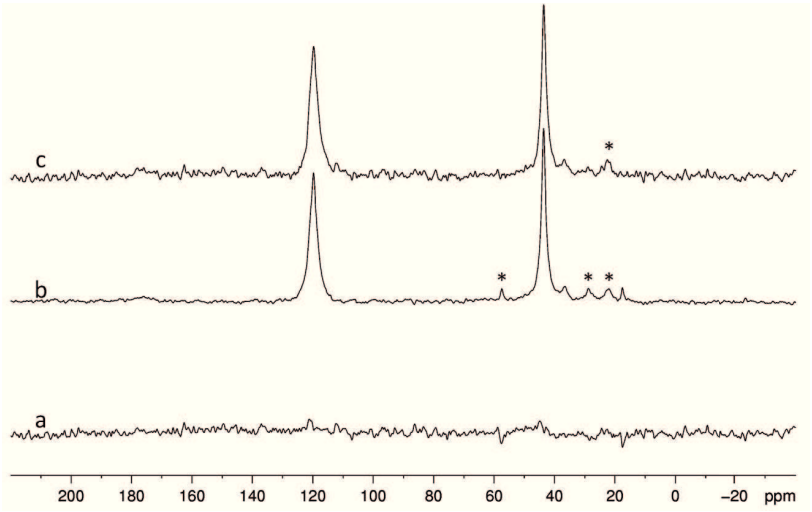

Figure 5.9: SPE ^{13}C NMR spectra of (a) difference spectrum (PVDF/white cement subtract PVDF), (b) PVDF, and (c) PVDF/white cement (* spinning sidebands).

with Holstein [92]. The ^{19}F NMR spectra of PVDF, dehydrofluorinated PVDF are essentially the same as demonstrated in the difference spectrum (Figure 5.10a), and no new resonances indicative of CH=CF were observed.

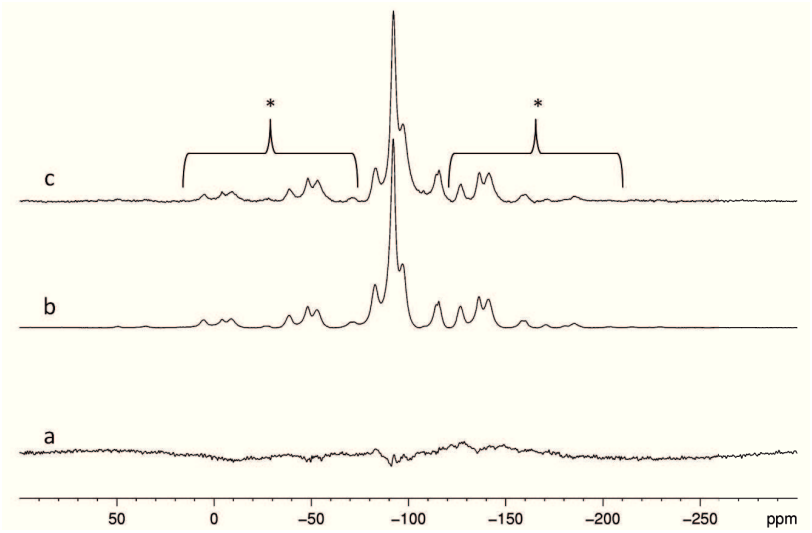

Figure 5.10: SPE ^{19}F NMR spectra of (a) difference spectrum (PVDF/white cement subtract PVDF), (b) PVDF, and (c) PVDF/white cement (* spinning sidebands).

5.4.3 Infrared Spectroscopy

The IR spectroscopic technique probes the vibrational modes of a molecule [94]. Using the Nujol mull technique, in which a solid is ground in mineral oil to create a suspension, and a temporary NaCl cell, IR spectra of Nujol, PVDF/Nujol, and dehydrofluorinated PVDF/Nujol were acquired (shown in Figures 5.11 and 5.12).

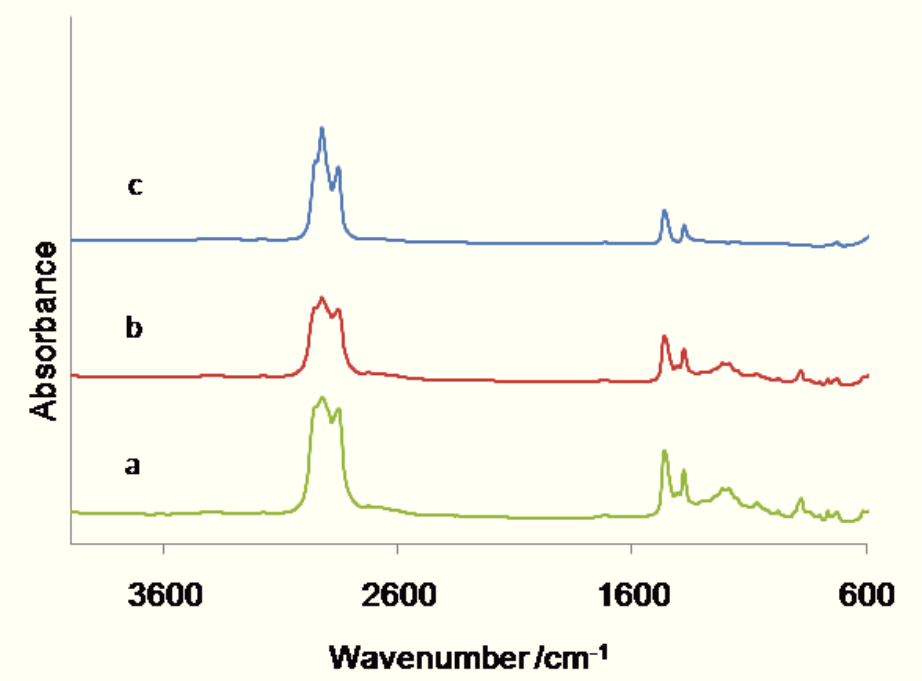

Figure 5.11: IR spectra of (a) dehydrofluorinated PVDF/Nujol, (b) PVDF/Nujol and (c) Nujol from 4000-600 cm^{-1}.

In Figure 5.11, the spectra from 4000-600 cm^{-1} show that major contributions to the spectrum can be assigned to the Nujol (3100-2000, 1772, 1470, 1442, and 778 cm^{-1}). The Nujol peaks were not problematic in this analysis as the region of interest where C=C frequencies would characteristically absorb is approximately 1600 cm^{-1} [94]. Figure 5.12 shows the 1700-600 cm^{-1} region in more detail. The

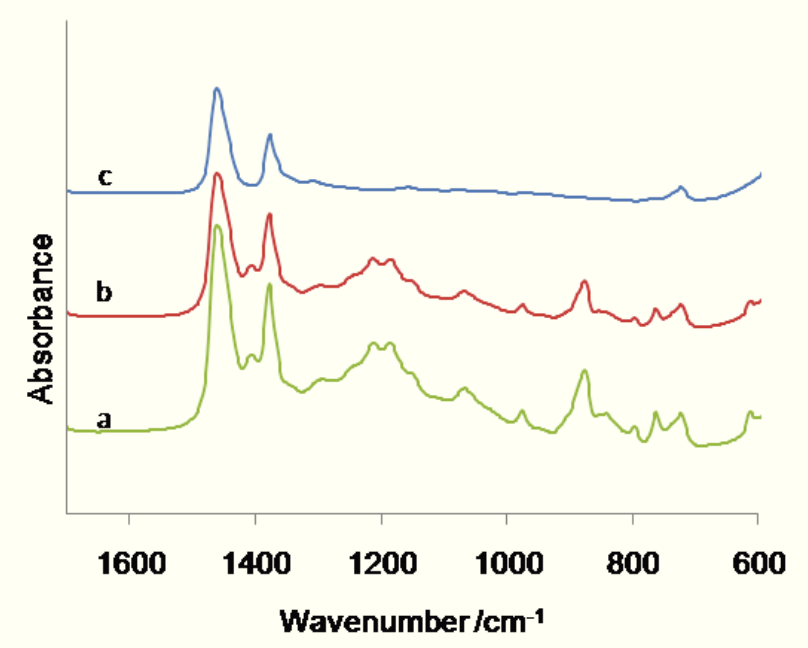

Figure 5.12: IR spectra of (a) dehydrofluorinated PVDF/Nujol, (b) PVDF/Nujol, and (c) Nujol from 1700-600 cm^{-1}.

PVDF spectrum was assigned from 1600-600 cm^{-1}, summarized in Table 5.1, and is consistent with the literature [95–101].

Table 5.1: Vibrational assignment of PVDF powder

Observed Band /cm^{-1}	Vibrational Mode	Reference
1424	CH_2 scissor, CH wag	[99]
1336-1118	CF stretch, CC and CCC vibrations	[98–101]
	CF out-of-plane deformation	
1084	CC vibrations, CH wag, CF wag	[99]
994	CH out-of-plane deformation	[95, 96, 98]
886-862	CH rocking, CH wag, CF wag	[95–99]
816	CH out-of-plane wag	[95, 96, 98]
770	CF_2 bending, CH_2 rocking	[95, 96]
620	CF_2 bending, C skeletal bending	[95, 97, 98]

Stretching frequencies are observed between 1336-1118 cm^{-1} (CF, CC, CCC) [98–101] and at 1084 cm^{-1} (CC) [99]. CH wagging vibrations are assigned at 1424 [99],

1084 [99], and 886-862 cm^{-1} [95–99]. CF wagging vibrations are observed at 1084 [99] and 886-862 cm^{-1} [95–99]. CH_2 rocking vibrations are assigned at 886-862 [95–99] and 770 cm^{-1} [96, 99]. Bending vibrations are observed at 770 (CF_2) [96, 99] and 620 cm^{-1} (CF_2 and C backbone) [95, 97, 98]. The spectra of PVDF and dehydrofluorinated PVDF are the same and a frequency indicative of C=C vibration was not observable (likely due to the low concentration of C=C produced in the dehydrofluorination reaction).

5.4.4 Bromination of Dehydrofluorinated PVDF

In organic chemistry, a common qualitative test for the presence of alkenes is the bromination addition reaction. As shown in Figure 5.13, when an orange coloured Br_2/CH_2Cl_2 solution is added to a sample containing an alkene, the bromine adds across the double bond and the resultant solution is colourless.

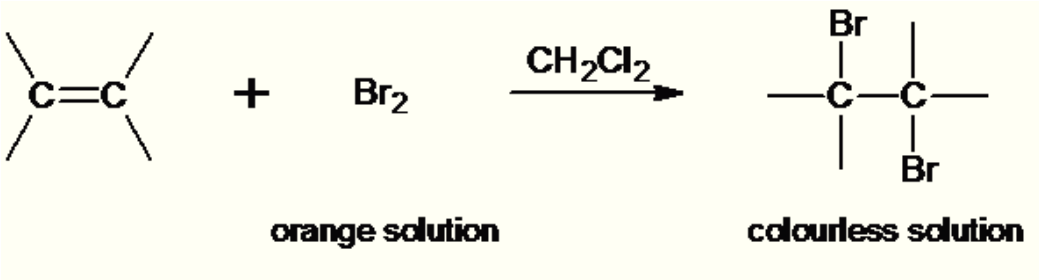

Figure 5.13: Schematic chemical equation for the bromination addition reaction to an alkene.

Bromine addition to alkenes can be inhibited by the presence of electron withdrawing groups, such as the fluorine substituent in dehydrofluorinated PVDF. The bromination qualitative test for alkene was carried out on dehydrofluorinated PVDF.

The reaction occurred slowly; however, after 4 hours the test solution containing the polymer had decolourized, resulting in a light yellow solution, indicating a positive test for alkene (see Figure 5.14).

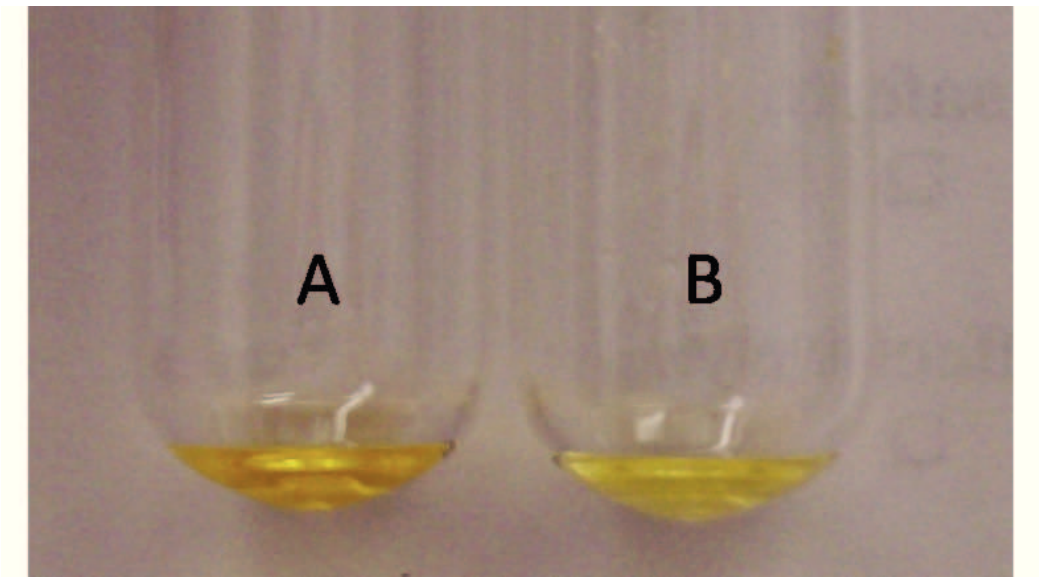

Figure 5.14: Qualitative test for bromination of dehydrofluorinated PVDF. (a) 5% Br_2/CH_2Cl_2 in 0.5 mL CH_2Cl_2 and (b) 0.02 g dehydrofluorinated PVDF and 5% Br_2/CH_2Cl_2 in 0.5 mL CH_2Cl_2.

5.4.5 Ultraviolet-Visible Spectroscopy

The UV-Vis spectra of PVDF and dehydrofluorinated PVDF are shown in Figure 5.15. The dehydrofluorinated PVDF spectrum shows an absorbance maximum at 471 nm while the PVDF spectrum has no obvious maxima. In a polymeric band structure, the molecular orbitals are delocalized and the energy levels produce a virtual continuum in which a band gap is present between the π bonding and π^* anti-bonding orbitals [102]. This band gap would be larger in a smaller molecule such as ethene as shown in Figure 5.16 for comparison. PVDF is white in colour, does not

contain π bonds, and does not absorb in the UV-Vis region of the electromagnetic spectrum. Brown coloured dehydrofluorinated PVDF, as discussed in Section 5.4.1, has less than 0.1% of the backbone in conjugated form. The brown colour (red-orange wavelengths of light) observed is a result of the absorption of blue-green light, and the π-π^* transition occurs at low energy (2.63 eV) and long wavelength (471 nm). Cho *et al.* [89] report an absorption for dehydrofluorinated PVDF at 519 nm in the UV-Vis spectrum, which is comparable to the absorption observed in this work.

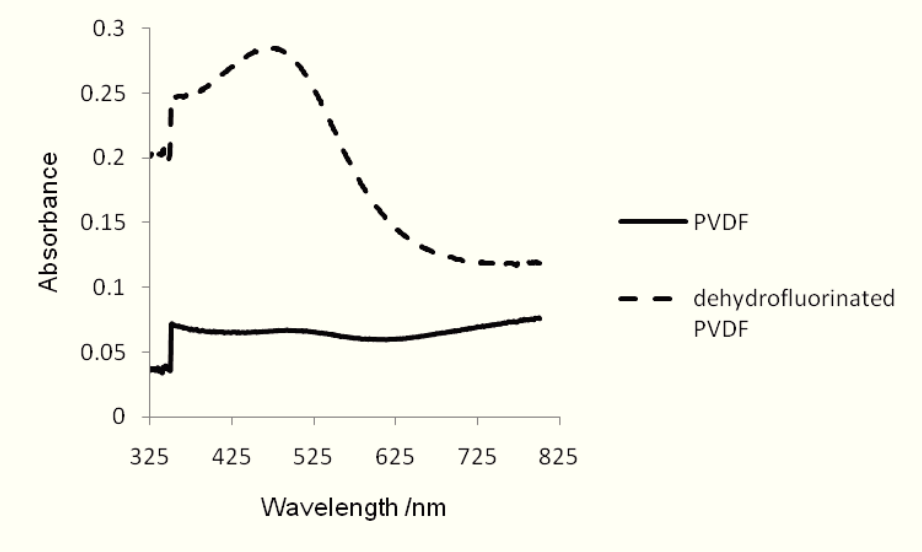

Figure 5.15: UV-Vis average spectra of PVDF (solid line) and dehydrofluorinated PVDF (broken line).

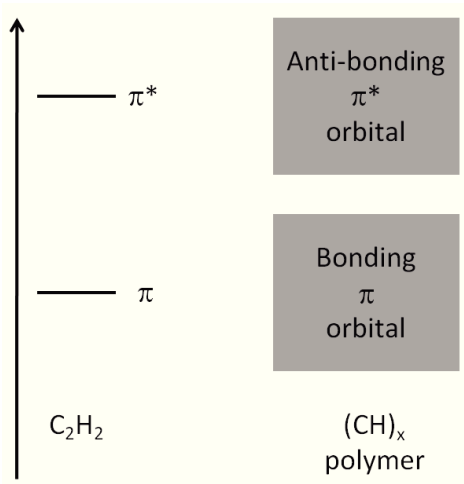

Figure 5.16: Effect of conjugation on energy band gap. Styled after White [102].

A similar experiment was conducted on cementitious PVDF samples. The UV-Vis spectra of white cement and PVDF/white cement are shown in Figure 5.17. Although, not as pronounced as the absorption in the dehydrofluorinated PVDF spectrum (Figure 5.15), a similar trend is observed in the PVDF/white cement spectrum indicating that the brown colour of this sample is due to the conjugation of the PVDF backbone in the basic cementitious environment, which suggests an E2 or E1cB pathway for dehydofluorination of PVDF in cement.

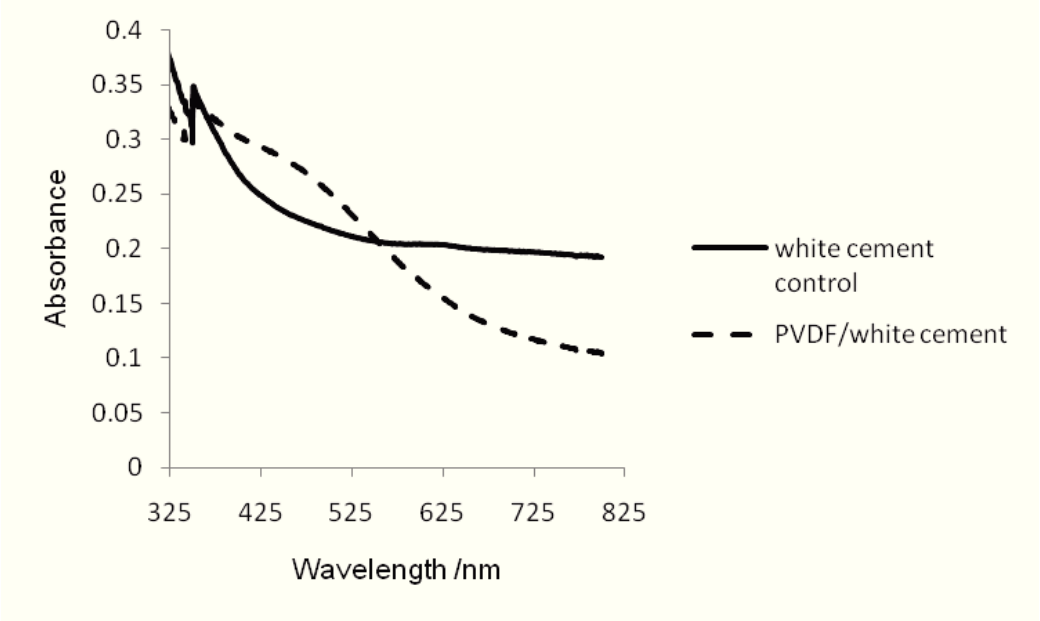

Figure 5.17: UV-Vis average spectra of white cement (solid line) and PVDF/white cement (broken line).

5.5 Summary

In this study, dehydrofluorinated PVDF was synthesized from PVDF powder. The dehydrofluorinated PVDF was studied via SPE ^{13}C and ^{19}F NMR, IR, and UV-Vis spectroscopic techniques. Evidence for CH=CF conjugation in the brown PVDF product was not observable with NMR or IR methods. This is likely due to the very small percentage of conjugation needed to change the colour of PVDF from white to black. Qualitative testing for alkene was carried out by bromination and the light yellow colour indicated a partial decolourization of Br_2 solution and a positive result for the presence of alkene. UV-Vis absorption was observed at 471 nm in brown coloured PVDF and PVDF/white cement samples. This evidence confirms that the

brown coloured PVDF/white cement sample is the result of the dehydrofluorination of the PVDF backbone in the basic cementitious environment.

Chapter 6

Short and Long Range Studies of the Polymeric Material/White Cement Interfacial Transition Zone

6.1 Background

The bond between a polymeric fibre and concrete, as well as the structure of the interfacial transition zone, are of chief importance when determining a fibre's suitability as a concrete reinforcement. To study the interfacial interactions between a polymeric material and cement at short range (angstrom scale) and at long range (micron scale), solid state NMR spectroscopy and scanning electron microscopy were employed.

The CP/MAS NMR technique, as described in Chapter 2, exploits through space dipole-dipole interactions to give information about heteronuclei in a sample. To isolate the polymeric powder/white cement interface with this technique, a heteronuclear pair must first be determined such that one nucleus is only associated with the polymeric material and the other with the cementitious matrix. Many polymeric materials of interest for concrete reinforcement contain protons. In an effort to study the interactions between, for example, protons (^{1}H) from polyolefin and the cement

(*e.g.*, ^{27}Al, ^{29}Si or ^{43}Ca), cementitious protons must be removed. In hardened cement, the major proton source is water, so it was speculated that carrying out hydration of cementitious samples with heavy water, D_2O, would reduce or effectively eliminate the proton signals from the cement. It was found that despite the D_2O hydration, samples still contained a considerable amount of water, as confirmed by the ^{27}Al CP signal observed in the control sample. Therefore, the signals observed in the ^{27}Al CP/MAS NMR experiments, for instance, could not be assigned to an interfacial interaction.

Since it proved difficult to remove water from the cementitious matrix even with D_2O hydration, perfluorinated polymers (poly(tetrafluoroethylene), Teflon, and poly-(tetrafluoroethylene-co-perfluoropropyl vinyl ether), PFA) were chosen as an additive in an effort to isolate interactions at the polymeric powder/white cement interface. Cement contains at most trace amounts of fluorine, which makes the CP/MAS NMR experiment between ^{19}F sites (in the polymer) and ^{27}Al sites (in cement) possible, thus isolating the interface. It is important to note that perfluorinated polymeric materials are speculated to have poor chemical bonding character with cementitious matrices due to their hydrophobic nature, therefore these polymers were chosen solely on their suitability for the CP/MAS NMR experimental requirements to isolate the polymeric powder/white cement interface. Based on chemical structure, see Figure 6.1, PFA would be expected to have more bonding potential with cement due to its ether linkage.

^{19}F and ^{27}Al SPE experiments and ^{13}C and ^{19}F $\longrightarrow$ ^{27}Al CP/MAS experiments

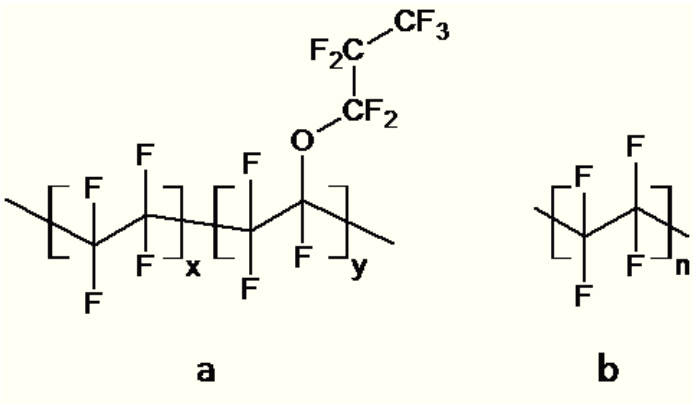

Figure 6.1: Chemical structure of (a) PFA and (b) Teflon.

were conducted to study polymeric degradation and chemical interactions at the fluoropolymer/white cement interface. The results of this study are discussed in Section 6.4.1.

To investigate the interfacial transition zone surrounding various fibres at long range (μm scale), which are currently and potentially could be used for concrete reinforcement applications, the SEM/EDS technique (as introduced in Chapter 2) was utilized. Scanning electron microscopy (SEM) coupled with energy dispersive spectroscopy (EDS) collects and analyzes the X-rays produced when a sample is bombarded with a beam of electrons. Since X-ray energies differ for each element, elemental mapping of a sample area can be achieved. This method is attractive for studying the interfacial transition zone between a fibre inclusion and cement paste as both visual and chemical differences in this region can be investigated simultaneously, with a spatial resolution on the micron scale, which could potentially elucidate characteristics of weak and strong fibre/concrete interfaces. The EDS technique requires that the sample surface be polished flat to avoid geometric effects in X-ray

detection. As a result of this requirement and cement polishing requirements, sample preparation for this study was quite extensive (see Section 6.2.2).

The interfacial transition zone was analyzed surrounding steel fibre as well as a variety of polymeric fibres, namely; HDPE/PP, PVA, PVDF, PEI, and Nylon 6.6. The chemical structures of these polymeric fibres are shown in Figure 6.2. As discussed in Chapter 1, Section 1.6.3.1, HDPE/PP, PVA, and Nylon 6.6 fibres are currently in use for fibre reinforced concrete applications [24,28,29,34–37]. PVA is known to exhibit a strong bond with the cementitious matrix as a result of its hydrophilic nature [34,35], while Nylon 6.6, despite possessing hydrophilic amide functional groups, exhibits poor bonding with cementitious matrices [28,29]. PVA and Nylon 6.6 fibres were therefore chosen for study as benchmark materials which exhibit strong and weak bonding, respectively, with cementitious matrices. The HDPE/PP fibre, although hydrophobic due to its chemical structure and thus its poor chemical bonding potential with cementitious matrices, was chosen for study because it is a common fibre type in the fibre reinforced concrete industry. It is important to note that the bond between HDPE/PP fibres and cementitious matrices is thought to be purely mechanical due to fibrillation of the fibres (during mixing) which serves to anchor them into the hardened matrix. PVDF and PEI fibres were chosen for study in this work to characterize the interfacial transition zone surrounding these materials, in relation to the benchmark fibre materials (PVA and Nylon 6.6) and the popular HDPE/PP fibre, to gauge their suitability as potential materials for fibre reinforced concrete applications.

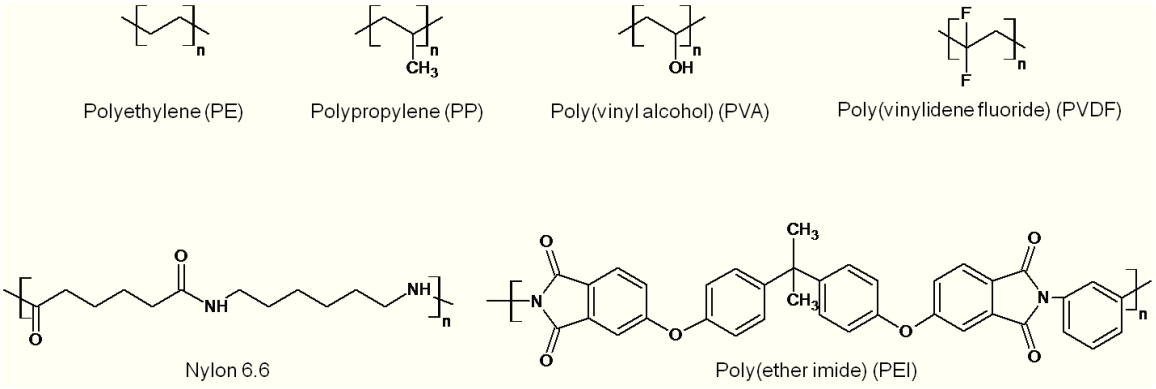

Figure 6.2: Chemical structure of polymeric fibres.

6.2 Sample Preparation

6.2.1 Nuclear Magnetic Resonance Samples

White cement paste, with a $w/c = 0.5$ to allow for complete hydration (see Chapter 1 for further details), was mixed with a light duty mixer until a smooth consistency was achieved (approximately 2 minutes). Fluoropolymer powder was folded into the cement paste and then agitated with a mixer.

White cement with 20% Teflon (1 μm particulate size, Sigma-Aldrich) by weight was cast in silicone moulds and hydrated for 1 week in a sealed plastic container. Following 1 week of hydration, the samples were ground to a powder for analysis.

PFA resin was purchased from CSI Plastics and was cryogenically milled to powder using a Spex SamplePrep 6770 Freezer Mill. Using a RO-TAP testing sieve shaker and ASTM E-11 sieves (ELE International), PFA particulate of less than 45 μm was separated. White cement with 20% PFA by weight was cast in a silicone mould and hydrated for 1 week in a sealed plastic container. Samples were ground to a powder

for NMR analysis.

6.2.2 SEM/EDS Samples

White cement paste, with a water to cement ratio of 0.35 (to ensure complete hydration and enable comparison with Bentur *et al.* [26]), was cast in 1.5 cm cube moulds with a single fibre embedded vertically in the centre. The samples were hydrated for 1 day in a sealed plastic container, 1 week in saturated $Ca(OH)_2$ solution, and the remaining hydration time in a sealed plastic container. The hardened fibre/cement composite samples were sectioned, perpendicular to the fibre, using a diamond saw with ethanol lubricant to expose the fibre/cement interface. Sections were freeze dried for 2 days to remove all free water. Samples were epoxy impregnated with low viscosity epoxy (EpoThin epoxy resin and hardener, Buehler Canada) in a vacuum desiccator (set-up shown in Figure 6.3). Epoxy impregnated fibre/cement composites were sectioned to re-expose the fibre/cement interface. Samples were polished with a series of diamond abrasives (70 μm and 30 μm discs and 15, 9, 6, 3, 1, and 0.25 μm pastes) to produce the flat surface required for SEM/EDS. Polished sections were coated with a 30 nm layer of Au/Pd to achieve a conductive surface. Figure 6.4 shows an example of fibre/white cement samples at various stages of processing for SEM/EDS analysis.

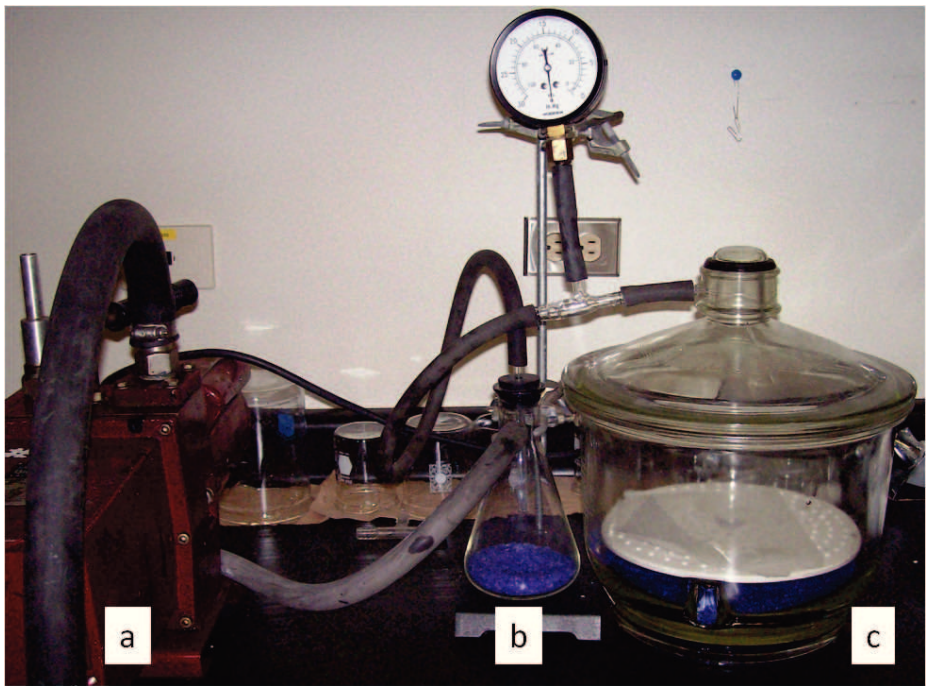

Figure 6.3: Epoxy impregnation apparatus. The letters a, b, and c indicate a vacuum pump, desiccant trap, and vacuum desiccator, respectively.

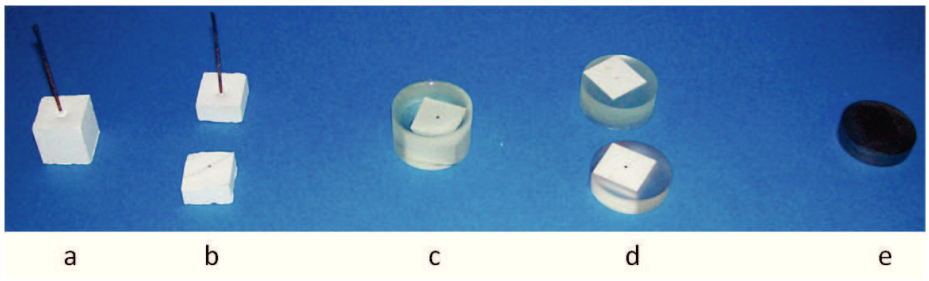

Figure 6.4: SEM/EDS fibre/white cement sample preparation. (a) fibre cast in cement cube, (b) sectioned cube, (c) sample following freeze drying and epoxy impregnation, (d) sectioned epoxy impregnated sample, and (e) polished section coated with Au/Pd.

6.3 Experimental

6.3.1 NMR Spectroscopy

All ^{19}F and ^{27}Al single pulse excitation (SPE) and cross-polarization (CP) experiments were conducted with a 700 MHz Bruker Avance NMR spectrometer operating at a magnetic field of 16.4 T using a 2.5 mm probe. Single pulse experiments were conducted at a spinning frequency of 25 kHz with the exception of ^{19}F experiments on samples containing PFA, which were spun at 20 kHz. ^{19}F SPE NMR spectra were acquired after a 3 μs 90 $^\circ$ pulse with 4-128 signal averaging scans. Recycle delays were between 10 and 30 s. Spectra were processed with linebroadening of 100-200 Hz. ^{27}Al single pulse spectra were acquired after a 0.5 μs pulse at an rf field strength of 59 kHz, using a recycle delay of 1 s and signal averaging 4096 scans. Data were processed with linebroadening of 50-100 Hz. ^{19}F $\longrightarrow$ ^{27}Al CP experimental parameters were setup using an AlF_3 reference material. ^{19}F $\longrightarrow$ ^{27}Al CP spectra were acquired following a 4 μs 90 $^\circ$ pulse on ^{19}F using a recycle delay of 15 s, contact times of 1, 2, and 5 ms at a spinning frequency of 15 kHz. Data were processed with linebroadening of 100-200 Hz.

^{13}C CP experiments (setup using glycine) were conducted with a 400 MHz Bruker Avance NMR spectrometer operating at a magnetic field of 9.4 T using a 4 mm probe at a spinning frequency of 7 kHz. ^{13}C CP spectra were acquired following a 4 μs 90 $^\circ$ pulse on ^{1}H using a contact time of 1 ms and a recycle delay of 10 s. For the cement control sample, 10,240 scans were collected and 100 Hz linebroadening was applied.

For the PFA/cement sample, 51,200 scans were collected and 150 Hz linebroadening was applied.

^{43}Ca SPE NMR spectra were acquired with a 900 MHz Bruker Avance II NMR spectrometer operating at a magnetic field of 21.1 T using a 7 mm single channel probe at a spinning frequency of 5 kHz. After a 1 μs 40 $^\circ$ pulse, spectra were acquired with 81,920 scans using a recycle delay of 2 s. Spectra were referenced to 2.0 M $CaCl_2$ solution at -14 ppm [49] and were processed with linebroadening of 200 Hz.

6.3.2 SEM/EDS

Fibre/white cement interfaces were examined with a Hitachi S-4700 SEM equipped with an Oxford Inca Energy Dispersive X-ray analysis system. An accelerating voltage of 12 kV was used. A current of 20 μA and a condenser lens setting of 5 was employed. Elemental maps were acquired using magnifications of 500$\times$ and 6.00k$\times$, with a live time of 600 s (approximately 500,000 counts). Point map data were acquired with a 90 s live time (approximately 300,000 counts) for each point.

6.4 Results and Discussion

6.4.1 Interfacial Interactions Between Fluoropolymeric Powder and White Cement at Short Range

SPE ^{27}Al MAS NMR spectra of Teflon/white cement, PFA/white cement, and a white cement control are shown in Figure 6.5. Following Rottstegge *et al.* [72], the ^{27}Al resonances were assigned as aluminum monosulfates (13 ppm), aluminum trisulfates

(10 ppm), and aluminum hydrates (3 ppm). From a comparison of these spectra, the local environments of the cementitious ^{27}Al sites do not seem to be affected by the presence of either Teflon or PFA powder.

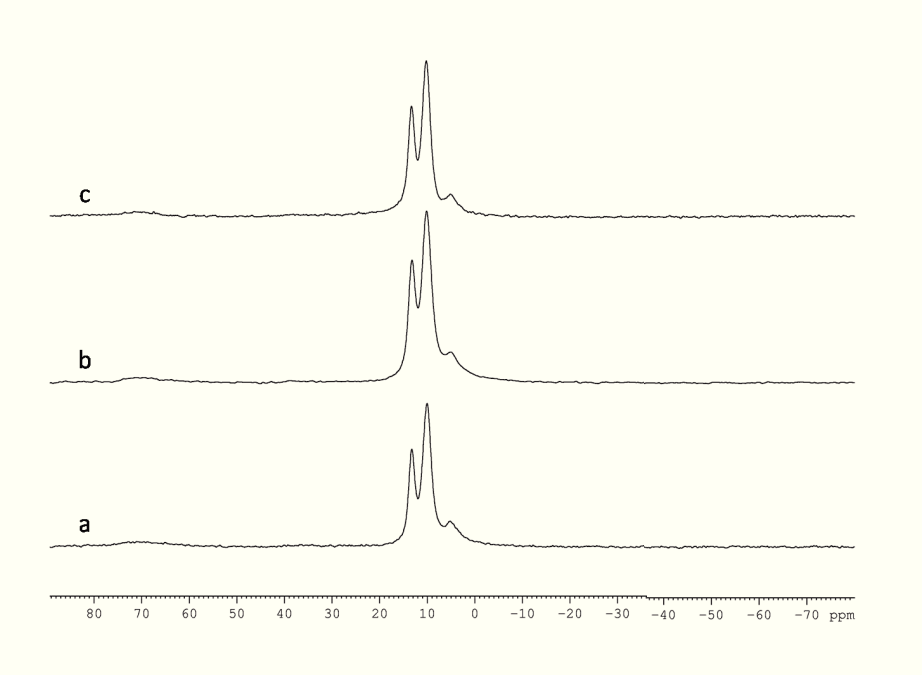

Figure 6.5: SPE ^{27}Al NMR spectra of (a) white cement control, (b) Teflon/white cement, and (c) PFA/white cement.

To determine if the polymeric ^{19}F sites are affected by the presence of the cement paste, SPE ^{19}F NMR spectra were acquired and examined. The SPE ^{19}F NMR spectra of Teflon and Teflon/white cement are shown in Figure 6.6. The Teflon spectra are quite simple, containing only one resonance at -123 ppm, which does not seem to be affected by the presence of the white cement. SPE ^{19}F NMR spectra of PFA, PFA/white cement and a white cement control are shown in Figure 6.7. Resonances for PFA are assigned based on the literature [103–105] as CF_3 (-82 ppm), OCF_2 (-81 ppm), CF_2 (-122 ppm), CF_2(side chain) (-130 ppm), and CF (-137 ppm). The

white cement control shows a minor fluorine signal; however, this is not substantial enough to interfere with the PFA resonances. The ^{19}F sites in PFA are not affected by the presence of the cementitious matrix.

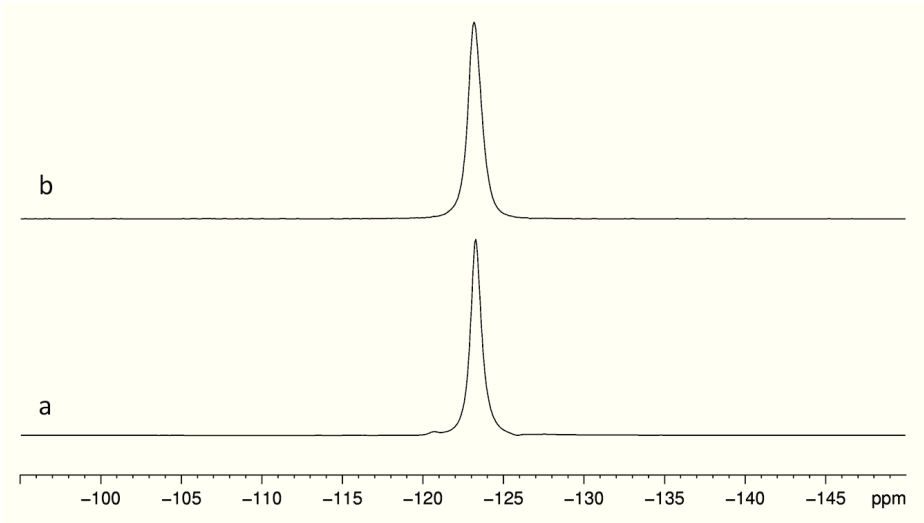

Figure 6.6: SPE ^{19}F NMR spectra of (a) Teflon and (b) Teflon/white cement.

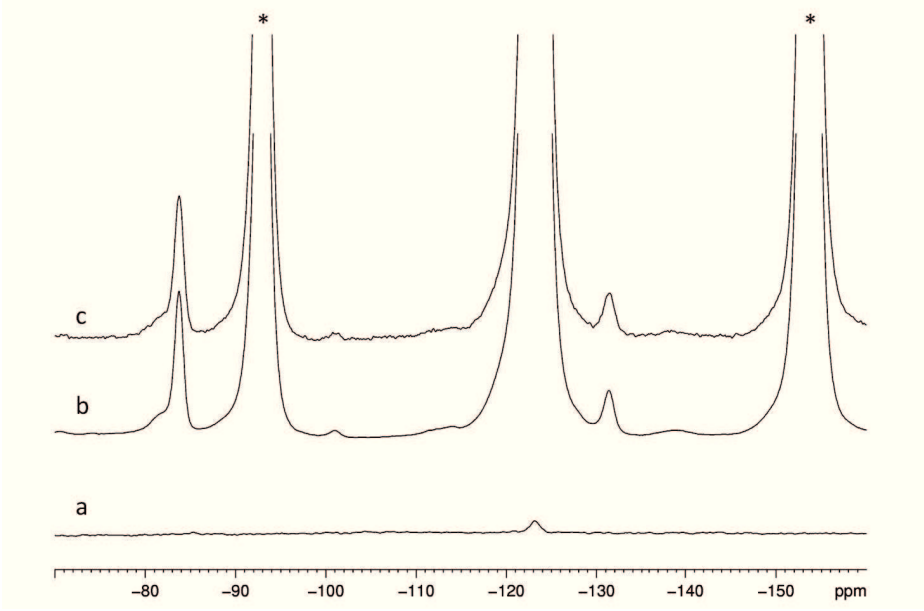

Figure 6.7: SPE ^{19}F NMR spectra of (a) white cement control, (b) PFA, and (c) PFA/white cement.

$^{19}F \longrightarrow {}^{27}Al$ CP/MAS NMR experiments were conducted to determine if interactions were detectable between polymeric fluorines and cementitious aluminum at the polymeric powder/white cement interface. These experiments did not yield any CP signal, which suggests that there are no significant interactions taking place. This is supportive of Bentur's steel fibre/concrete interface model [20] since the porous/bulk cement which contains aluminum can be up to 40 μm away from the polymer. The $^{19}F \longrightarrow {}^{27}Al$ CP/MAS NMR experiment probes chemical interactions which occur through space on an angstrom scale. If there is at most a 1 μm duplex film of $Ca(OH)_2$ at the fibre/cement interface the ^{19}F sites of the polymer could not couple with the ^{27}Al sites in the cement. With Bentur's model in mind and working with CP NMR dipolar coupling distances on the angstrom scale, it is therefore not surprising that the NMR data suggest that there are no detectable interactions between ^{19}F in PFA and ^{27}Al in white cement, even if Bentur's model is correct only out to one micron.

^{13}C CP/MAS NMR experiments were employed to determine if there were detectable interactions taking place between polymeric carbons and cementitious protons at the PFA/white cement interface. The experiments were carried out on PFA only, as it is the most likely to interact with the cementitious matrix, as a result of its ether functionality. In contrast, Teflon is assumed to exhibit little to no bonding characteristics with white cement. ^{13}C CP/MAS NMR spectra of a white cement control and PFA/white cement are shown in Figure 6.8. Both spectra have a strong resonance at 168 ppm which is attributed to $CaCO_3$ in the cementitious matrix.

The ^{13}C CP/MAS spectrum of PFA/white cement contains a broad resonance in the range of 110-140 ppm that is not observed in the control sample. To assign this broad resonance, the ^{13}C spectrum for a similar fluoropolymer, Nafion (see Figure 6.9), presented by Chen *et al.* [103] was used. Table 6.1 summarizes the ^{13}C chemical shifts for Nafion and their assignments. Nafion resonances for OCF_2(furthest from backbone), SCF_2, and CF (side chain) would not be present in PFA ^{13}C spectra. Of the remaining possible resonances, CF_3, OCF_2, CF_2, and CF (backbone), all resonate between 108-118 ppm, which falls into the range of the weak broad resonance observed in the ^{13}C CP/MAS NMR spectrum for PFA/white cement. From these results, it is speculated that there is a weak hydrogen bonding interaction occurring between the ether linkage in PFA and the hydroxyl groups in the surrounding cementitious matrix, which gives support to Bentur's interfacial model such that $Ca(OH)_2$ would form near the polymer/cement interface.

Table 6.1: SPE ^{13}C NMR chemical shifts for Nafion as reported by Chen *et al.* [103]

Peak Position (ppm)	Assignment
117.9	CF_3
117.0	OCF_2 (nearest to backbone)
116.7	OCF_2
112.2	SCF_2
111.0	$[CF_2]$
108.0	CF (backbone)
102.9	CF (side-chain)

To investigate further the possibility of PFA/white cement interactions, SPE ^{43}Ca NMR experiments were conducted to determine if the calcium sites, specifically the $Ca(OH)_2$ or CSH sites, were affected by the presence of fluoropolymer powder. Taylor

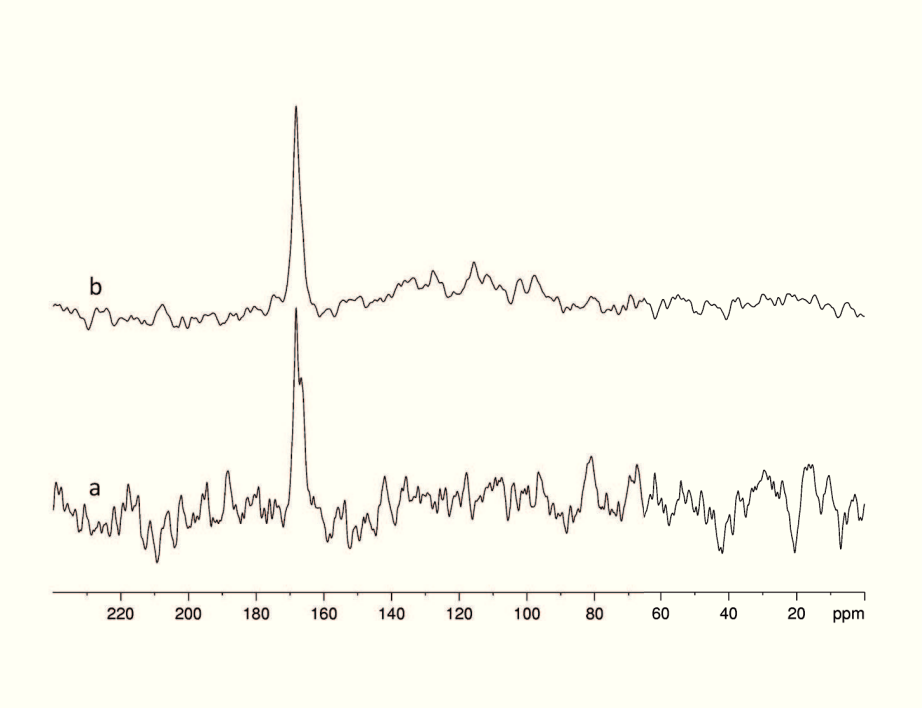

Figure 6.8: ^{13}C CP/MAS NMR spectra of (a) white cement control and (b) PFA/white cement.

and co-workers [14,70,71] describe the structure of CSH as tobermorite or jennite-like (structures introduced in Chapter 1, Section 1.4). Bowers and Kirkpatrick [64] used ^{43}Ca NMR spectroscopy to study the calcium environments of tobermorite, jennite and $Ca(OH)_2$ at a magnetic field strength of 21.1 T. ^{43}Ca NMR resonances were assigned between 0 and −40 ppm (−10 ppm maximum) for tobermorite and between 5 and −60 ppm (−24 ppm maximum). In the Bowers and Kirkpatrick study [64], the resonances of tobermorite and jennite do not overlap and the $Ca(OH)_2$ resonance, between 30 and 70 ppm with a peak maximum of 60 ppm, only partially overlap with jennite. Bryce *et al.* [49] report experimental $CaCO_3$ resonances at 3 to 6 ppm and 0 to −30 ppm (10 ppm centre) for calcite and vaterite, which overlap with the

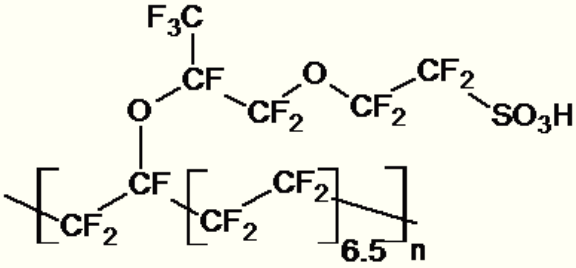

Figure 6.9: Chemical structure of Nafion.

tobermorite spectral region. Figure 6.10 shows the SPE ^{43}Ca NMR spectra of a white cement control, Teflon/white cement, and PFA/white cement. The ^{43}Ca resonances were assigned as $Ca(OH)_2$ (53 ppm), tobermorite (-10 ppm), and jennite (0 to 62 ppm with a peak maximum at 31 ppm) consistent with the literature [49,54,56,60,64,106]. There is no significant increase in intensity observed in the 0 to -30 ppm region of the spectra, indicating that carbonation of the samples is minimal.

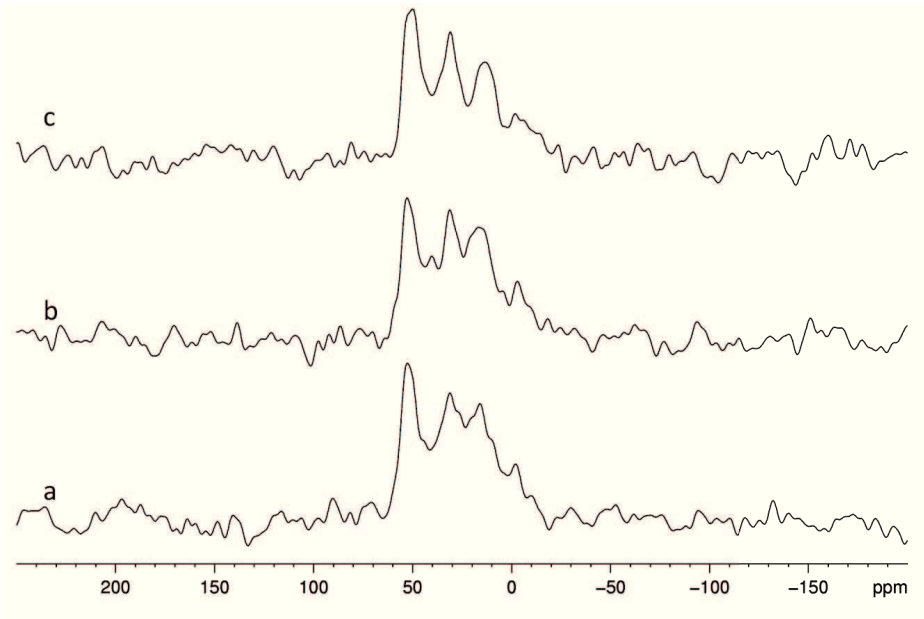

Figure 6.10: SPE ^{43}Ca NMR spectra of (a) white cement control, (b) teflon/white cement, and (c) PFA/white cement.

6.4.2 The Interfacial Transition Zone Surrounding Steel and Polymeric Fibres and White Cement at Long Range

6.4.2.1 Elemental Mapping

The SEM/EDS technique (as introduced in Chapter 2) requires that sample surfaces be polished flat and coated with a conductive material. For porous material, such as cementitious samples, there are many important things to consider prior to sample preparation. Cementitious specimens should be impregnated with epoxy resin to preserve the pore structure during sectioning and polishing procedures. Prior to epoxy impregnation, samples must be dried to avoid incomplete curing of the epoxy resin. There are four typical methods used to dry cementitious samples, namely vacuum drying, freeze drying, solvent exchange and oven drying. Kjellsen *et al.* [107], used the freeze drying technique that first involved freezing the sample in liquid nitrogen then placing it in a cooled chamber under vacuum. This process is fast and minimizes structural damage. The solvent exchange method is very slow, vacuum drying can induce cracking, and oven drying can cause damage to some cement hydrates [76]. Considering these techniques, the freeze drying method was chosen for this study. A low viscosity epoxy resin was used to impregnate the fibre/white cement samples. Sample surfaces are commonly polished using SiC, colloidal silica or diamond paste. To avoid silicon contamination of the cementitious surfaces (as Si is an element of interest in the cement matrix), diamond was chosen for all polishing procedures in this study.

Bentur *et al.* [26] proposed a model of the steel fibre/concrete interface which is characterized by an interfacial transition zone of approximately 40 μm (rich in $Ca(OH)_2$). It is anticipated that if there was indeed a calcium rich area surrounding a steel or polymeric fibre it would be visible in a elemental map of the fibre/cement interface. Elemental maps were recorded of the steel, HDPE/PP, PVA, Nylon 6.6, PVDF, and PEI/white cement interface, viewing approximately 20 μm and 250 μm of the interfacial transition zone, are shown in Figures 6.11, 6.12, 6.13, 6.14, 6.15, and 6.16, respectively.

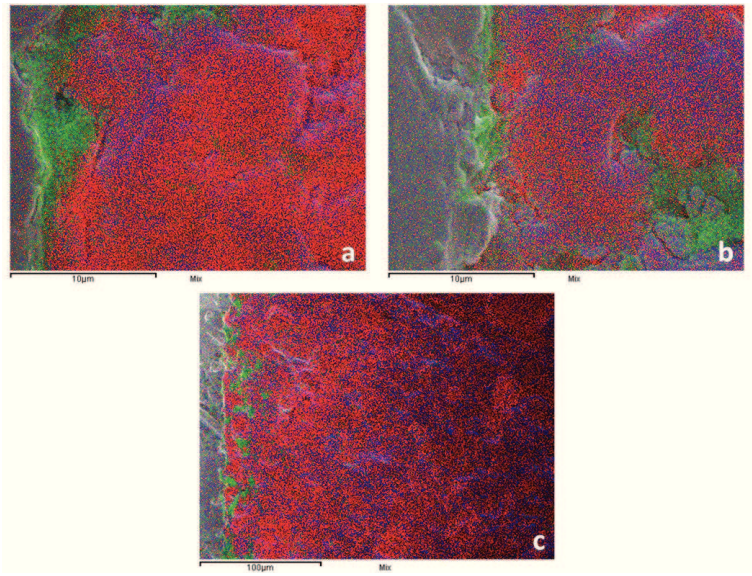

Figure 6.11: SEM/EDS overlaid elemental maps of the steel/white cement interface. The colours red, green, and blue correspond to Ca, C, and O, respectively, where (a) and (b) show approximately 20 μm of the ITZ and (c) shows approximately 250 μm of the ITZ.

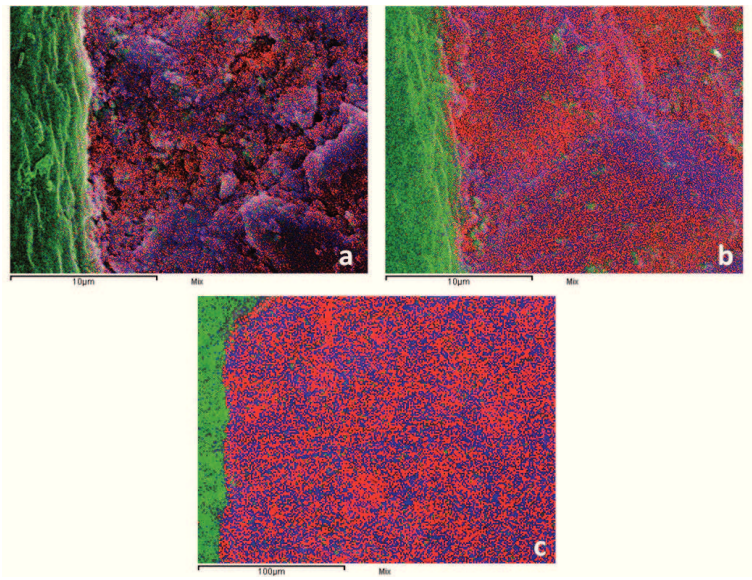

Figure 6.12: SEM/EDS overlaid elemental maps of the HDPE/PP/white cement interface. The colours red, green, and blue correspond to Ca, C, and O, respectively, where (a) and (b) show approximately 20 μm of the ITZ and (c) shows approximately 250 μm of the ITZ.

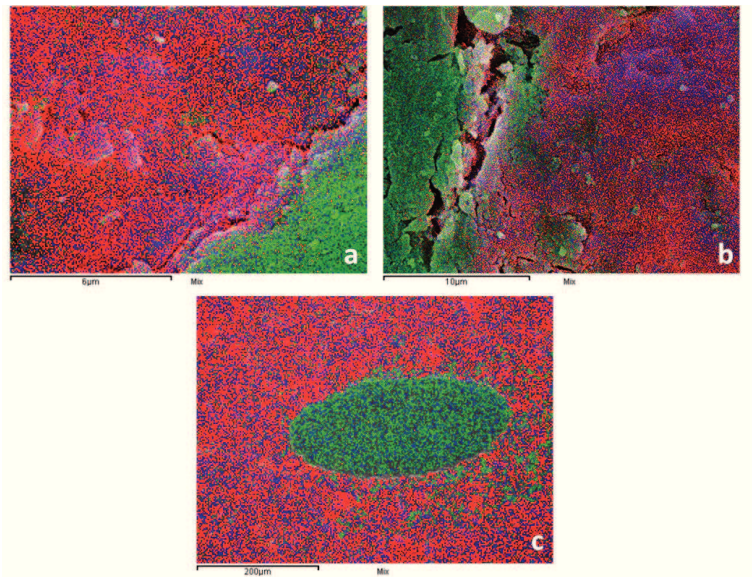

Figure 6.13: SEM/EDS overlaid elemental maps of the PVA/white cement interface. The colours red, green, and blue correspond to Ca, C, and O, respectively, where (a) and (b) show approximately 20 μm of the ITZ and (c) shows approximately 250 μm of the ITZ.

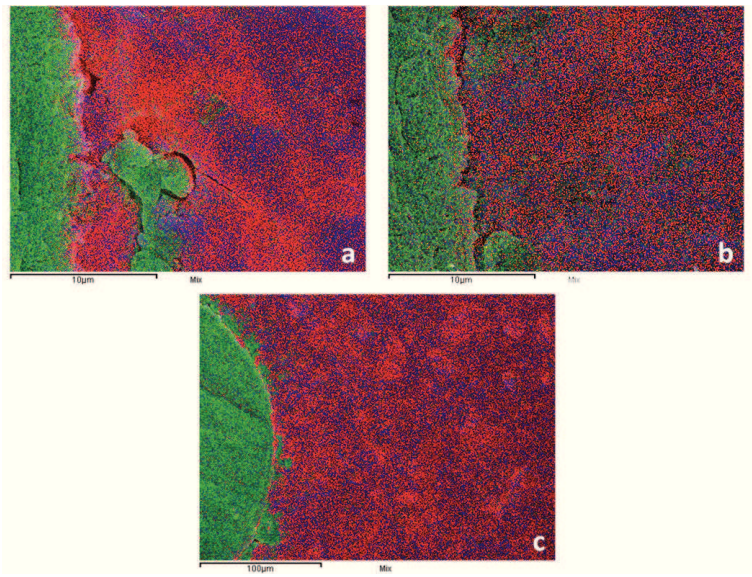

Figure 6.14: SEM/EDS overlaid elemental maps of the Nylon 6.6/white cement interface. The colours red, green, and blue correspond to Ca, C, and O, respectively, where (a) and (b) show approximately 20 μm of the ITZ and (c) shows approximately 250 μm of the ITZ.

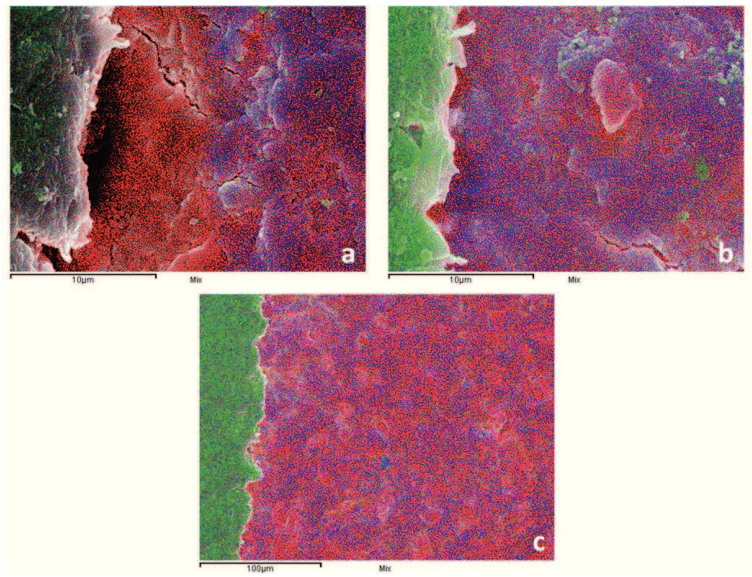

Figure 6.15: SEM/EDS overlaid elemental maps of the PVDF/white cement interface. The colours red, green, and blue correspond to Ca, C, and O, respectively, where (a) and (b) show approximately 20 μm of the ITZ and (c) shows approximately 250 μm of the ITZ.

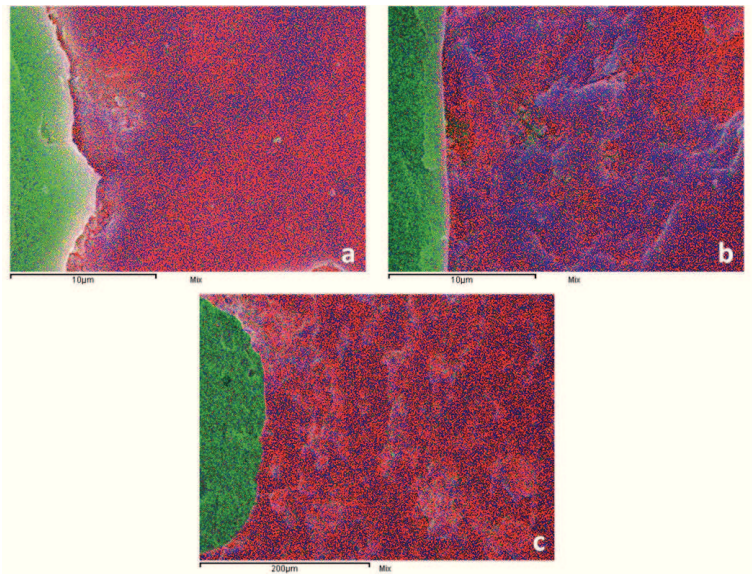

Figure 6.16: SEM/EDS overlaid elemental maps of the PEI/white cement interface. The colours red, green, and blue correspond to Ca, C, and O, respectively, where (a) and (b) show approximately 20 μm of the ITZ and (c) shows approximately 250 μm of the ITZ.

All coloured elemental maps are composed of an overlay of calcium (red), carbon (green), and oxygen (blue) maps. HDPE/PP, PVA, Nylon 6.6, PVDF, and PEI are carbon based fibres and as such all the composite maps picture the fibre in green, with the exception of the steel composite elemental maps in which the fibre is coloured grey. Recalling Bentur's model of the steel fibre concrete interface [26] (introduced in Chapter 1, Section 1.6.2.1), the interfacial transition zone is porous and rich in $Ca(OH)_2$. To begin, the steel fibre/cement interfacial transition zone was compared to Bentur's steel fibre/concrete model. Focusing on Figure 6.11, the steel fibre/white cement interface, large deposits of carbon are observed in direct contact with the steel fibre (see Figure 6.11a and b). On the larger scale (Figure 6.11c), carbon deposits are observed approximately up to 30-40 μm from the fibre surface. The carbon deposits

are representative of the epoxy filled pores in the cementitious matrix. This porous zone surrounding the steel fibre is consistent with Bentur's model which described a porous layer near the fibre concrete interface. It is difficult to determine visually from these images if there is a substantial $Ca(OH)_2$ layer present at the fibre surface as suggested by Bentur *et al.* [26].

For the polymeric fibre/white cement interface composite elemental maps, it is difficult to determine which carbon deposits are attributable to epoxy filled pores or part of the fibre itself. The distribution of calcium does not suggest the presence of a calcium rich layer near the polymeric fibre surface.

6.4.2.2 Point Analysis

To determine the characteristics of the interfacial transition zone as a function of distance from the fibres of interest, spectra at a series of points were acquired, moving away from the fibre surface. From this analysis, the percentage oxide of each element of interest was calculated, based on stoichiometry, for each point. An example of the point map anaylsis grid is shown in Figure 6.17 for the steel fibre/white cement interface.

Using the point analysis data, the Ca/Si ratio was determined for points in the interfacial transition zone between steel, HDPE/PP, PVA, PVDF, PEI, and Nylon 6.6/white cement.

Considering the possible cement hydration products, shown in Table 6.2, the only

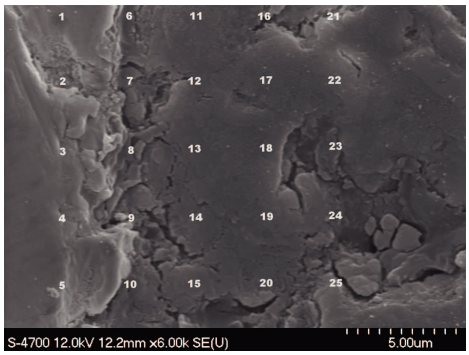

Figure 6.17: Example of a point map grid for elemental analysis of the interfacial transition zone in a steel fibre/white cement composite.

Si containing product is CSH, which is the major cement hydration product. Assuming that all of the SiO_2 reacts to form CSH, which typically has a Ca/Si ratio of 1.5-2.0, the remaining amount of CaO which can form other products can be estimated. With all SiO_2 accounted for, the remaining cement hydration products consist of calcium aluminates, calcium sulfates, and $Ca(OH)_2$. If a high Ca/Si ratio is observed, it follows that there is low silicon content or high calcium content present in the region. It is speculated that in areas of high Ca/Si ratios that the dominating calcium species is $Ca(OH)_2$. Figure 6.18 shows that the Ca/Si ratio near the fibre is high, and, with increasing distance from the fibre, the Ca/Si ratio tends to approach more ideal Ca/Si ratios (shown by black horizontal lines) for CSH. The point analysis method involved the manual selection of mapping points and numerous assumptions to calculate the Ca/Si ratio at various distances from the fibre surface. To reduce the potential error and possible bias, the fibre/white cement interfacial transition zones were also analysed by image analysis in this work (see Section 6.4.2.3).

Table 6.2: Cement hydration products

Chemical Formula
$CaO \cdot SiO_2 \cdot H_2O$
$Ca(OH)_2$
$3\,CaO \cdot Al_2O_3 \cdot 3\,CaSO_4 \cdot 32\,H_2O$
$3\,CaO \cdot Al_2O_3 \cdot CaSO_4 \cdot 12\,H_2O$
$3\,CaO \cdot Al_2O_3 \cdot CaCO_3 \cdot 11\,H_2O$
$4\,CaO \cdot Al_2O_3 \cdot 12\,H_2O$

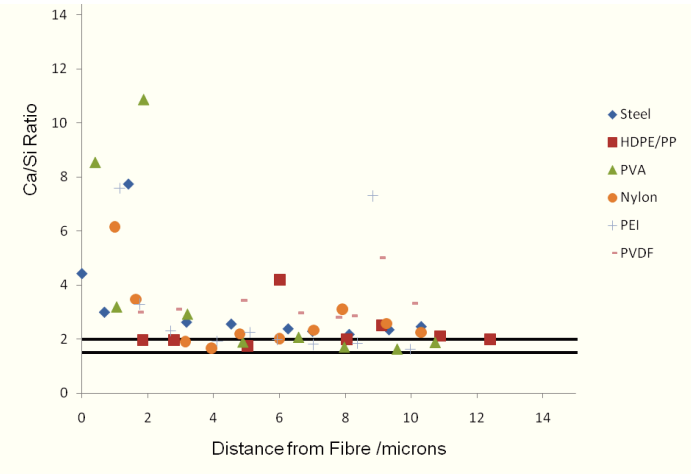

Figure 6.18: Ca/Si ratio *vs.* distance from the fibre edge based upon point analysis data.

6.4.2.3 Image Analysis

The elemental mapping procedure records the distribution of X-ray intensity over a selected region of the sample, thus giving an assessment of the distribution of elements. From this process maps of individual elements over a sample area can be generated. To analyze the elemental data more closely, using the electron micrograph images (see Appendix A), masks were created for each fibre (for an example see Figure 6.19) and were used to determine the fibre edge in each elemental map. Elemental maps of Fe, Ca, Si, Al, O, and C are presented for each fibre type; steel, HDPE/PP, PVA, Nylon

6.6, PVDF, and PEI, in Figures 6.20, 6.21, 6.22, 6.23, 6.24, and 6.25, respectively. In micron sized steps (see Figure 6.26), slices were selected up to 50 microns from the fibre edge and the average pixel intensity was recorded. The average pixel intensity gives an estimate of the amount of a particular element present in a given slice. Following image analysis, the ratio of Ca/Si was calculated and plotted as a function of distance from the fibre surface as shown in Figure 6.27.

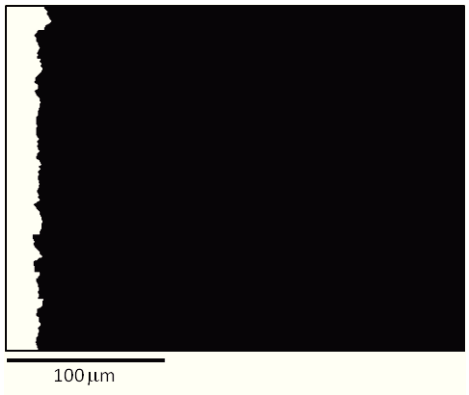

Figure 6.19: Example of a fibre mask created and used for image analysis of SEM/EDS elemental maps where the white space represents a steel fibre and the black space represents the cementitious matrix surrounding the fibre.

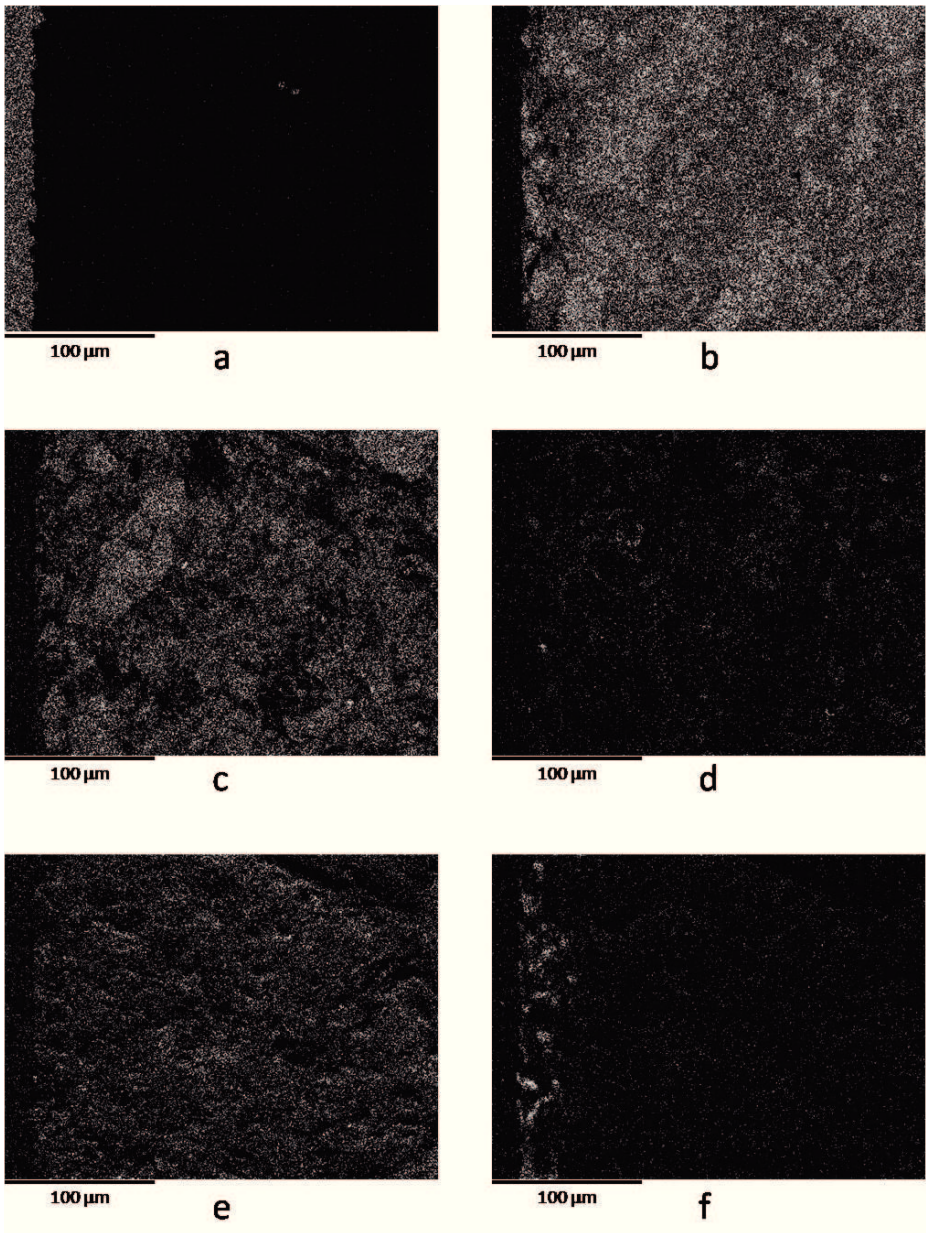

Figure 6.20: SEM/EDS elemental maps of the steel fibre/white cement interface. Letters a-f correspond to Fe, Ca, Si, Al, O, and C.

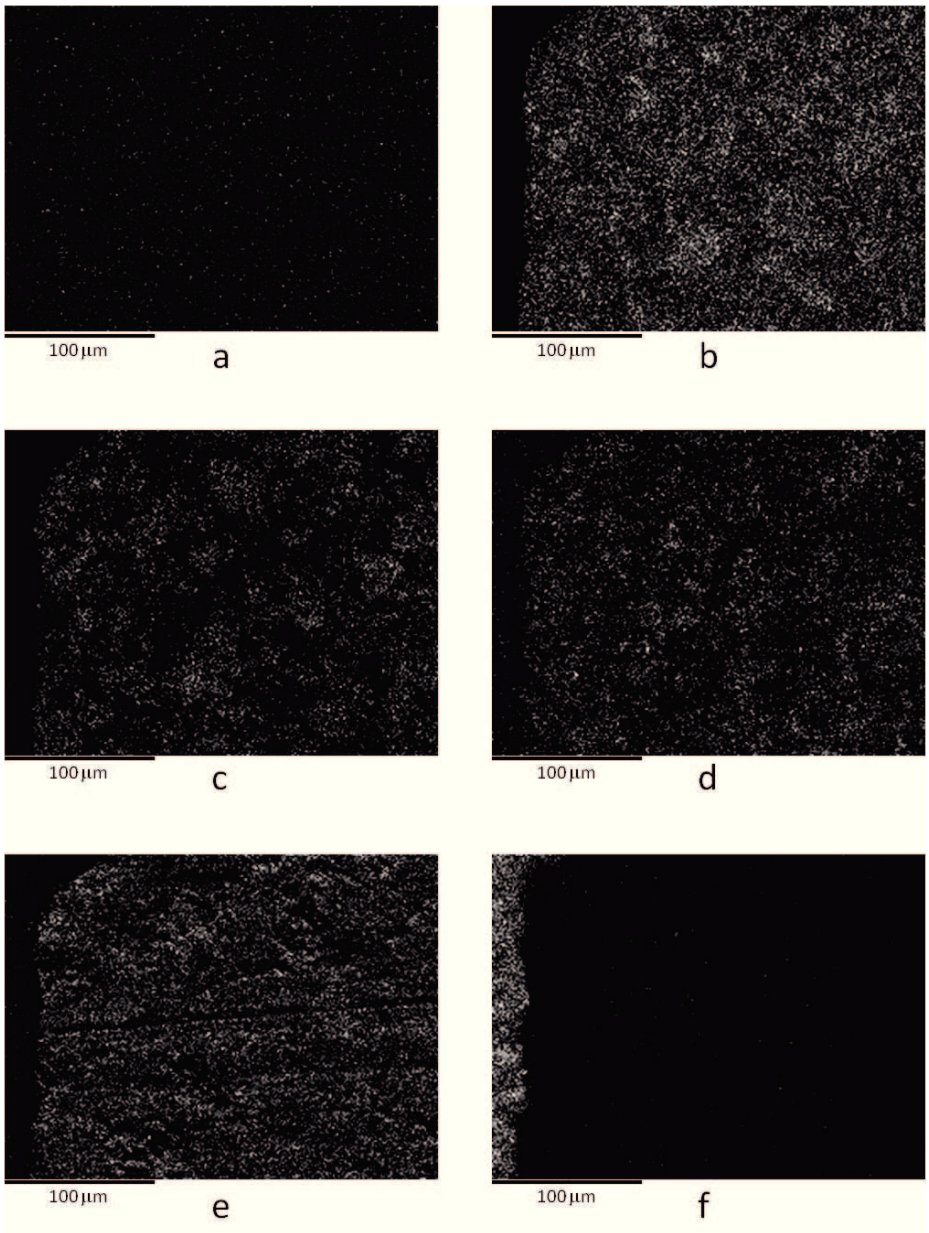

Figure 6.21: SEM/EDS elemental maps of the HDPE/PP fibre/white cement interface. Letters a-f correspond to Fe, Ca, Si, Al, O, and C.

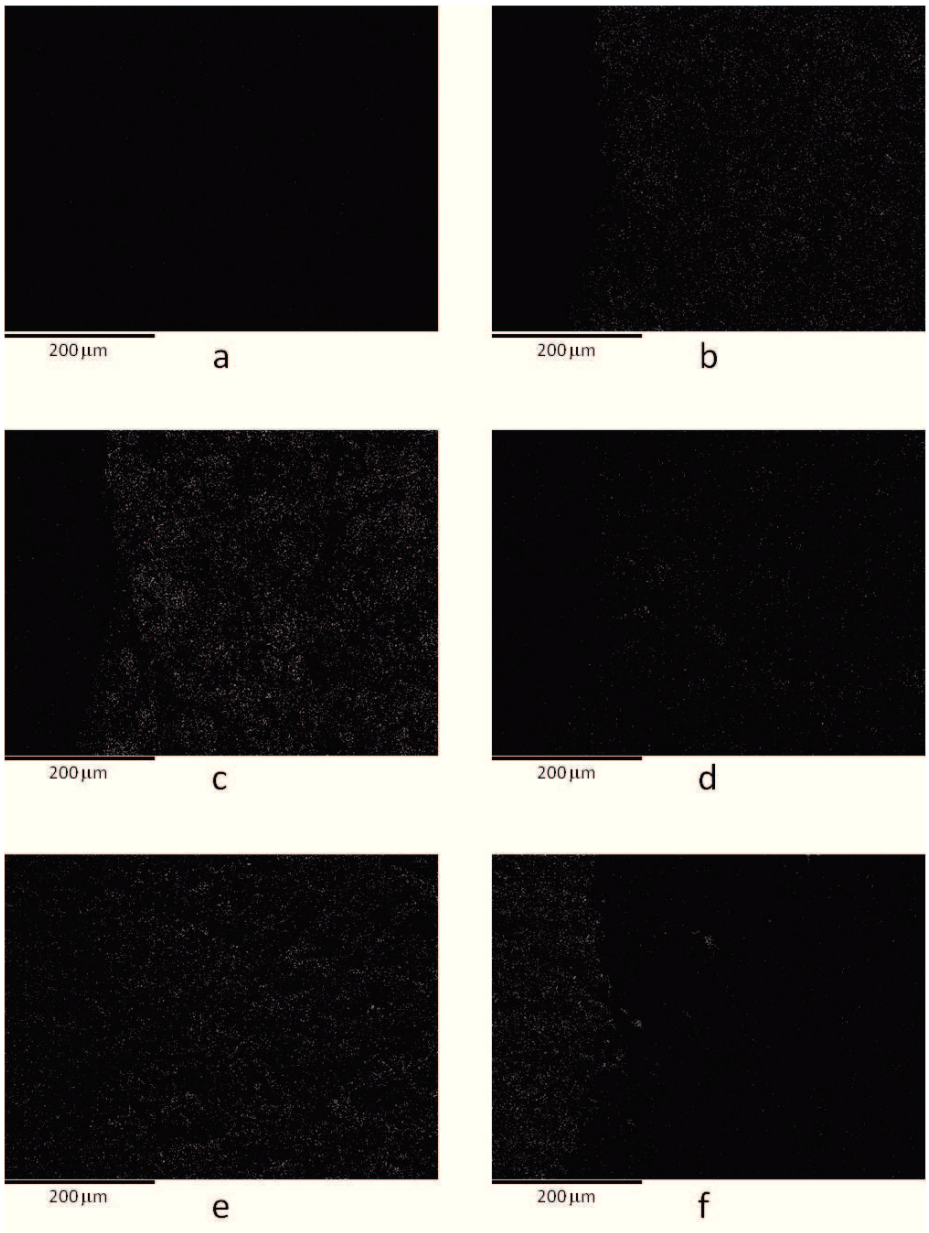

Figure 6.22: SEM/EDS elemental maps of the PVA fibre/white cement interface. Letters a-f correspond to Fe, Ca, Si, Al, O, and C.

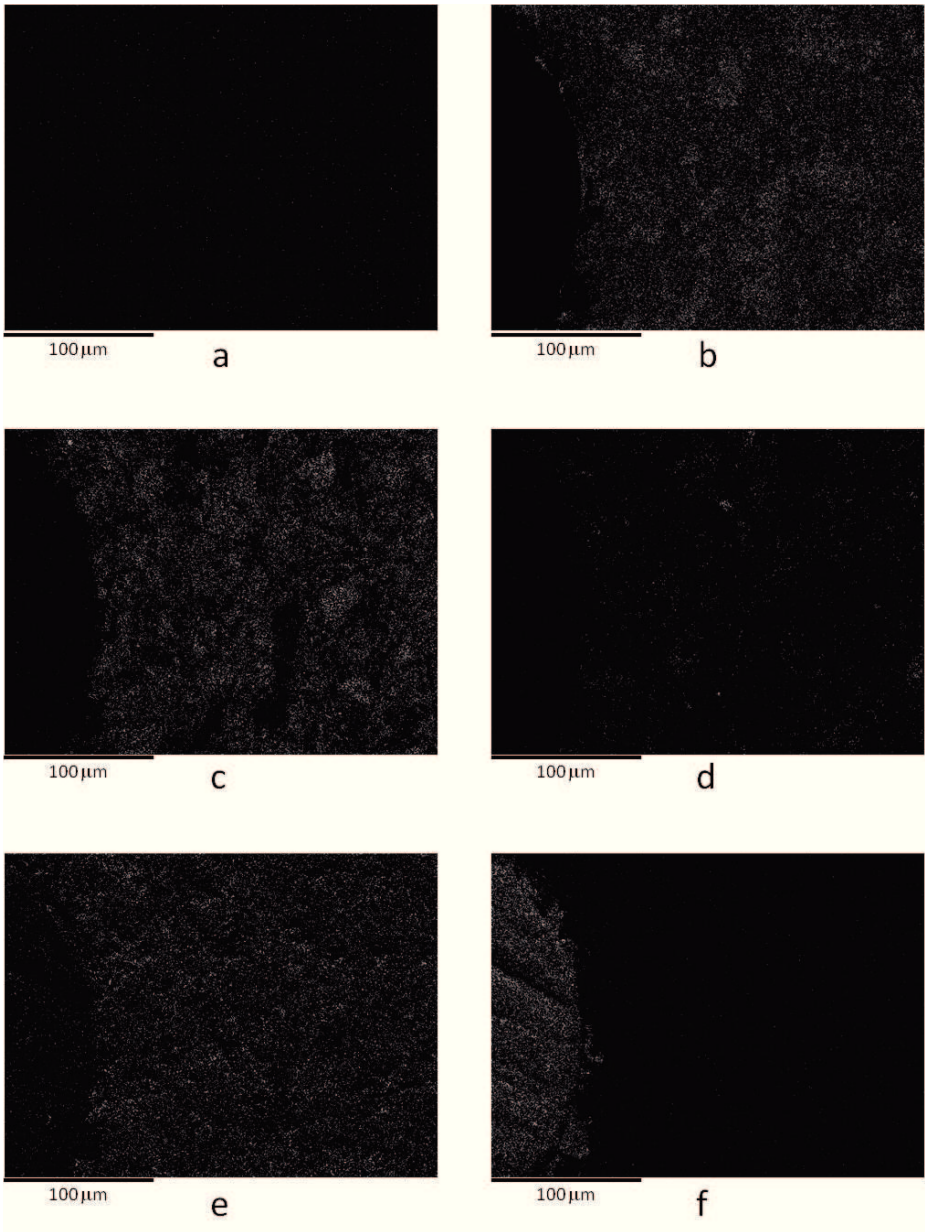

Figure 6.23: SEM/EDS elemental maps of the Nylon 6.6 fibre/white cement interface. Letters a-f correspond to Fe, Ca, Si, Al, O, and C.

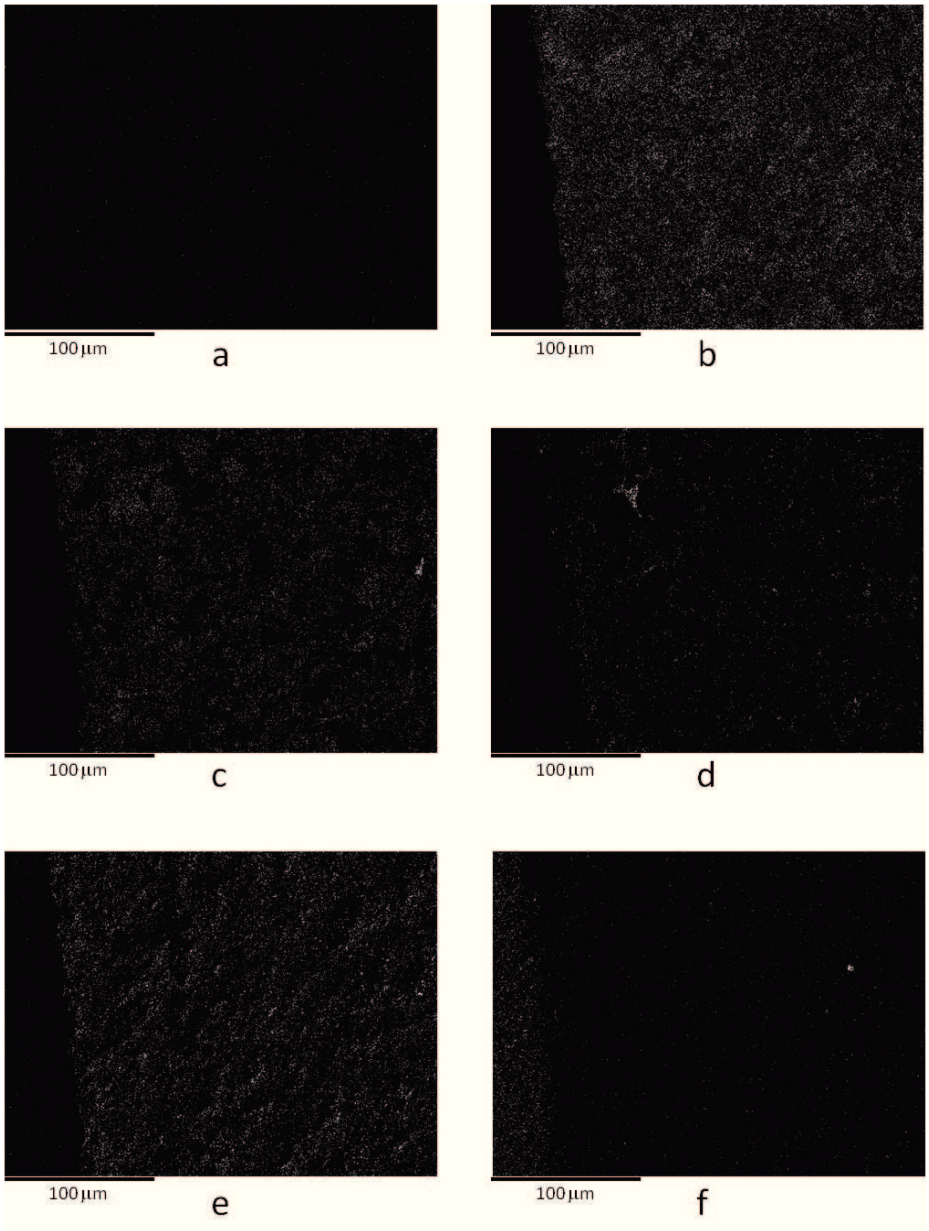

Figure 6.24: SEM/EDS elemental maps of the PVDF fibre/white cement interface. Letters a-f correspond to Fe, Ca, Si, Al, O, and C.

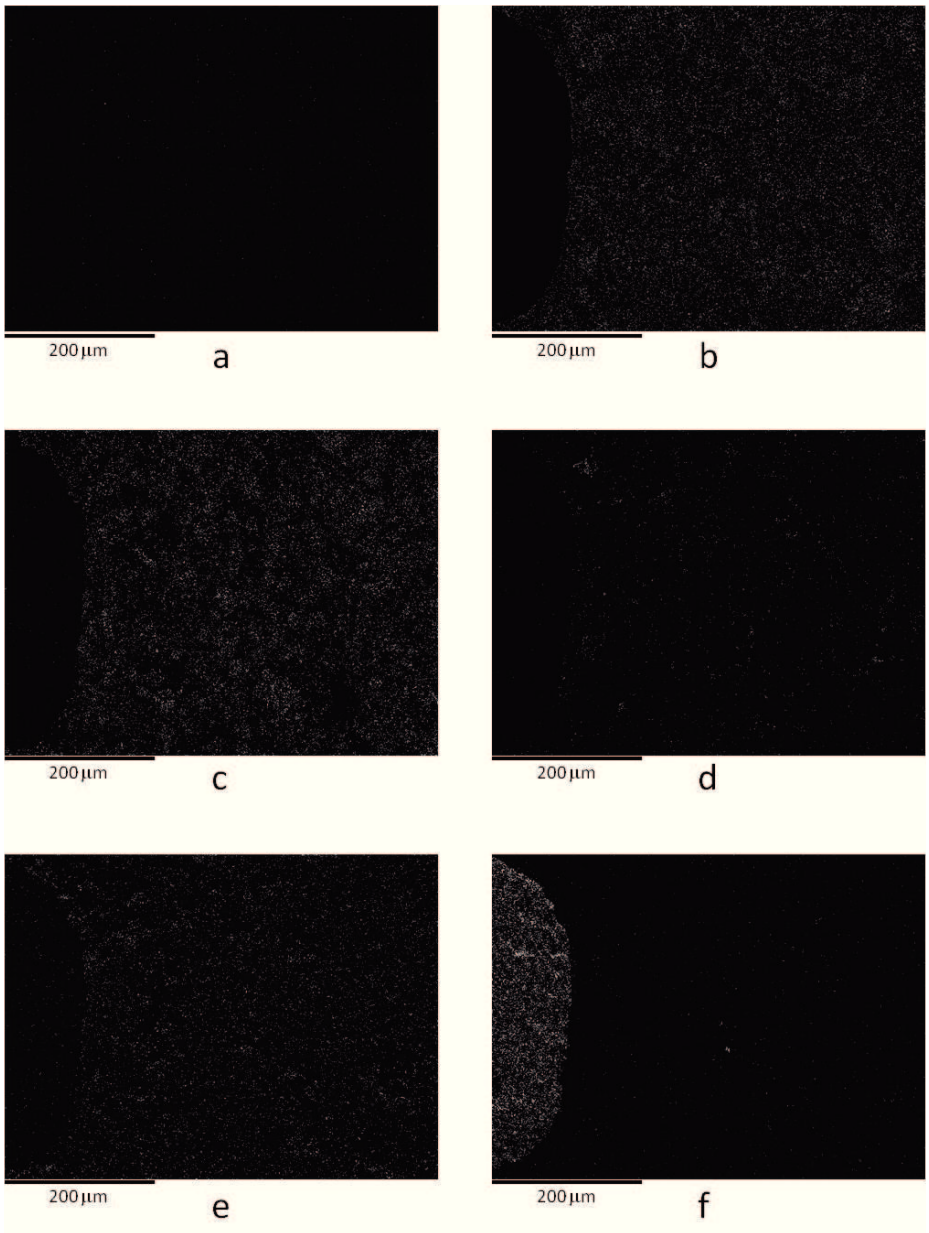

Figure 6.25: SEM/EDS elemental maps of the PEI fibre/white cement interface. Letters a-f correspond to Fe, Ca, Si, Al, O, and C.

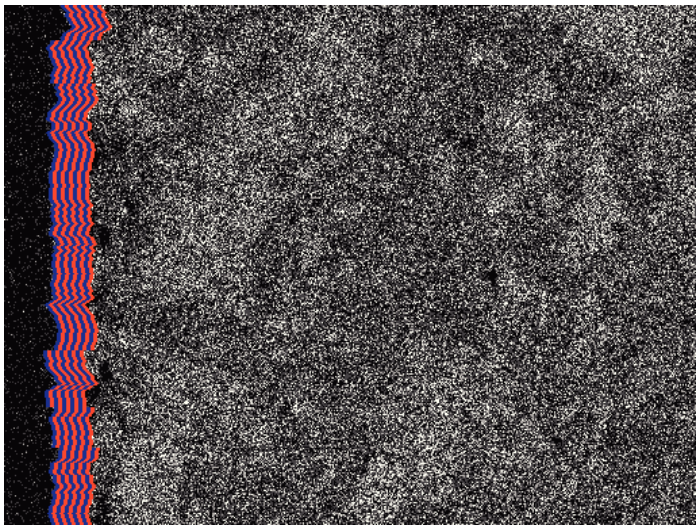

Figure 6.26: Example of micron sized slices used for SEM/EDS image analysis.

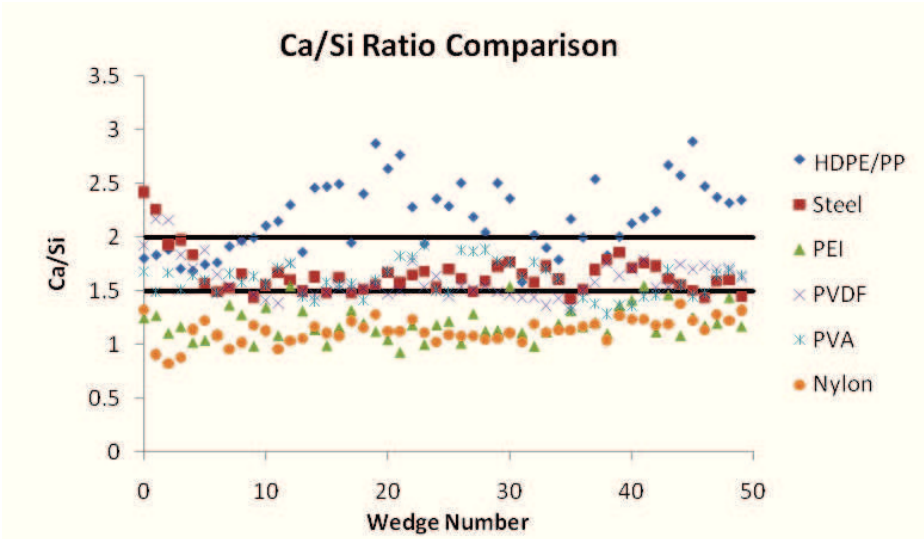

Figure 6.27: Ca/Si ratio *vs.* distance from the fibre edge based upon image analysis results.

The Ca/Si ratio data, determined from image analysis, were compared using the t-test, for cases of PEI *vs.* PVA, PVDF *vs.* Nylon, and Nylon *vs.* PEI, to test if the difference between Ca/Si ratio data that fall below a Ca/Si ratio of 1.5 (shown in Figure 6.27) and those above a Ca/Si ratio of 1.5 is statistically significant. It was found that PVDF has a higher Ca/Si ratio than Nylon (1.61 *vs.* 1.13, t=15.6, p= 1.84×10^{-23}), indicating that the difference in Ca/Si ratios of PVDF and Nylon are statistically significant. Similarly, the difference in Ca/Si ratios of the interfacial transition zone surrounding PEI and PVA are statistically significant. The difference in the zones surrounding PEI and Nylon are also significant at the 0.01 level; however, the effect size is small. The Cohen's d values [108] are 2.61, 3.61, and 0.51 for cases of PEI *vs.* PVA, PVDF *vs.* Nylon, and Nylon *vs.* PEI, respectively. The statistical t-test results are given in Table 6.3.

Table 6.3: t-test comparisons between PEI, PVA, Nylon, and PVDF SEM/EDS image analysis data

Comparison	Mean	t-statistic	p-value
PEI *vs.* PVA	1.20 *vs.* 1.60	12.9	3.72×10^{-23}
PVDF *vs.* Nylon	1.61 *vs.* 1.13	15.6	1.84×10^{-26}
Nylon *vs.* PEI	1.13 *vs.* 1.20	2.51	0.007

The typical Ca/Si ratio in CSH (major product of cement hydration) falls between 1.5-2.0. Taylor [14] postulated that the structure of CSH is similar to that of tobermorite and jennite (for chemical structures refer to Chapter 1). The Ca/Si ratio in tobermorite is less than 1.2 and in jennite, greater than 1.2. Keeping these ratios in mind, the structure of the interfacial transition zone can be determined. In

Figure 6.27, there are three groups of possible structures observed that could surround steel and polymeric fibres. The Ca/Si ratio of the interfacial transition zone surrounding PEI and Nylon 6.6 fibres falls below the typical CSH Ca/Si ratio of 1.2. The slope of these data is essentially zero and as there are no values of Ca/Si ratio above 2, it is speculated that the CSH structure surrounding PEI and Nylon 6.6 fibres is tobermorite-like. Although based on chemical structure of the fibres it was anticipated that PEI and Nylon 6.6 would produce chemical bonding between the fibre and the matrix, it has been shown previously in the literature that Nylon 6.6 exhibits poor chemical bond with cementitious matrices [28,29]. PEI contains similar functionalities as Nylon 6.6 and was shown (in Chapter 4) to react, albeit minimally, with the cementitious environment. Following hydrolysis in the cementitious matrix, PEI's structure contains an amine functional group like that of Nylon 6.6. Based on the Ca/Si ratio surrounding PEI and Nylon 6.6 fibres, the similar functionalities in the fibre structures and the knowledge of Nylon 6.6's poor chemical bonding with cementitious matrices, it is suspected that PEI fibres would not exhibit substantial chemical bonding with cement.

In Bentur's model (discussed in Chapter 1), it was reported that a large $Ca(OH)_2$ layer (30 μm) was present surrounding a steel fibre. From the SEM/EDS image analysis data, it was observed that the Ca/Si ratio in the steel fibre/white cement interfacial transition zone was generally between 1.5-2.0. Near the interface however, within the first few microns, the Ca/Si ratio was higher which could indicate the presence of $Ca(OH)_2$. From these observations, it is thought that Bentur's model

of the steel fibre/concrete interface is generally correct, however, in this work the $Ca(OH)_2$ layer is estimated to be only a few microns in thickness.

Considering PVA, which is hydrophilic and is known to bond strongly with cementitious matrices [34, 35], the data fall in the typical range for CSH and it is thought that the CSH surrounding the PVA fibre is jennite-like. Interestingly, the data for PVDF (hydrophobic) also fall in the same range as the data for PVA (hydrophilic). It is possible that PVA and PVDF share a similar ionic bonding mechanism with the cementitous matrix. When PVA is placed in a basic environment, like that of cement, the hydroxyl proton can be removed allowing the oxygen to interact with near by calcium in the cement as shown in Figure 6.28. PVDF, when drawn into fibre, takes on a polarized β-form (shown in Chapter 5, Figure 5.2), in which the partially positive region could interact with the oxygens in the cement and the partially negative region could interact with the calcium species. These results indicate that PVDF could exhibit similar bonding character with cementitious matrices as PVA.

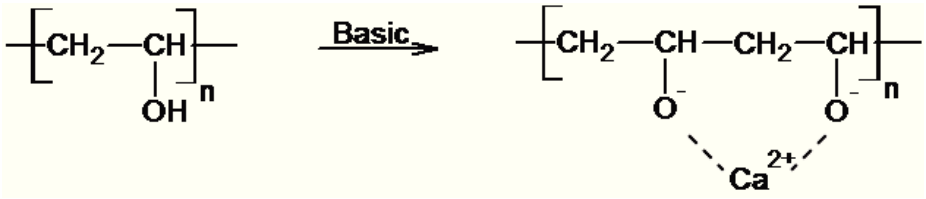

Figure 6.28: Potential bonding between PVA and cementitious matrices.

The interfacial transition zone between the HDPE/PP fibre and white cement was also examined. The data for this fibre are not surprising, as the fibre is hydrophobic and its bonding character is solely mechanical, due to the fibre's ability to fibrillate

during the mixing process. The Ca/Si ratio, up to approximately 5 μm from the fibre surface, is within typical values for CSH, however, beyond this distance from the fibre, the majority of the data are above a Ca/Si ratio of 2.0. A possible explanation for this result is that the water in the cementitious matrix was repelled by the hydrophobic nature of the fibre, creating a small region near the fibre with typical Ca/Si ratios which is jennite-like and a larger region which contained more water, which increased the probability of $Ca(OH)_2$ formation.

6.5 Summary

In this study, the interfacial transition zone was studied at short range via NMR spectroscopy between fluoropolymer powder and white cement and at long range via SEM/EDS between steel/polymeric fibres and white cement. The interfacial interactions between PFA and white cement were isolated by ^{13}C CP/MAS NMR spectroscopy. The ^{13}C CP/MAS NMR spectra of PFA/white cement, when compared to the white cement control spectrum, suggest that there is a weak chemical bond between the ether functional group of PFA and the cementitious matrix, likely hydrogen bonding. The ^{27}Al and ^{19}F NMR experiments show that there is little interaction between the polymer ^{19}F sites and the cementitious ^{27}Al, which is supportive of Bentur's model in which any ^{27}Al sites would be far from the interface, too far to be observed via cross-polarization techiniques. It is speculated that the presence of hydrophobic perfluorinated materials in cementitious matrices could cause localized regions around a fibre, for example, to have a high water to cement ratio. The high water to cement

ratio would create a more porous region that could cause the interfacial transition zone surrounding a fibre of this type to fail.

SEM/EDS elemental mapping was used to investigate the structures of the fibre/white cement interfacial transition zone for various fibres. Two methods were used; point analysis and image analysis. Point analysis was much more time consuming and involved more assumptions during analysis, thus in the future, image analysis would be the method of choice when using the SEM/EDS technique. It was found that for the steel fibre case that the transition zone possibly contains a $Ca(OH)_2$ layer, but it is estimated to be at most a few microns thick. The data indicate that the interfacial transition zone between a fibre/white cement is affected by the chemistry of the fibre itself. It was found that PVDF could potentially bond well with cementitious matrices similar to PVA. PEI is thought to have poor bond with the matrix as does Nylon 6.6.

Chapter 7

Conclusion

7.1 General Conclusions

The purpose of this dissertaion was to explore the chemical interactions between polymeric powder/fibre and white cement. It was hypothesized that the chemical interactions between polymeric fibres and concrete create additional bonding. To test this hypothesis experimentally, the chemical degradation of EVA, PVDF, and PEI powder in white cement and the chemical interactions between steel, HDPE/PP, PVA, PEI, PVDF, and Nylon 6.6 fibres in white cement were investigated.

The hydrolysis of an EVA admixture in white cement was monitored using NMR spectroscopy. It was found that the EVA hydration kinetics are pseudo-second order until 32 days of cement hydration. Following 32 days of cement hydration, the hydration kinetics of EVA deviate from the pseduo-second order model and it is speculated that a diffusion controlled mechanism is adopted. ^{43}Ca and ^{29}Si NMR was used to study the effect of EVA additive on the cementitious calcium and silicon species. From the ^{43}Ca NMR spectra, it was not apparent that there was a change in the structure of the cementitious calcium species as a result of the addition of EVA. It is speculated, based on the ^{29}Si NMR spectra, that the hydroxyl groups in hydrolyzed

EVA interact via hydrogen bonding with the hydroxyl groups in the silicate chains of CSH creating additional bond between EVA and cement.

In an attempt to isolate the fibre white cement interface using NMR spectroscopy, fluoropolymer powders were chosen to create heteronuclear pairs in which one nucleus was exclusively associated with the polymer and the other with the cement. It was found that there is little interaction between white cement and Teflon or PFA. There is possibly a weak chemical bonding interaction observed (as shown with ^{13}C CP NMR) between PFA and white cement due to the presence of PFA's ether functionality.

The potential polymer candidates for fibre production chosen by Trottier [13] were examined in powdered and fibre form. It was found, using NMR spectroscopy, that PEI reacted chemically in the cementitious environment via a hydrolysis pathway. Through SEM/EDS studies it was shown that the interfacial transition zone surrounding PEI is similar to that of Nylon 6.6, which is known to exhibit poor bond with cementitious matrices. The results, coupled with the fact that Trottier [13] was unable to draw PEI fibres due to temperature restrictions on the melt extrusion line, and the high cost of PEI resin, indicate that this material is likely to make a poor concrete reinforcing fibre, despite its high tensile strength and good thermal properties.

PVDF was observed to react chemically with cement when in powdered form, producing a brown composite. Through a variety of testing methods (NMR, IR, and UV-Vis spectroscopies) it was concluded that the PVDF backbone had undergone conjugation which gave rise to the brown colour. It is uncertain if this reaction would

take place to a great enough extent to be detrimental to a PVDF fibre. Through SEM/EDS analysis it was found that the β-PVDF fibre induced an interfacial transition zone similar to that surrounding PVA fibre, which is known to bond strongly with concrete. These results indicate that PVDF or PVDF containing blended fibres could potentially create a chemical bond and an interfacial transition zone like that of strongly bonding PVA, but the bond could be tailored to allow for slow pull-out from the matrix rather than fracture which typically occurs with PVA.

7.2 Recommendations and Future Directions

Based upon the results of the EVA study, it was recommended to project collaborators to incorporate EVA into fibres for usage in fibre reinforced concrete applications, either as a blended component (*e.g.*, PP/EVA and HDPE/PP/EVA, similar to the blended materials studied by [109–111]) or as a surface coating. The inclusion of EVA is speculated to add additional chemical bond between the fibre and cementitious matrix via hydrogen bonding. Fibres containing EVA as a blended component have been successfully extruded and preliminary mechanical testing indicates that there is an increase in bond as compared to similar fibres without an EVA component. In the future, further investigations into the kinetics of EVA hydrolysis in cement after 32 days of hydration should be carried out to determine the diffusion controlled model as well as to gain insight into how EVA will behave in cementitious matrices in the long term (periods of years). More detailed mechanical testing and long term studies are required to confirm EVA's capability of increasing bond strength between a

blended fibre and cementitious matrices. This testing is currently underway in the Department of Civil and Resource Engineering at Dalhousie University under the supervision of Dr. Dean Forgeron.

Results of this dissertation have shown that PVDF is a promising material for concrete reinforcement. Based upon the chemical bonding potential of PVDF with cementitious matrices shown in this work (discussed in Chapter 5), PVDF blended fibres have been extruded. PVDF fibres and PVDF blended fibres should be mechanically tested in cementitious environments to determine its toughening capabilities and long term testing on the fibres themselves should be carried out to determine if backbone conjugation of the fibre surface would potentially become detrimental to the fibre's intrinsic properties. Preliminary mechanical testing data indicate that there could be an increase in bond between PVDF and the cementitious matrix. Further mechanical and long term testing is currently being carried out under the supervision of Dr. Dean Forgeron.

Further study of the structure of the interfacial transition zone surrounding polymeric materials in white cement is required to confirm if different fibre chemistries indeed induce changes in the CSH structure of the interfacial transition zone. Raman spectroscopic mapping techniques are currently being explored as a suitable method to examine the structure of CSH surrounding steel, HDPE/PP, PEI, PVDF, and Nylon 6.6 fibres in white cement as a function of distance from the fibre surface. Samples of synthetic tobermorite, natural tobermorite, and jennite will be used as

controls to determine if the structure of CSH is affected locally by the presence of different polymeric fibres (to create an interfacial transition zone which is more jennite or tobermorite-like) as it is speculated that the local CSH structure surrounding the fibres, coupled with the possible chemical bonding between a fibre and cementitious matrix, ultimately affect the overall bond between a fibre and concrete.

The studies presented in this dissertation involved a select few polymers (HDPE/PP, PVDF, PEI, EVA, PFA, Teflon, and Nylon 6.6) and white cement, with cement hydration times of 84 days or less. Future work on the chemical interactions between polymeric fibres and concrete could expand on the selection of fibres as well as the types of cements used and studies could be carried out over much longer time scales (*e.g.*, years). Eventually, it would be interesting to move from the model systems (cement and polymer powder/fibres) presented in this work to more complex concrete composites.

References

[1] M. F. Ashby, Materials and the Environment: Eco-Informed Material Choice, Elsevier, New York, 2009.

[2] M. Murphy, Occupational health - asbestos is biggest killer, Chemistry & Industry 21 (2007) 5.

[3] S. A. S. Akers, G. G. Garrett, Fibre-matrix interface effects in asbestos-cement composites, Journal of Materials Science 18 (7) (1983) 2200–2208.

[4] A. Bismarck, E. Schulz, Adhesion and friction behavior between fluorinated carbon fibers and poly(vinylidene fluoride), Journal of Materials Science 38 (24) (2003) 4965–4972.

[5] Z. Lin, T. Kanda, V. C. Li, On interface property characterization and performance of fiber reinforced cementitious composites, Concrete Science and Engineering 1 (3) (1999) 173–184.

[6] J. A. Nairn, Analytical fracture mechanics analysis of the pull-out test including the effects of friction and thermal stresses, Advanced Composite Letters 9 (6) (2000) 373–383.

[7] J. A. Nairn, C.-H. Liu, D. A. Mendels, S. Zhandarov, Fracture mechanics analysis of the single-fiber pull-out test and the microbond test including the effects of friction and thermal stresses, in: Proceedings of the 16th Annual Technical Conference, American Society for Composites, Blacksburg VA, 2001.

[8] K. Tanaka, K. Minoshima, H. Yamada, Measurement of the fiber stress distribution during pull-out test by means of micro-Raman spectroscopy and FEM analysis, WIT Transactions on the Built Environment 85 (2006) 131–139.

[9] S. Zhandarov, E. Mäder, Characterization of fiber/matrix interface strength: Applicability of different tests, approaches and parameters, Composites Science and Technology 65 (1) (2005) 149–160.

[10] S. Diamond, S. Mindess, F. P. Glasser, L. R. Roberts, J. P. Skalny, L. D. Wakeley (Eds.), Microstructure of Cement-Based Systems/Bonding and Interfaces in Cementitious Materials, Vol. 370, Materials Research Society, 1995.

[11] S. Mindess, S. P. Shah (Eds.), Bonding in Cementitious Composites, Vol. 114, Materials Research Society, 1988.

[12] O. Buyukozturk, M. Wecharatana (Eds.), Interface Fracture and Bond, American Concrete Institute, Detriot, Michigan, 1995.

[13] A. M. Trottier, Development and optimization of synthetic fibres for reinforcement of concrete, Master's thesis, Dalhousie University, Halifax, Nova Scotia, Canada (June 2009).

[14] H. W. F. Taylor, Cement Chemistry, 2nd Edition, Thomas Telford, London, 1997.

[15] S. H. Kosmatka, B. Kerkhoff, W. C. Panarese., Chapter 2: Portland, blended, and other hydraulic cements, in: Design and Control of Concrete Mixtures, 7th Edition, Portland Cement Association, 2002.

[16] P. C. Hewlett, Lea's Chemistry of Cement and Concrete, Arnold, London, 1998.

[17] D. C. MacLaren, M. A. White, Cement: Its chemistry and properties, Journal of Chemical Education 80 (6) (2003) 623–635.

[18] E. G. Nawy, Reinforced Concrete: A fundametal approach, Prentice Hall, New Jersey, 2003.

[19] ASTM Dictionary of Engineering Science and Technology, 10th Edition, ASTM International, 2005.

[20] A. Bentur, S. Mindess, Fibre Reinforced Cementitious Composites, Elsevier Science Publishers Ltd, New York, 1990.

[21] R. Dorf, Handbook of Engineering Tables, CRC Press, Boca Raton, 2004.

[22] Fiber Reinforced Concrete Properties and Applications, American Concrete Institute, 1987.

[23] L. Disney, Steel Reinforcement, Concrete Series, Concrete Publications Limited, London, 1954.

[24] J.-F. Trottier, M. Mahoney, Fiber reinforced building materials, US Patent 6,423,134 (July 2002).

[25] J. P. Newhook, A. A. Mufti, A reinforcing steel-free concrete deck slab for the Salmon River bridge, Concrete International 18 (6) (1996) 30–34.

[26] A. Bentur, S. Diamond, S. Mindess, Cracking processes in steel fiber reinforced cement paste, Cement and Concrete Research 15 (2) (1985) 331–342.

[27] J. Aveston, G. Cooper, A. Kelly, in: The Properties of Fibre Composites, Conference Proceedings of the National Physical Laboratory, Science and Technology Press, UK, 1971.

[28] P. N. Balaguru, S. P. Shah, Fiber-Reinforced Cement Composites, McGraw-Hill, Inc, New York, 1992.

[29] Y. Wang, S. Backer, V. C. Li, An experimental study of synthetic fibre reinforced cementitious composites, Journal of Materials Science 22 (12) (1987) 4281–4291.

[30] C. Redon, V. C. Li, C. Wu, H. Hoshiro, T. Saito, A. Ogawa, Measuring and modifying interface properties of PVA fibers in ECC matrix, Journal of Materials in Civil Engineering 13 (6) (2001) 399–406.

[31] A. Majumdar, Fibre Reinforced Cement and Concrete, RILEM Symposium, 1975, Ch. Properties of fibre cement composites.

[32] D. A. Silva, A. M. Betioli, P. J. P. Gleize, H. R. Roman, L. A. Gómez, J. L. D. Ribeiro, Degradation of recycled PET fibers in Portland cement-based materials, Cement and Concrete Research 35 (9) (2005) 1741–1746.

[33] ACI Committee 544, ACI Manual of Concrete Practice, American Concrete Institute, Detriot, 1986.

[34] J. Hikasa, T. Genba, Replacement for asbestos in reinforced cement products-'Kuralon' PVA fibres, properties, structure., International Man-Made Fibres Congress, Austrailian Chemical Institute, 1986.

[35] Z. Zhijiang, C. Y. Tian, High tenacity PVA fibres: a suitable alternative for asbestos, International Man-Made Fibres Congress, Austrailian Chemical Institute, 1986.

[36] J. F. Trottier, M. Mahoney, Innovative synthetic fibers, Concrete International 23 (6) (2001) 23–28.

[37] S. Burke, M. B. Macklin, K. A. Rieder, J.-F. Trottier, Three-dimensional twisted fibers and processes for making same, US Patent 6,340,522 (January 2002).

[38] S. R. Hartmann, E. L. Hahn, Nuclear double resonance in the rotating frame, Physical Review 128 (5) (1962) 2042–2053.

[39] M. J. Duer, Introduction to Solid-State NMR Spectroscopy, Blackwell Publishing Ltd., 2004.

[40] K. J. D. MacKenzie, M. E. Smith, Multinuclear Solid-State NMR of Inorganic Materials, Pergamon Materials Series, Pergamon, 2002.

[41] J. I. Goldstein, D. E. Newbury, D. C. Joy, C. E. Lyman, P. Echlin, E. Lifshin, L. Sawyer, J. R. Michael, Scanning Electron Microscopy and X-Ray Microanalysis, 3rd Edition, Springer, 2003.

[42] L. C. Sawyer, D. T. Grubb, G. F. Meyers, Polymer Microscopy, 3rd Edition, Springer, New York, 2008.

[43] S. L. Flegler, J. W. Heckman, K. L. Klomparens, Scanning and Transmission Electron Microscopy: An Introduction, W. H. Freeman and Company, 1993.

[44] V. S. Ramachandran, Concrete Admixtures Handbook - Properties, Science, and Technology, 2nd Edition, William Andrew Publishing, 1995.

[45] D. A. Silva, H. R. Roman, P. J. P. Gleize, Evidences of chemical interaction between EVA and hydrating portland cement, Cement and Concrete Research 32 (9) (2002) 1383–1390.

[46] J. Rottstegge, M. Arnold, L. Herschke, G. Glasser, M. Wilhelm, H. W. Spiess, W. D. Hergeth, Solid state NMR and LVSEM studies on the hardening of latex modified tile mortar systems, Cement and Concrete Research 35 (12) (2005) 2233–2243.

[47] A. M. Betioli, J. H. Filho, M. A. Cincotto, P. J. P. Gleize, R. G. Pileggi, Chemical interaction between EVA and Portland cement hydration at early-age, Construction and Building Materials 23 (11) (2009) 3332–3336.

[48] A. A. P. Mansur, O. L. do Nascimento, H. S. Mansur, Physico-chemical characterization of EVA-modified mortar and porcelain tiles interfaces, Cement and Concrete Research 39 (12) (2009) 1199–1208.

[49] D. L. Bryce, E. B. Bultz, D. Aebi, Calcium-43 chemical shift tensors as probes of calcium binding environments: Insight into the structure of the vaterite CaCO polymorph by Ca solid-state NMR spectroscopy, Journal of the American Chemical Society 130 (29) (2008) 9282–9292.

[50] A. A. P. Mansur, O. L. do Nascimento, W. L. Vasconcelos, H. S. Mansur, Chemical functionalization of ceramic tile surfaces by silane coupling agents: Polymer modified mortar adhesion mechanism implications, Materials Research 11 (3) (2008) 293–302.

[51] P. Sykes, A Guidebook to Mechanism in Organic Chemistry, 4th Edition, Longman Group Ltd., London, 1975.

[52] M. E. Smith, Recent progress in solid-state NMR of low-γ nuclei, Annual Reports on NMR Spectroscopy 43 (2001) 121–175.

[53] R. G. Bryant, S. Ganapathy, S. D. Kennedy, High-resolution calcium-43 NMR in solids, Journal of Magnetic Resonance 72 (3) (1987) 376–378.

[54] R. Dupree, A. Howes, S. C. Kohn, Natural abundance solid state ^{43}Ca NMR, Chemical Physics Letters 276 (5-6) (1997) 399–404.

[55] H. Zanni, R. Rassem-Bertolo, S. Masse, L. Fernandez, P. Nieto, B. Bresson, A spectroscopic NMR investigation of the calcium silicate hydrates present in cement and concrete, Magnetic Resonance Imaging 14 (7/8) (1996) 827–831.

[56] P. Nieto, R. Dron, R. Thouvenot, H. Zanni, F. Brivot, Study by ^{43}Ca NMR spectroscopy of the sol-gel transformation of the calcium-silicate complex, Comptes Rendus de l'Académie des Sciences, Série II B: Mécanique, Physique, Chimie, Astronomie. 320 (9) (1995) 485–488.

[57] S. Marchand, A. Trokiner, A. Yakubovsky, A. Knizhnik, Y. Eckstein, Doping dependence of the ^{43}Ca Knight shift in the normal state of superconducting $(La_{1-x}Ca_x)(Ba_{1.75-x}La_{0.25+x})Cu_3O_y$, Physica C 408-410 (2004) 826–827.

[58] D. Padro, V. Jennings, M. E. Smith, R. Hoppe, P. A. Thomas, R. Dupree, Variations of titanium interactions in solid state NMR–Correlations to local structre, Journal of Physical Chemistry B 106 (51) (2002) 13176–13185.

[59] K. J. D. MacKenzie, M. Schmücker, M. E. Smith, I. J. F. Poplett, T. Kemmitt, Evolution of crystalline aluminates from hybrid gel-derived precursors studied by XRD and multinuclear solid state MAS NMR IV: Calcium dialumunate, $CaAl_4O_7$ and calcium hexaluminate, $CaAl_{12}O_{19}$, Thermochimica Acta 363 (1-2) (2000) 181–188.

[60] A. Trokiner, A. Bessière, R. Thouvenot, D. Hau, J. Marko, V. Nardello, C. Pierlot, J.-M. Aubry, Solid state and solution ^{43}Ca NMR of calcium peroxides involved in the disproportionation of hydrogen peroxide by calcium hydroxide, Solid State Nuclear Magnetic Resonance 25 (4) (2004) 209–215.

[61] A. Wong, D. Laurencin, R. Dupree, M. E. Smith, Two-dimensional ^{43}Ca–^{1}H correlation solid-state NMR spectroscopy, Solid State Nuclear Magnetic Resonance 35 (1) (2009) 32–36.

[62] Z. Lin, M. E. Smith, F. E. Sowrey, R. J. Newport, Probing the local structural environment of calcium by natural-abundance solid-state ^{43}Ca NMR, Physical Review B 69 (22) (2004) 224107–1:7.

[63] D. Laurencin, A. Wong, R. Dupree, M. E. Smith, Natural abundance ^{43}Ca solid-state NMR characterisation of hydroxyapatite: Identification of the two calcium sites, Magnetic Resonance in Chemistry 46 (4) (2008) 347–350.

[64] G. M. Bowers, R. J. Kirkpatrick, Natural abundance ^{43}Ca NMR spectroscopy of tobermorite and jennite: Model compounds for C-S-H, Journal of the American Ceramic Society 92 (2) (2009) 545–548.

[65] A. Wong, A. P. Howes, R. Dupree, M. E. Smith, Natural abundance ^{43}Ca NMR study of calcium-containing organic solids: A model study for Ca-binding biomaterials, Chemical Physics Letters 427 (1-3) (2006) 201–205.

[66] I. Moudrakovski, R. Alizadeh, J. J. Beaudoin, Natural abundance high field ^{43}Ca solid state NMR in cement science, Physical Chemistry Chemical Physics 12 (26) (2010) 6961–6969.

[67] D. L. Bryce, Calcium binding environments probed by ^{43}Ca NMR spectroscopy, Dalton Transactions 39 (37) (2010) 8593–8602.

[68] J. K. Harper, M. Strohmeier, D. M. Grant, Pursuing structure in microcrystalline solids with independent molecules in the unit cell using ^{1}H–^{13}C correlation data, Journal of Magnetic Resonance 189 (1) (2007) 20–31.

[69] M. Baldus, R. J. Iulliucci, B. H. Meier, Probing through-bond connectivities and through-space distances in solids by magic-angle-spinning nuclear magnetic resonance, Journal of the American Chemical Society 119 (5) (1997) 1121–1124.

[70] H. F. W. Taylor, Proposed structure for calcium silicate hydrate gel, Journal of the American Ceramic Society 69 (6) (1986) 464–467.

[71] H. F. W. Taylor, Nanostructure of C-S-H: Current status, Advanced Cement Based Materials 1 (1) (1993) 38–46.

[72] J. Rottstegge, C. C. Han, W. D. Hergeth, Compatibility investigations on polymer-fiber-reinforced cements modified with polymer latexes, Macromolecular Materials and Engineering 291 (4) (2006) 345–356.

[73] I. Sakurada, Some fundamental aspects of polymer reactions, Pure and Applied Chemistry 16 (2-3) (1968) 263–283.

[74] R. Koopmans, R. Dommisse, F. Alderweireldt, R. van der Linden, E. F. Vansant, Reactivity differences between isolated and vicinal vinyl acetate functions in high pressure ethylene/vinyl acetate copolymers, European Polymer Journal 19 (2) (1983) 165–169.

[75] C. Fonseca, J. G. Fatou, J. M. Pereña, Study of the acetoxy-hydroxide transformation in ethylene-vinyl acetate copolymers, Die Angewandte Makromolekulare Chemie 190 (1) (1991) 137–155.

[76] N. B. Winter, Understanding cement: An introduction to cement production, cement hydration and deleterious processes in concrete, Electronic Book (2009).

[77] SABIC Innovative Plastics Ultem 1000 polyetherimide, (Last accessed May 14, 2010), `http://www.matweb.com/search/DataSheet.aspx?MatGUID=e2d985b723954e54aac5327093460528`.

[78] S. S. Song, M. Cakmak, J. L. White, Orientation and mechanical property development in the melt spinning of fibers from polyetherimide and polyarylate, International Polymer Processing 4 (4) (1991) 332–336.

[79] P. Plastics, Ultem 1000 - polyetherimide, Tech. rep., Quadrant Engineering Plastic Products, (Last accessed May 14, 2010) `http://quadrant.matweb.com/SpecificMaterial.asp?bassnum=P1SM50` (2008).

[80] S.-G. Kim, K.-H. Lee, Effects of chemical transition of polyetherimide membranes having an integrally skinned asymmetric structure, Current Applied Physics 9 (2) (2009) e51–e55.

[81] J. Jang, S. Shin, Toughness improvement of tetrafunctional epoxy resin by using hydrolysed poly(ether imide), Polymer 36 (6) (1995) 1199–1207.

[82] ACD/13CNMR Predictor version 4.56, 90 Adelaide Street West Toronto, Ontario M5H 3V9, Canada www.acdlabs.com copyright 1994-2000.

[83] A. J. Lovinger, D. J. Freed, Inhomogeneous thermal degradation of poly(vinylidene fluoride) crystallized from the melt, Macromolecules 13 (4) (1980) 989–994.

[84] Y. Wang, M. Cakmak, J. L. White, Structure development in melt spinning poly(vinylidene fluoride) fibers and tapes, Journal of Applied Polymer Science 30 (6) (1985) 2615–2632.

[85] K. Matsushige, K. Nagata, S. Imada, T. Takemura, The II-I crystal transformation of poly(vinylidene fluoride) under tensile and compressional stresses, Polymer 21 (12) (1980) 1391–1397.

[86] C.-H. Du, B.-K. Zhu, Y.-Y. Xu, Effects of stretching on crystalline phase structure and morphology of hard elastic PVDF fibers, Journal of Applied Polymer Science 104 (4) (2007) 2254–2259.

[87] H. Kise, H. Ogata, M. Nakata, Chemical dehydrofluorination and electrical conductivity of poly(vinylidene fluoride) films, Die Angewandte Makromolekulare Chemie 168 (1) (1989) 205–216.

[88] H. Kise, H. Ogata, Phase transfer catalysis in dehydrofluorination of poly(vinylidene fluoride) by aqueous sodium hydroxide solutions, Journal of Polymer Science: Polymer Chemistry Edition 21 (12) (1983) 3443–3451.

[89] J. W. Cho, H. Y. Song, Dehydrofluorination of a copolymer of vinylidene fluoride and tetrafluoroethylene by phase transfer catalysis reaction, Journal of Polymer Science Part A: Polymer Chemistry 33 (13) (1995) 2109–2112.

[90] J. Scheirs, Compositional and Failure Analysis of Polymers: A Practical Approach, John Wiley & Sons, Ltd., New York, 2000.

[91] R. E. Banks, B. E. Smart, J. C. Tatlow (Eds.), Organofluorine Chemistry: Principles and Commercial Applications, Plenum Press, New York, 1994.

[92] P. Holstein, U. Scheler, R. K. Harris, Triple-channel solid-state NMR investigation of poly(vinylidene fluoride) polymorphs, Magnetic Resonance in Chemistry 35 (9) (1997) 647–649.

[93] P. K. Pallathadka, S. S. Tay, L. Tianxi, P. Sprenger, Solid state ^{19}F NMR study of crystal transformation in PVDF and its nanocomposites, Polymer Engineering and Science 46 (12) (2006) 1684–1690.

[94] E. B. Wilson, J. C. Decius, P. C. Cross, Molecular Vibrations: The Theory of Infrared and Raman Vibrational Spectra, McGraw-Hill Book Company, Inc, 1955.

[95] Y. Bormashenko, R. Pogreb, O. Stanevsky, E. Bormashenko, Vibrational spectrum of PVDF and its interpretation, Polymer Testing 23 (7) (2004) 791–796.

[96] R. Gregorio, Jr., R. C. Capitão, Morphology and phase transition of high melt temperature crystallized PVDF, Journal of Materials Science 35 (2) (2000) 299–306.

[97] A. Salimi, A. A. Yousefi, FTIR studies of β-phase crystal formation in stretched PVDF films, Polymer Testing 22 (6) (2003) 699–704.

[98] T. Boccaccio, A. Bottino, G. Capannelli, P. Piaggio, Characterization of PVDF membranes by vibrational spectrocopy, Journal of Membrane Science 210 (2) (2002) 315–329.

[99] L. N. Pirozhnaya, O. B. Zubkova, L. A. Gribov, Vibration spectra of polymers and copolymers consisting of CH_2 and CF_2 groups, Zhurnal Prikladnoi Spektroskopii 48 (1) (1988) 65–70.

[100] J. C. Li, C. L. Wang, W. L. Zhong, P. L. Zhang, Q. H. Wang, J. F. Webb, Vibrational mode analysis of β-phase poly(vinylidene fluoride), Applied Physics Letters 81 (12) (2002) 2223.

[101] J. C. Li, C. L. Wang, W. L. Zhong, P. L. Zhang, Q. H. Wang, IR vibrational modes of PVDF chains, Synthetic Metals 135-136 (2003) 469–470.

[102] M. A. White, Properties of Materials, Oxford University Press, New York, 1999.

[103] Q. Chen, K. Schmidt-Rohr, ^{19}F and ^{13}C NMR signal assignment and analysis in a perfluorinated ionomer (Nafion) by two-dimensional solid-state NMR, Macromolecules 37 (16) (2004) 5995–6003.

[104] S.-F. Liu, K. Schmidt-Rohr, High-resolution solid-state ^{13}C NMR of fluoropolymers, Macromolecules 34 (24) (2001) 8416–8418.

[105] U. Lappan, U. Geibler, U. Scheler, K. Lunkwitz, Identification of new chemical structures in poly(tetrafluoroethylene-co-perfluoropropyl vinyl ether) irradiatied in vacuum at different temperatures, Radiation Physics and Chemistry 67 (3-4) (2003) 447–451.

[106] C. Gervais, D. Laurencin, A. Wong, F. Pourpoint, J. Labram, B. Woodward, A. P. Howes, K. J. Pike, R. Dupree, F. Mauri, C. Bonhomme, M. E. Smith, New perspectives on calcium environments in inorganic materials containing calcium-oxygen bonds: A combined computational-experimental ^{43}Ca NMR approach, Chemical Physics Letters 464 (1-3) (2008) 42–48.

[107] K. O. Kjellsen, A. Monsøy, K. Isachsen, R. J. Detwiler, Preparation of flat-polished specimens for SEM-backscattered electron imaging and X-ray microanalysis–importance of epoxy impregnation, Cement and Concrete Research 33 (4) (2003) 611–616.

[108] W. Thalheimer, S. Cook, How to calculate effect sizes from published research: A simplified methodology (August 2002) Retrieved August 17, 2010 from http://work–learning.com/effect_sizes.htm.

[109] E. Ramirez-Vargas, D. Navarro-Rodriguez, F. J. Medellin-Rodriguez, B. M. Huerta-Martinez, J. S. Lin, Morphological and mechanical properties of polypropylene [PP]/poly(ethylene vinyl acetate)[EVA] blends. I. Homopolymer PP/EVA systems, Polymer Engineering and Science 40 (10) (2000) 2241–2250.

[110] L. Liu, Y. Wang, F. Xiang, Y. Li, L. Han, Z. Zhou, Effects of functionalized multiwalled carbon nanotubes on the morphologies and mechanical properties of PP/EVA blend, Journal of Polymer Science: Part B: Polymer Physics 47 (15) (2009) 1481–1491.

[111] H. P. Blom, J. W. Teh, A. Rudin, iPP/HDPE blends. II. Modification with EPDM and EVA, Journal of Applied Polymer Science 60 (9) (1996) 1405–1417.

Appendix A

Fibre/White Cement Electron Images

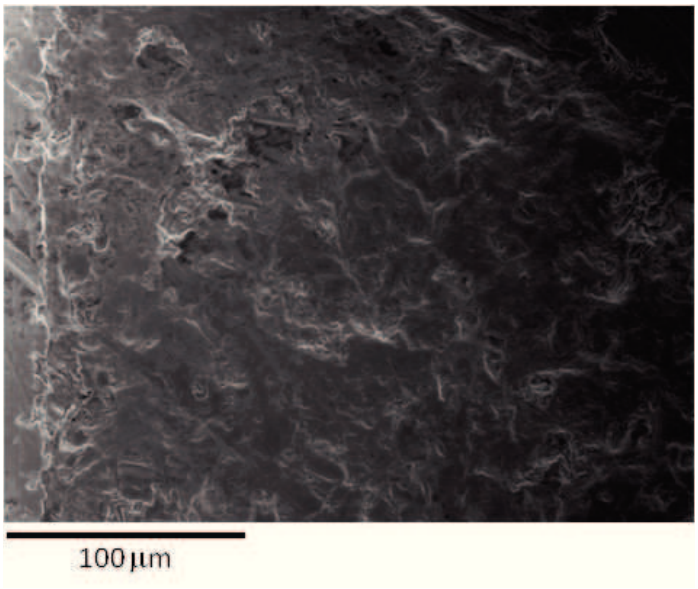

Figure A.1: Secondary electron image of the steel fibre/white cement interfacial transition zone.

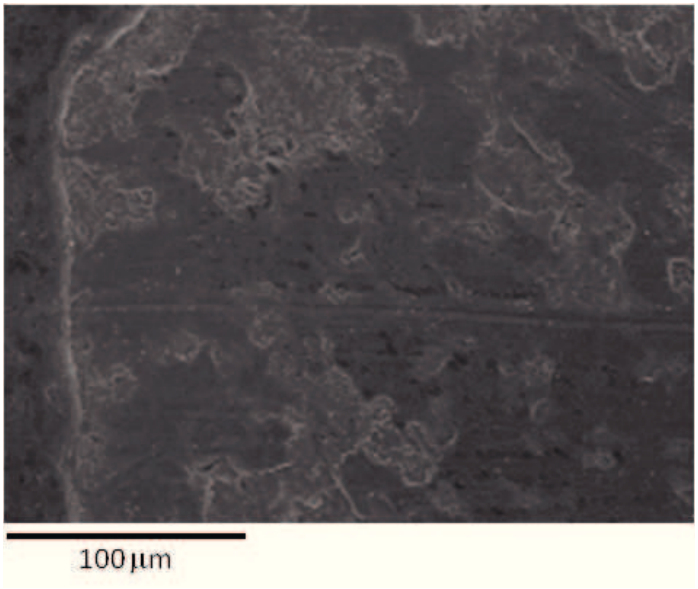

Figure A.2: Secondary electron image of the HDPE/PP fibre/white cement interfacial transition zone.

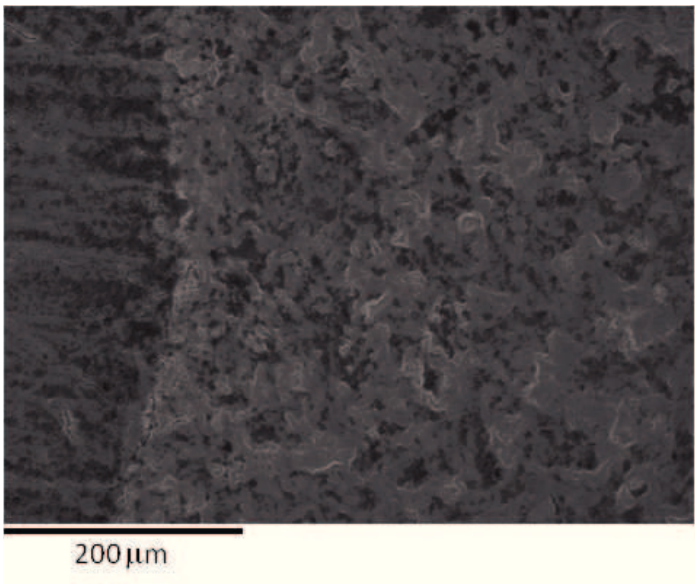

Figure A.3: Secondary electron image of the PVA fibre/white cement interfacial transition zone.

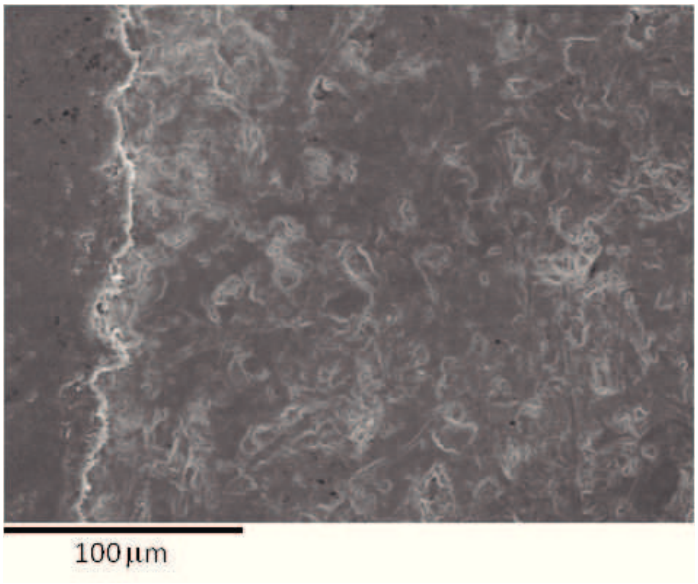

Figure A.4: Secondary electron image of the PVDF fibre/white cement interfacial transition zone.

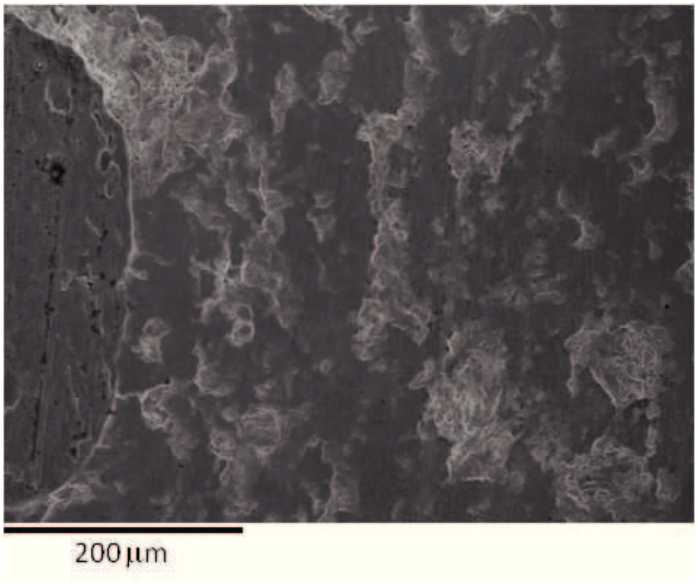

Figure A.5: Secondary electron image of the PEI fibre/white cement interfacial transition zone.

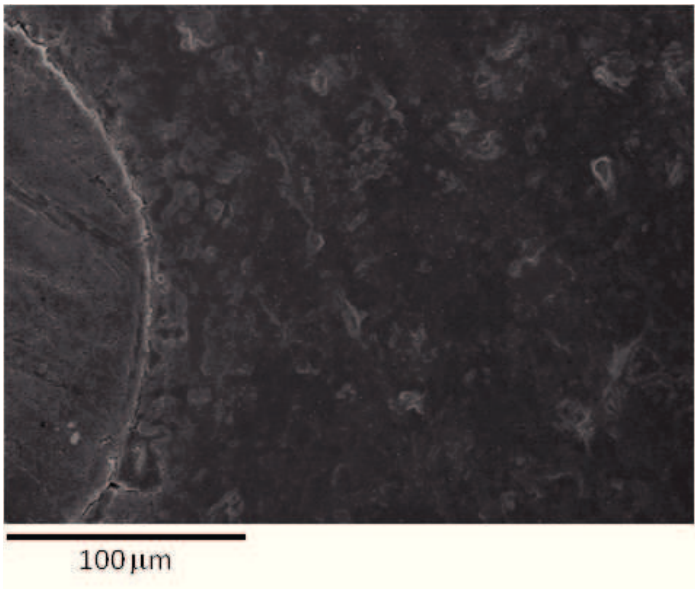

Figure A.6: Secondary electron image of the Nylon 6.6 fibre/white cement interfacial transition zone.